



UNIVERSITÀ DEGLI STUDI DI PALERMO

Progetto: DELIAS – “Ricercatori ed Esperti Di Alta Tecnologia e Innovazione Tecnologica Applicata al Settore dei Beni Culturali” a valere sull’Avviso n. 713/Ric. del 29 ottobre 2010

TITOLO III

“CREAZIONE DI NUOVI DISTRETTI E/O NUOVE AGGREGAZIONI PUBBLICO – PRIVATE”

Codice identificativo progetto: PON03PE 00214 2/F9

Dottorato di ricerca in Information and Communication Technology (ICT)
Scuola Politecnica, Dipartimento di Energia, Ingegneria dell'Informazione e Modelli Matematici.
Settore Scientifico Disciplinare ING-INF/01

Innovative systems based on optical nanoantennas for energy harvesting application

IL DOTTORE

Ing. Chiara Di Garbo

IL COORDINATORE

Chiar.mo Prof. Ing. Ilenia Tinnirello

IL TUTOR

Chiar.mo Prof. Ing. Patrizia Livreri

CO TUTOR

Chiar.mo Prof. Ing. Gianpaolo Vitale

CICLO XXX

ANNO CONSEGUIMENTO TITOLO 2018



*To my daughter Sara, to
my mum Vera and to my
grandma Lilla*

ABSTRACT

The purpose of this study is to outline the main guidelines for the design of arrays of optical rectennas aiming to harvest energy and for the optimization of the power transfer to an external load. In particular, the novelty of this study consists in introducing the concept of the integrated design between the array of optical rectennas and the harvesting circuit able to exploit the available energy.

The design of the array represents the crucial point in order to optimize the power transfer between the antenna and the load and can influence the rectenna design. On the other hand, the maximum power transfer to the load has to be obtained under matching conditions between the array and the load and can influence both the design of the array and of the converter to supply a load.

A previous study of the main type of nanoantennas and their relative structures will be fulfilled in order to choose the particular structure, which will be analysed in this work.

Therefore, a numerical analysis of the chosen structure, a dipole nanoantenna, and a description of the rectenna topology will be performed.

The exploitation of the available energy requires the use of the DC-DC boost converter, which allows to interface a rectenna system with a downstream load.

The choice of the commercially DC-DC boost converter will allow to design an array of optical rectennas in order to achieve the impedance matching conditions to a harvesting circuit.

Finally, since the equivalent impedance of the array of optical rectennas changes with the solar radiation during a day, the optimization of the maximum power transfer between the array and the harvesting circuit will be investigated.

TABLE OF CONTENTS

ABSTRACT	1
TABLE OF CONTENTS.....	2
LIST OF FIGURES	5
LIST OF TABLES	9
ACKNOWLEDGEMENTS.....	10
INTRODUCTION.....	11
CHAPTER I – OPTICAL NANOANTENNAS.....	15
1.1 – HISTORY OF OPTICAL NANOANTENNAS	15
1.2 – METALLIC NANOANTENNAS	16
1.2.2 – <i>Dipole</i>	18
1.2.3 – <i>Bowtie</i>	19
1.2.4 – <i>Spiral</i>	21
1.2.5 – <i>Yagi-Uda</i>	23
1.3 – DIELECTRIC NANOANTENNA	24
1.4 – FABRICATION.....	26
1.4.1 – <i>Electron Beam Lithography (EBL)</i>	27
1.4.2 – <i>Focused Ion Beam Milling (FIB)</i>	28
1.4.3 – <i>Nano-imprint Lithography (NIL)</i>	28
CONCLUSION	29
CHAPTER II – ANALYSIS OF THE MAIN OPTICAL NANOANTENNA PARAMETERS ...	31
2.1 – SIMULATIONS	31
2.1.1 – <i>Modelling techniques</i>	31
2.1.2 – <i>Software tools</i>	32
2.1.3 – <i>Software CST Studio Suite</i>	34
2.1.4 – <i>Simulated structure</i>	34
2.2 – SIMULATION RESULTS	37
2.2.1 – <i>Nanoantenna impedance evaluation</i>	37
2.2.2 – <i>Effective area evaluation</i>	41
2.2.3 – <i>Nanoantenna electrical parameters evaluation</i>	42
CONCLUSION	45

CHAPTER III – RECTENNA TOPOLOGY	48
3.1 – EQUIVALENT CIRCUIT CONFIGURATION	48
3.2 – MAIN RECTIFIERS	49
3.2.1 – <i>MIM diode</i>	50
3.2.2 – <i>MOM diode</i>	52
3.2.3 – <i>Geometric diode</i>	52
3.2.4 – <i>Carbon nanotube forests</i>	53
3.3 – DIODE EQUIVALENT IMPEDANCE	54
3.4 – RECTENNA SYSTEMS APPLICATIONS	56
3.5 – SEEBECK NANOANTENNAS	57
CONCLUSION	59
CHAPTER IV – DC-DC BOOST CONVERTERS FOR ENERGY HARVESTING APPLICATIONS.....	62
4.1 – MAIN ISSUES OF OPTICAL RECTENNA	62
4.2 – HARVESTING CIRCUITS	63
4.2.1 – <i>LTC3108</i>	66
4.2.2 – <i>LTC3105</i>	68
4.2.3 – <i>SPV1050</i>	70
4.3 – CHOICE OF LTC3108	72
4.3.1 – <i>Evaluation board</i>	73
4.3.2 – <i>Mode of operation</i>	74
4.3.3 – <i>Input LTC3108 impedance evaluation</i>	75
CONCLUSION	79
CHAPTER V – DESIGN OF RECTENNA ARRAY.....	81
5.1 – IMPEDANCE MATCHING	81
5.2 – VOLTAGE MATCHING.....	84
5.3 – LOAD POWER AND ENERGY EVALUATION	86
5.4 – POWER EVALUATION UNDER DIODE IMPEDANCE MISMATCHING	88
5.5 – COMPARISON BETWEEN PHOTOVOLTAIC CELLS AND OPTICAL RECTENNA	89
CONCLUSION	90
CHAPTER VI – MAXIMUM POWER TRANSFER OPTIMIZATION	92
6.1 – EXTERNAL CONVERTER CONTROL.....	92
6.1.1 – <i>Open collector</i>	94

6.1.2 – <i>Not three-state port</i>	96
6.2 – CONTROL CIRCUIT	100
6.2.1 – <i>Design of control circuit</i>	101
6.2.2 – <i>Implementation of control circuit</i>	105
6.2.3 – <i>Measures</i>	106
6.3 – POWER EVALUATION UNDER MISMATCHING CONDITIONS	109
CONCLUSION	112
CONCLUSIONS AND FUTURE WORK	114
REFERENCES.....	119
PUBLICATIONS	129
GLOSSARY	131

LIST OF FIGURES

Figure 1: a) Surface plasmon polariton; b) localized surface plasmons; c) field enhancement in the gap between two nano-metal particles [59].....	17
Figure 2: Monopole and dimer metallic nanoantennas [27].	17
Figure 3: Nanodipole model	18
Figure 4: Spectra of intensity enhancement a) for different dipole arm lengths, b) for different gap sizes [60].	18
Figure 5: Spatial distribution of electric field enhancement in the gap of the dipole [61].....	18
Figure 6: Dipole nanoantenna SEM image [27]	19
Figure 7: Bowtie nanoantenna model	19
Figure 8: Bowtie nanoantenna SEM image[27].....	20
Figure 9: Electric field distributions of bowtie nanoantenna at the resonances [65]	20
Figure 10: Spectra response comparison between dipole and bowtie nanoantenna [26].....	20
Figure 11: Electric field enhancement versus wavelength for dipole and bowtie nanoantennas [42].	21
Figure 12: Square spiral nanoantenna model [35]	21
Figure 13: The Electrical field pattern of square spiral nanoantenna [69].....	22
Figure 14: a) SC spiral nanoantenna; b) NSC spiral nanoantenna [69]	22
Figure 15: Yagi-Uda nanoantenna model [71].....	23
Figure 16: Yagi-Uda nanoantenna SEM image [27].....	23
Figure 17: Huygens element [27].....	24
Figure 18: Wavelength dependence of directivity in Huygens element [27].....	25
Figure 19: Dielectric Yagi-Uda nanoantenna [71].....	25
Figure 20: Wavelength dependence of directivity in dielectric Yagi-Uda Nanoantenna [71].....	25
Figure 21: Efficiency curves of dielectric and plasmonic antenna [41, 72].....	26
Figure 22: EBL [26].....	27
Figure 23: FIB [26]	28
Figure 24: Sketch of simulated dipole nanoantenna for L equal to 150 nm	35
Figure 25: Excitation signal	35
Figure 26: Sketch of circularly polarized plan wave.....	36
Figure 27: Discrete port in the gap.....	36
Figure 28: Electric field enhancement at interface dipole-gap	36
Figure 29: Zoom of electric field enhancement at the interface between dipole and gap.....	37

Figure 30: Circuit for calculation of internal nanoantenna impedance	38
Figure 31: a) Open circuit voltage at the end of dipole when load is not connected; b) FFT	39
Figure 32: a) The voltage occurring when the load Z_L is connected to the dipole; b) FFT	40
Figure 33: Radiation efficiency versus wavelength, for dipole arm length in a range from 100 nm to 350 nm [56].....	43
Figure 34: Equivalent circuit for calculation of nanoantenna power	45
Figure 35: Block diagram of Solar Rectenna.....	48
Figure 36: Equivalent circuit of Solar Rectenna	49
Figure 37: Energy band profile of a single insulator MIM diode [96].....	51
Figure 38: Inverse arrowhead geometric diode structure [101]	53
Figure 39: Schematic of carbon nanotube rectenna [58, 103].....	53
Figure 40: Illuminated I(V) curve. V_{ph} is the photon energy $\hbar\omega/q$ [111].....	54
Figure 41: Sketch of a current-voltage I(V) curve for a rectenna diode [33].....	55
Figure 42: Electric equivalent circuit of the antenna-coupled thermocouples [90]	58
Figure 43: Step-up DC-DC converter [128].....	63
Figure 44: Charge pump step-up converter [129]	64
Figure 45: Self-oscillating step-up DC-DC converter [130].....	65
Figure 46: Equivalent Circuit of a typical application LTC3108 [132].....	66
Figure 47: Input resistance versus V_{IN} [132].....	67
Figure 48: a) Start-up voltage sequencing in LTC3108; b) PGD response versus V_{OUT} during a step load in LTC3108 [132].....	68
Figure 49: Equivalent Circuit of a typical application LTC3105 [133].....	68
Figure 50: Typical LTC3108 start-up sequence [133].....	69
Figure 51: SPV1050 block diagram [134]	70
Figure 52: SPV1050 Boost configuration [134]	71
Figure 53: SPV1050 start-up behavior [134].....	71
Figure 54: SPV1050 MPPT tracking [134].....	72
Figure 55: LTC3108 Demonstration Circuit 1582B [135].....	73
Figure 56: LTC3108 block diagram [132]	74
Figure 57: Output voltage sequencing [132].....	75
Figure 58: The experimental rig.....	76
Figure 59: Connections in the rig.....	76
Figure 60: Time domain waveforms of input current I_{IN} (top), P_{GD} voltage (middle) and output voltage V_{STORE} (bottom)	77
Figure 61: Load power versus R_A and R_L	82

Figure 62: Equivalent circuit of an array of N*M optical rectennas.....	83
Figure 63: Equivalent circuit for calculation of rectenna array power.....	86
Figure 64: Solar radiation versus time	87
Figure 65: Load power versus diode resistance	88
Figure 66: a) Detail of the LTC3108 board; b) Detail of the LTC3108 block diagram [132, 135] ..	92
Figure 67: Equivalent circuit of the simulated self-oscillating stage of LTC3108	93
Figure 68: Trend of the reducing of the self-oscillating stage pulse train for different time intervals	93
.....	
Figure 69: Gate voltage of the MOSFET as a function of the external control	94
Figure 70: SN74LS06 functional block diagram [136].....	95
Figure 71: Experimental rig	95
Figure 72: a) SN74LS244 3-state octal buffer; b) SN74LS244 functional logic diagram [137]	96
Figure 73: a) SN74LS244 typical input; b) SN74LS244 typical output [137]	97
Figure 74: Experimental rig	97
Figure 75: Converter control at D = 95%.....	98
Figure 76: Converter control at D = 50%.....	99
Figure 77: Converter control at D = 35%.....	99
Figure 78: Input impedance R_{IN} versus square-wave duty cycle D	100
Figure 79: a) SN74LS32; b) Logic diagram [138].....	101
Figure 80: Schematic of the SN74LS32 [138].....	101
Figure 81: Logic diagram of the three-state port driven by the OR port.....	102
Figure 82: a) SN74LS00; b) Logic Diagram of each gate [139].....	103
Figure 83: Logic diagram of the circuit with the OR port, the NAND port and the three-state port	104
.....	
Figure 84: Block diagram of the prototype of the external control circuit [140].....	105
Figure 85: Equivalent circuit of the prototype of the external control circuit [140].....	105
Figure 86: Experimental rig	106
Figure 87: The trends of the gate voltage (yellow) and the square-wave duty cycle (purple) [140]	107
.....	
Figure 88: The DC-DC converter input impedance R_{IN} versus the square-wave duty cycle D [140]	108
.....	
Figure 89: A block diagram of a typical energy harvesting system based on nanoantennas	109
Figure 90: Input impedance R_{IN} versus input voltage V_{IN}	110
Figure 91: Input power P_{IN} versus input impedance R_{IN}	111
Figure 92: Normalized input power versus the ratio R_M/R_{IN}	111

Figure 93: Example of integrated design118

LIST OF TABLES

Table 1: Internal nanodipole impedance values at 250 THz, 350 THz and 1000 THz	41
Table 2: Effective nanodipole area values at 250 THz, 350 THz and 1000 THz	42
Table 3: Poynting vector and optimal power	44
Table 4: Electrical field, V_{open} and output voltage V_O	45
Table 5: Regulated voltage using pins V_{S1} and V_{S2} [132].....	67
Table 6: Comparison between LTC3108, LTC3105 and SPV1050.....	72
Table 7: Electrical characteristics of the Demonstration Circuit 1582B [135].....	74
Table 8: R_{IN} values at $C_{OUT} = 220 \mu F$ and $R_{OUT} = 100 k\Omega$	77
Table 9: R_{IN} values at $C_{TOT} = 1220 \mu F$ and $R_{OUT} = 100 k\Omega$	78
Table 10: Parameters of an array of optical rectennas	85
Table 11: Effective area and geometric area of an array of optical rectennas	85
Table 12: Comparison between traditional PV cells and rectennas	89
Table 13: SN74LS244 function table.....	97
Table 14: Input current I_{IN} and input impedance R_{IN} values	100
Table 15: SN74LS32 function table [138]	102
Table 16: Function table of logic diagram in Figure 81.....	102
Table 17: SN74LS00 function table [139].....	104
Table 18: Function table of logic diagram in Figure 83.....	104
Table 19: Input current I_{IN} , input voltage V_{IN} and input impedance R_{IN} values	108
Table 20: Input voltage V_{IN} , input current I_{IN} , input impedance R_{IN} and input power P_{IN}	110

ACKNOWLEDGEMENTS

I would like to express my deepest gratitude to my advisor Prof. Patrizia Livreri because, despite how busy she is, she always found the time to help and support me during these years. My deepest gratitude also goes to my second advisor Prof. Gianpaolo Vitale from whom I learned a lot and who always provided me with support and encouragement along the way.

My sincere thanks go to all colleagues and researchers I met during these three years.

I am eternally grateful to my parents, Enzo and Vera. Without their encouragement, support and help, I could not have achieved my goals.

Thank you also to my sister Agnese and my brother in law Rosario, and to my sister Francesca for her “English” support, my brother in law Raphaël and my little nephew, who will be born in February.

I am grateful to my late grandmother Lilla for her strength, energy and for all that I learned from her.

Finally, my biggest thanks to Cristiano for his love, patience, support and understanding and to my daughter Sara, whose love is the reason of my life.

INTRODUCTION

Nowadays, a growing demand for renewable energy requires the study and the development of new technologies that are able to harvest ambient energy. Recently, several low power sources using different mechanisms to harvest mechanical, thermal, solar, and chemical energy have been considered in the literature. Among these, fuel cells as electrochemical systems able to convert chemical energy in electricity have been discussed [1-3]. Piezoelectric systems exploit mechanical energy [4-7]. Thermoelectric generators convert heat in electricity [8-10]. However, the Sun seems to be the most important source of renewable energy. As a matter of fact, during the last two decades several approaches and technologies to harvest energy from the Sun has been proposed and implemented. Among these, solar photovoltaic (PV) cells able to convert directly sunlight into electricity have been discussed [11-20]. Traditional solar photovoltaic (PV) sources are typically p-n junction cells made of semiconductor materials that can absorb photons whose energy is greater than the bandgap. Solar radiation is composed of energy photons whose energy is generally higher than the bandgap of the solar cells. Therefore, only photons charged with an energy equal to the bandgap can be efficiently harvested, while the excess of energy is converted into heat by lattice vibrations or phonons. For this reason, the upper efficiency is about 20% [21-22]. In order to overcome this limitation, multi-junction PV cells have been studied and developed [16, 18-19]. Even if the Sun seems to be one of the most promising source for harvesting purposes, there are some intrinsic limitations: PV cells are strongly dependent on daylight, which makes them also sensitive to the weather conditions [23]. The thermal radiation from the fusion reaction in the Sun is transferred in the form of electromagnetic waves into the free space. About 30% of solar radiation is scattered and reflected back to the space from the atmosphere, and 70% is absorbed by the atmosphere and by the surface of the Earth [24-25]. As a consequence, the Earth temperature rises and electromagnetic waves in the wavelength range from 8 μm to 14 μm are reemitted. This type of radiation, named Long-Wave Infrared Radiation (LWIR), is an electromagnetic wave radiation at terahertz frequencies that cannot be collected by traditional PV sources. Therefore, new technologies overcoming the drawbacks of the traditional PV conversion and harvesting the reemitted LWIR energy are being developed [24]. These new devices, called nanoantennas, have only recently been considered thanks to the development of electron beam lithography and similar techniques, which are able to assure the required level of miniaturization for the purposes of realization and demonstration. Nanoantennas operate at nanometers wavelengths and have dimensions in a range that goes from a few hundred nanometres to a few microns. They exhibit potential advantages in terms of polarization, tunability, and rapid time response. Furthermore, the nanoscale dimensions, combined with the high electric field enhancement in the antenna gap, enable a small device footprint, which is compact enough to be

monolithically integrated with electronics and auxiliary optics [26-27]. Similar to traditional RF antennas, nanoantennas capture the incident visible or infrared electromagnetic wave causing an AC current onto the antenna surface, such that it oscillates at the same frequency of that of the wave. As a result, contrarily to the traditional PV cells no energy threshold is present. The movement of the electrons produces an alternating current or voltage in the antenna circuit that can be rectified in order to produce a DC power and to supply an external load. For this reason, a proper rectifier coupled with nanoantenna is used. It can be noted that this is a difference in comparison to PV cells that provide a DC current; whereas in both systems there is need to match the source with the load to achieve the maximum available power [26, 28-32]. The rectifier usually coupled with a nanoantenna is an ultra-high speed rectifier and contains one or more diodes whose power loss and fast response can influence the whole device efficiency [33-35]. The combination of a rectifying device at the feed points of a nanoantenna is known as rectenna. The first use of a rectenna for microwave applications dates back to 1960s [36-37]. The idea of harvesting solar energy using nano-rectennas was first proposed by Bailey in 1972 and the first patent on solar rectennas issued to Marks in 1984 [38-39].

Photovoltaic sources and rectennas belong to the so called “frequency dependent energy conversion devices”; a general optimization method, based on the exergy concept has been proposed by [40] where it is developed in detail for PV sources. The article [40] also underlines the need to further study rectennas in order to identify the thermodynamic losses and to rectify the high frequency solar radiation. On the other hand, rectennas can benefit from the broadening of frequency responsive range.

The conversion efficiency of a rectenna depends on the power loss in the diodes, on the impedance matching between the nanoantenna, the rectifier and the load, and on the nanoantenna efficiency [24-25, 41]. Therefore, one of the main issues that can be find when the nanoantennas are employed in energy harvesting systems is the radiation efficiency. In the literature, a great variety of nanoantenna structures depending on the geometry of nanoparticles can be found [27, 42]. The radiation efficiency depends on the metal used as conductor and on the dimension of the nanoantenna. The metals mainly used are gold, silver, aluminium and copper, whose plasmonic properties lie in the optical range. Therefore, an accurate choice of materials and design of nanoantenna is most important for its efficiency [43]. Relatively to the rectifier, the main problems regard diode resistance, capacitance and reverse-bias leakage. The diode resistance has to be sufficiently low in order to achieve a significant reduction of power loss; the diode capacitance has to be small in order to have a fast diode. The significant current for negative voltages in the diode is required to be lower, approximately 1 μA or less [33]. The values of the rectenna output voltage and available power on the load matching conditions are on the order of few tens microvolt and few picowatt, respectively. As a matter of fact, another issue is the impedance matching between the optical rectenna and the load. The latter is typically a DC-DC boost power converter that can be modelled by an equivalent input impedance. Considering the values of the internal

nanoantenna impedance, the diode impedance and the harvesting circuit impedance, the optimal matching can be achieved by a nano-rectenna array whose equivalent impedance equals the harvesting circuit impedance [43]. In the literature, few contributions dealing with rectennas for energy harvesting have been proposed; they are mainly focused on rectennas. [24] describes the main issues related to infrared emission exploitation; [33] and [35] deal with solar cells based on the rectennas whereas [44] is devoted to the use of nanoantennas subjected to electromagnetic radiation. As for the Author's knowledge, no contribution has been published about matching conditions between rectennas and loads.

To this purpose, this study is not an exhaustive work on the nanoantennas for energy harvesting or on the main DC-DC boost converters for energy harvesting applications. Instead, the novelty of this study consists in introducing the concept of integrated design between an array of optical rectennas and a harvesting circuit able to exploit the available energy. Especially, the goal of this study is to define a methodology with which to realize the integration of these two systems. For this purpose, the main guidelines for the design of an array of optical rectennas aiming to harvest energy and for the optimization of maximum power transfer to the external load are studied and discussed in this work. As it will be explained in the following, the design of the array represents a crucial point in order to optimize the power transfer between the antenna and the load and can influence the rectenna design. On the other hand, the maximum power transfer to the load has to be obtained under matching conditions between the array and the load and can influence both the design of the array and of the DC-DC boost converter.

In the chapter I, a description of the optical nanoantennas will be made. In particular, the main structures of nanoantennas and their mode of operation will be explained.

In the chapter II, an analysis of the main nanoantenna parameters will be illustrated. Especially, the method for the evaluation of the internal nanoantenna impedance, of the nanoantenna effective area and of the electrical parameters will be validated.

In the chapter III, a rectenna topology will be analysed. The equivalent circuit configuration of a rectenna and the main types of the rectifiers will be described. The diode equivalent impedance will be evaluated.

The characteristics of the main commercially DC-DC boost converter for energy harvesting and ultralow power applications will be described in chapter IV. The choice of the DC-DC boost converter based on LTC3108 integrated circuit will be validated.

In chapter V, the main guidelines for the design of an array of optical rectennas will be defined. The optimal impedance matching between the array and the load will be investigated in order to allow the maximum power transfer. The available power and energy during a typical day of July in Palermo (south of Italy, 38.1157° N, 13.3613° E) at the terminal of the array of optical rectennas under matching conditions will be evaluated. The differences between photovoltaic cells and rectenna will be highlighted.

The optimization of the maximum power transfer between the array and the harvesting circuit will be investigated in chapter VI. The design and implementation of an external control circuit in order to dynamically obtain the impedance matching between the array and the harvester will be defined.

CHAPTER I – OPTICAL NANOANTENNAS

An optical nanoantenna is an antenna suitable to be operated at nanometers wavelengths; it has dimensions in a range that goes from a few hundred nanometers to a few microns. This device is able to both efficiently receive and convert an optical frequency radiation into a strongly confined electromagnetic field, and to transmit and convert the strongly confined electromagnetic field in the optical frequency range created by a source into optical radiation [27]. In receiving mode, a nanoantenna captures the incident visible and infrared electromagnetic waves causing an AC voltage or current onto the antenna surface whose frequency is the same of that of the incident radiation. An optical nanoantenna exhibits potential advantages in terms of polarization, tunability, and rapid time response. Furthermore this device is able to harvest both visible and short-wave and long-wave infrared (LWIR) radiation [24-25]. Two main types of optical nanoantennas (metallic and dielectric) can be identified based on their functional properties [27].

1.1 – History of optical nanoantennas

In 1972, Robert Bailey and James C. Fletcher proposed the concept of optical nanoantenna able to convert the incident light into electric power. They received a patent for the device named “Electromagnetic Wave Energy Converter (EWEC)” [38]. This device is a particular detector consisting of a 100 nm-diameter thin metal onto a metal surface covered with a thin oxide layer, used by Ali Javan in 1971 as a rectifier for the infrared radiation at a frequency of 58 THz [45]. In 1974, T. Gustafson and coauthors demonstrated that these types of devices could rectify even visible light to DC current [46]. In 1984, Alvin M. Marks received a new patent for a device using a sub-micron antenna for the direct conversion of light power to electrical power. This device showed substantial improvements in efficiency over Bailey’s device [39]. In 1996, Guang H. Lin and coauthors reported resonant light absorption by a fabricated nanostructure and rectification of light with frequencies in the visible range. It is the first empirical design for the optical nanoantenna in the visible light. The design consists of a dipole antenna array and a p-type boron single crystal wafer with 3 nm oxide layer for the rectification [47]. In 2001, Kottman and coauthors introduced and simulated the idea of using irregular nanoparticles to maximize the incident field enhancement compared to the field enhancement due to a regular one [48]. In 2002, the ITN Energy Systems Inc. published a work on optical antennas coupled with high frequency diode, whose efficiency however was very low [49]. Sundaranurthy and coauthors fabricated two opposing gold 60° bowties with 16 nm tip-to-tip gap operating at optical regime in 2005. The novelty of this study was the possibility to visualize the current distribution along the antenna surface and the current behaviour at the gap [50]. In 2009, McMahon and coauthors proposed a nanoantenna

design of two gold dimers with a diameter of 90 nm and studied the gap effect between the gold dimers on the electric field intensity enhancement [51]. A year later, McMahon published a new study on the designs of cylindrical nano-wires and bowtie antennas using nonlocal dielectric constants [52]. In the same year, Kotter and coauthors designed and fabricated a spiral nanoantenna for solar energy harvesting at mid-infrared region [53]. In 2011, Midrio and coauthors designed and analysed monopole antenna based on nickel for the reception of thermal radiation [54]. In 2012, Chen fabricated a 60° bowtie nanoantenna operating in the IR regime [55]. In the same year, Vandenbosch and coauthors introduced upper bounds for the solar energy harvesting efficiency of nanoantennas. This efficiency was investigated in terms of the dimensions of the nanoantenna and the metal used as a conductor [56]. In 2014, Gadalla and coauthors proposed a THz bowtie antenna integrated with maximum near field intensity enhancement at the infrared energy regime [57]. The state of art of nanoantennas has been achieved only recently in 2015 by Sharma and coauthors that engineered metal–insulator–metal tunnel diodes, with a junction capacitance of about 2 aF, at the tip of vertically aligned multiwalled carbon nanotubes of about 10 nm in diameter, which act as the antenna [58].

1.2 – Metallic Nanoantennas

A metallic nanoantenna consists of one or more metallic nanoparticles working in a range of frequencies close to plasmonic resonance of the used metal. At visible and infrared frequency, metals no longer behave as perfect conductors and become less resistant to electromagnetic waves penetration. Their optical response is described by a complex frequency-dependent dielectric constant and is dominated by the collective behaviour of the free electron gas. The interaction with the electromagnetic (EM) radiation depends on free conduction electrons in metals. These electrons oscillate with respect to fixed positively charged ions in the metal at a frequency that depends both on materials and on incident electric field, creating therefore a quasi-particles located on the metal surface namely plasmons. At the interface between metal and dielectric, surface plasmons can be couple with photons and result in a coherent electron charge oscillations called surface plasmon polariton (SPP). Localized surface plasmons (LSP) exist when light interacts with particles much smaller than the incident wavelength. For incident radiation wavelengths in a range from visible (400-700 nm) to infrared (700-1000 nm), some materials, such as gold, silver, aluminium and copper, are characterized by a negative real part of the dielectric constant and, as a consequence, by a high reflectivity of metal surfaces [26-27, 31, 59]. At this range of wavelengths, the free conduction electrons in these metals are able to generate resonant collective oscillations namely localized plasmonic resonances, originating from the characteristic dielectric response of metals themselves at optical frequencies. These localized plasmonic resonances produce an enhancement of the electrical field at the surface, in particular at the interface between metal and dielectric (gap). Therefore, such enhancement depends on the metal used, on the geometry of

nanoparticles, on the gap width and on the properties of the environment [27]. When metallic nanoantennas absorb the incident electromagnetic radiation at the resonant frequency, a cyclic plasma movement of free electrons is induced and an alternating current at the same frequency as the resonance is generated, which then flows toward the antenna feed point creating a hot spot at which a field intensity is enhanced. Thus, the electric field is concentrated at the center of this point [24, 31, 59].

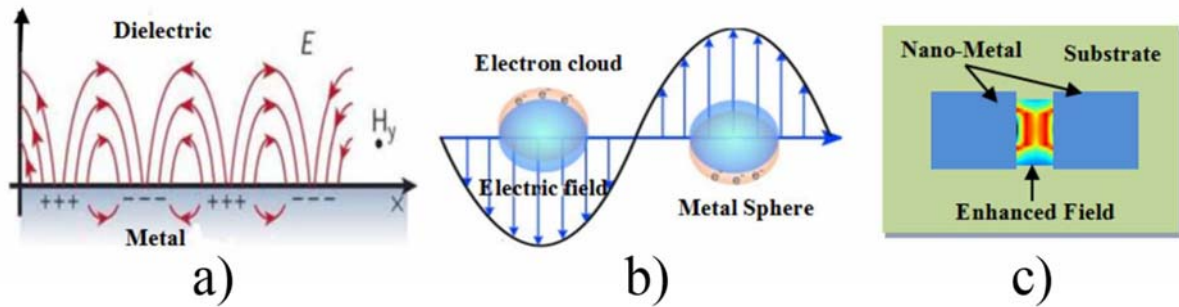


Figure 1: a) Surface plasmon polariton; b) localized surface plasmons; c) field enhancement in the gap between two nano-metal particles [59]

Metallic nanoantennas exhibit large ohmic losses in close proximity to the surface that should be as low as possible. They can be kept low either by choosing a metal with large negative real part of the dielectric constant or by selecting low imaginary part. The metals mainly used are gold, silver, aluminum and copper, whose plasmonic properties lie in the optical range.

A great variety of metallic nanoantennas depending on the geometry of nanoparticles can be found in literature. The simplex type of metallic nanoantenna is the monopole nanoantenna. It consists of a single metallic nanoparticle that increases the strength of the electromagnetic field in its vicinity. The characteristics of monopole nanoantenna depend on the shape, size, material and dielectric environment of the nanoparticle. The dimer nanoantennas confine the high field in the gap between two nanoparticles and include dipole and bowtie nanoantennas that are described in the following sections [41]. Figure 2 shows a monopole and a dimer antennas.

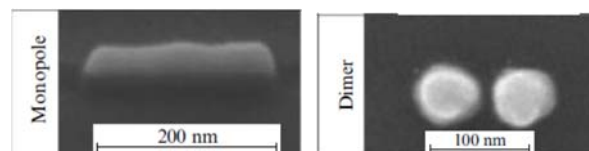


Figure 2: Monopole and dimer metallic nanoantennas [27].

1.2.2 – Dipole

The dipole nanoantennas consist of two coupled nanorods or nanospheres with a gap G in between, as shown in Figure 3.

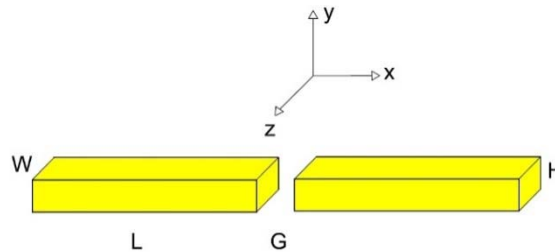


Figure 3: Nanodipole model

The length of each arm (in x direction) is L and the width (in z direction) is W . The height (in y direction) is H . The electric field enhancement is concentrated in the gap G . The spectra response of dipole depends on the arm length L and on the size of the gap, as it can be noted in Figures 4a) and 4b).

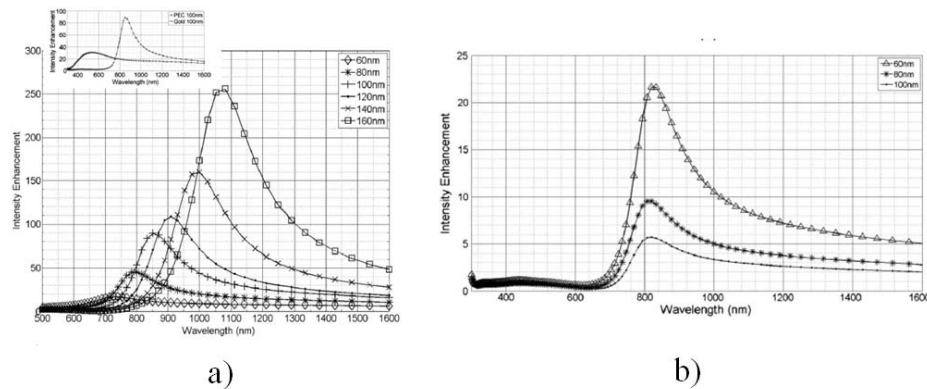


Figure 4: Spectra of intensity enhancement a) for different dipole arm lengths, b) for different gap sizes [60].

The distribution of the electric field enhancement in the gap is shown in Figure 5.

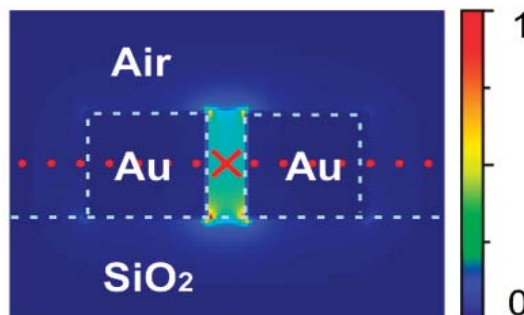


Figure 5: Spatial distribution of electric field enhancement in the gap of the dipole [61]

It can be noted that the distribution of electric field is mainly concentrated in the gap, at the interface between metal and dielectric. This confirms that a dipole nanoantenna is able to generate strong localized field when an electromagnetic wave irradiates its surface [62]. The image of dipole nanoantenna, obtained by scanning electron microscopy (SEM), is shown in Figure 6.

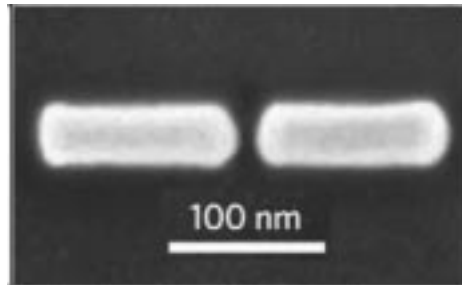


Figure 6: Dipole nanoantenna SEM image [27]

The dipole nanoantennas offer several advantages in terms of easy production, fine-tuning of the operation mode and high confinement of electric field in the gap. They usually are employed in wireless and nanophotonic communication systems with the aid of optical fibres. Furthermore, in order to obtain a higher output power, it is possible to realize an array of dipole nanoantennas [27].

1.2.3 – Bowtie

A bowtie nanoantenna consists of two triangles facing each other from their apices and with a gap in between. The electric field is typically concentrated at its gap [27, 35, 63-64].

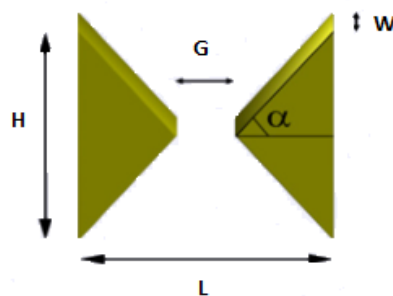


Figure 7: Bowtie nanoantenna model

Bowtie nanoantenna can be applied to enhance molecular fluorescence, Raman scattering and for high-harmonic generation. It is characterized by a broad bandwidth and by a higher field enhancement in the gap compared with dipole nanoantenna because of larger lightning-rod effect at apex [26]. Figure 8 shows an image of bowtie nanoantenna obtained by SEM.

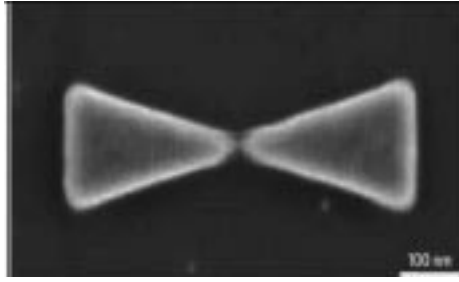


Figure 8: Bowtie nanoantenna SEM image[27]

Figure 9 shows the distribution of the electric field enhancement in the gap.

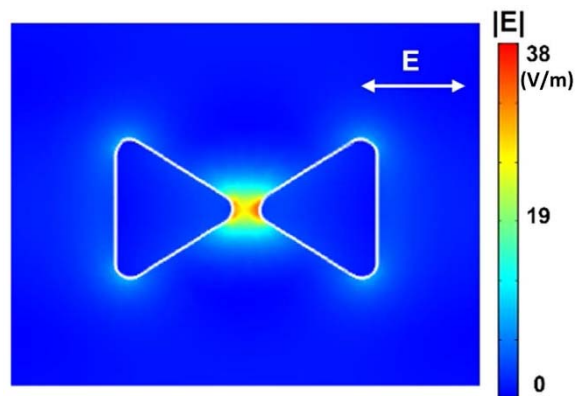


Figure 9: Electric field distributions of bowtie nanoantenna at the resonances [65]

Even though the bowtie nanoantennas have a broad bandwidth, they exhibit a lower confinement factor due to a larger amount of metal used for its fabrication, as shown in Figure 10.

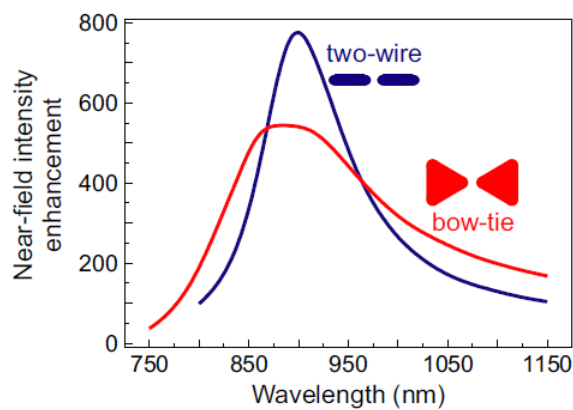


Figure 10: Spectra response comparison between dipole and bowtie nanoantenna [26]

As a consequence, they have greater dissipative losses than a dipole nanoantenna. This is also recently confirmed by Chekini and coauthors, who investigated five different nanoantenna structures, i.e. dipole, bowtie, rounded bowtie, rounded cross bowtie and cross bowtie nanoantennas [42].

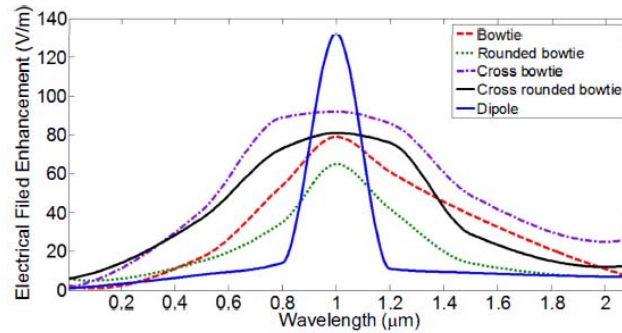


Figure 11: Electric field enhancement versus wavelength for dipole and bowtie nanoantennas [42].

As it can be noted in Figure 11, dipole nanoantennas exhibits the maximum field enhancement in the antenna gap but has the minimum bandwidth. On the other hand, bowtie nanoantennas suffer from low electrical field enhancement and have a larger bandwidth [42]. Moreover, with this type of nanoantenna it is possible to construct an array by coupling several bowtie elements in one configuration and by combining the electric field from each element at the array feeding point, where a rectifier can be embedded [27, 35, 63-64].

1.2.4 – Spiral

Spiral nanoantennas reveal planar structure, circular polarization and broadband characteristics. They are good resonators and they can produce a large field at the feed point with peak values of 8.9 N/C in the wavelength range between 700 nm and 1100 nm. The electric field is enhanced in the gap between the two metallic arms, as shown in Figure 13 [66-70].



Figure 12: Square spiral nanoantenna model [35]

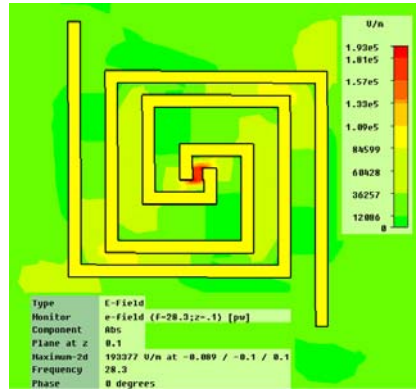


Figure 13: The Electrical field pattern of square spiral nanoantenna [69]

It is possible to enhance the performance of this nanoantenna by increasing the number of arms and, consequently, obtaining an increased aperture area [35]. A square Spiral nanoantennas is modelled by square spiral or logarithmic spiral. Moreover, two configurations of square spiral nanoantenna can be designed: self-complementary (SC) antenna when the distance between the arms is identical and non self-complementary (NSC) antenna otherwise. These spiral nanoantennas work in the infrared band and captures the incident wavelength when the total length of the spiral equals one wavelength. Furthermore, the inductive and capacitive effects can be exist on the antenna structure, due to the folded arms, that affect the resonant frequency and contribute to give a broadband antenna [69]. Figure 14 shows the SC and NSC spiral nanoantennas.

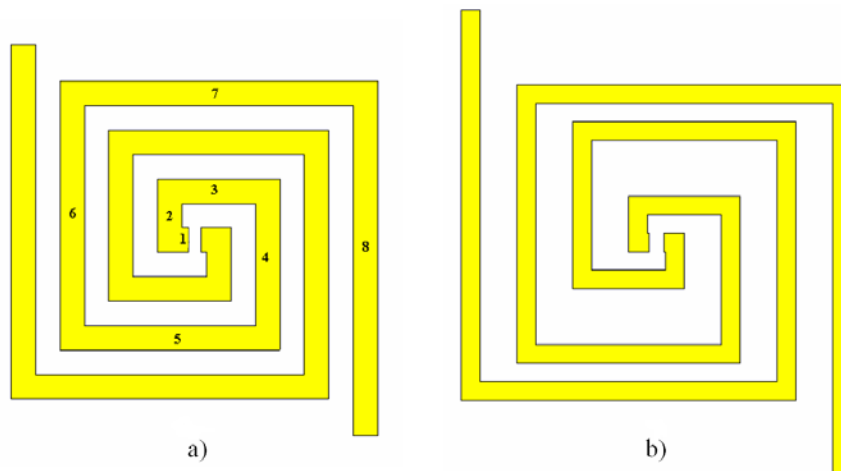


Figure 14: a) SC spiral nanoantenna; b) NSC spiral nanoantenna [69]

The electric field in the NSC nanoantenna is higher than the electric field in the SC nanoantenna. The structure requires a more complicated manufacturing process and a bigger quantity of metal for both the antenna and the ground plane. Therefore, the power losses in these structures are much higher [69].

1.2.5 – Yagi-Uda

Yagi-Uda nanoantennas are narrowband devices that work at frequencies close to those of the plasmon resonances, determined by the dimensions of the antenna elements [27, 71]. They are directive antennas and have a high efficiency in terms of directivity and losses that occur throughout the antenna while it is operating at a given frequency. Furthermore, they are very simple to build [71]. These devices consist of an actively driven element called feed surrounded by passive elements, which are not driven. These passive elements are usually of two types: a resonant reflector and one or several spaced directors, as sketched in Figure 15.

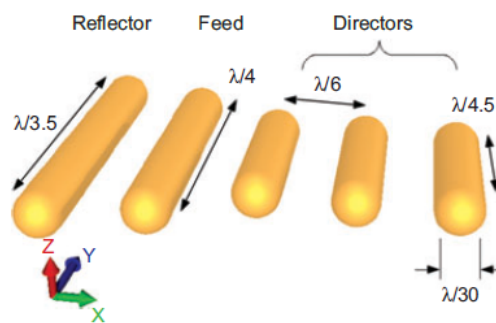


Figure 15: Yagi-Uda nanoantenna model [71]

The length of feeding element is the key parameter and should be at resonance at the desired frequency. The lengths of the reflector and directors are chosen to be off resonance and in phase in the forward direction. Therefore, the director elements are made shorter and the reflector is made longer than the feeding element. Yagi-Uda nanoantennas suffer from the absorption losses in metals in the visible and infrared range. Figure 16 shows an image of Yagi-Uda nanoantenna obtained by scanning electron microscopy.



Figure 16: Yagi-Uda nanoantenna SEM image [27]

1.3 – Dielectric Nanoantenna

Metallic nanoantennas exhibit a small size and a strong localization of the electric field. However, they have large dissipative losses due to utilized metal that reduce their range of working frequencies and result in low radiation efficiency [72]. To overcome these disadvantages a new type of nanoantennas based on dielectric nanoparticles with a high index dielectric constant has been realized. Dielectric nanoantennas are fabricated from optically transparent materials and exhibit smaller dissipative losses in the material with enhanced magnetic response in the visible. They support simultaneously both electric and magnetic resonances which can be controlled independently [72]. They show a resonant response due to the formation of an effective resonator inside the particle. Furthermore, they allow us to achieve the superdirectivity effect. The dielectric nanoantennas include also the antennas based on semiconducting particles, because this type of materials are sufficiently transparent in the visible frequency range. Typically, dielectric nanoantennas consist of spherical particles and sometimes of rods and disks [27]. Several configurations of dielectric nanoantennas have been proposed in the literature.

Whispering gallery antennas consist of dielectric microspheres and possess good directional capabilities by virtue of their large surface area. However, they have a weak influence on the spontaneous relaxation rate of the emitter.

Huygens optical element, consisting of a single dielectric nanoparticle, as shown in Figure 17, can be considered for the creation of totally dielectric nanoantennas with good directional properties.

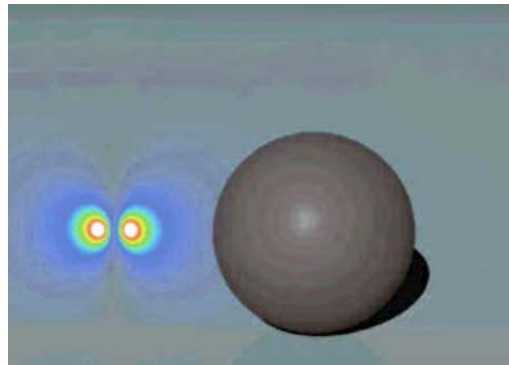


Figure 17. Huygens element [27]

The excitation of such a dielectric particle induces electric and magnetic dipole moments. Depending on the frequencies and on the material and the size of the nanoparticles, the amplitudes of electric and magnetic polarizabilities can be equal to each other. In this way, it is possible to create compact fully dielectric nanoantennas with good directional properties.

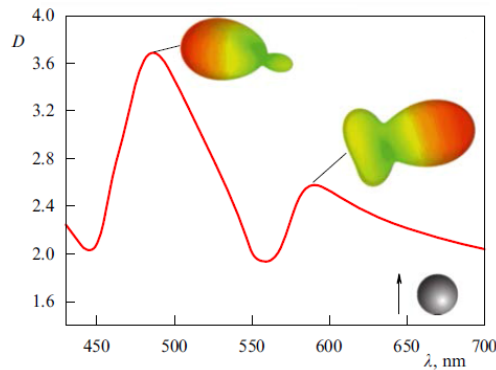


Figure 18: Wavelength dependence of directivity in Huygens element [27]

Dielectric Yagi-Uda nanoantenna consists of more dielectric nanoparticles of equal size. It exhibits the radiation efficiency that slowly decreases with decreasing distance between the elements [27]. This distance influences the operational regime of a dielectric Yagi-Uda nanoantenna. In order to have the best directivity, this type of nanoantenna has to operate in a magnetic regime [27]. An example of dielectric Yagi-Uda nanoantenna, consisting of four directors and one reflector, is shown in Figure 19.

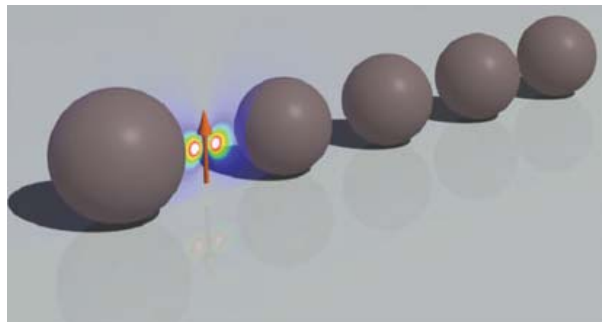


Figure 19: Dielectric Yagi-Uda nanoantenna [71]

Figure 20 illustrates the wavelength dependence of directivity of dielectric Yagi-Uda nanoantennas for different values of gap G [27, 71-72]. The dipole excitation source is placed equidistantly between the reflector and the first director.

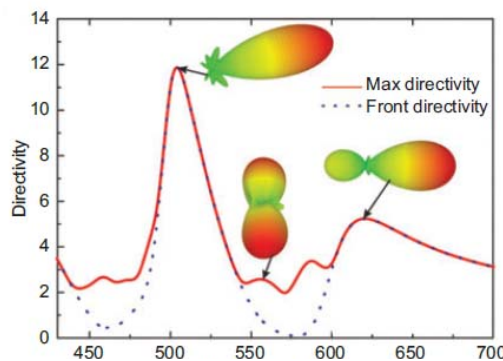


Figure 20: Wavelength dependence of directivity in dielectric Yagi-Uda Nanoantenna [71]

The radiation efficiency of dielectric Yagi-Uda nanoantennas slowly decreases with the distance between the elements. Furthermore, the operational regime strongly depends on the distance between the elements [27]. Figure 21 shows the radiation efficiency of dielectric and plasmonic Yagi-Uda nanoantennas. It can be noted that the efficiency curves are similar [41, 72].

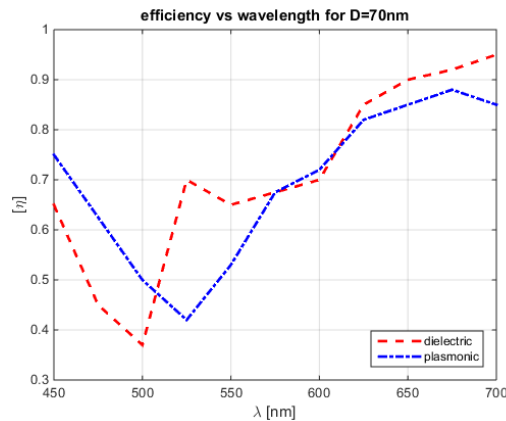


Figure 21: Efficiency curves of dielectric and plasmonic antenna [41, 72]

A hybrid nanoantenna consists of a pair of metallic nanoparticles. Such antenna enhances the spontaneous emission rate of an emitter placed between them, and a dielectric (TiO_2) microsphere needed to effectively collect radiated light into a narrow beam [27]. This nanoantenna combines the advantages of metallic and dielectric nanoantennas resulting in good directive properties and in a significantly enhancement of the confined field [27].

1.4 – Fabrication

The fabrication of optical nanoantennas requires reliable and reproducible structuring techniques with a typical resolution below 10 nm, in order to define exactly critical dimensions such as feed-gap size or antenna arm length. This is because the resonances of optical nanoantennas depend on the exact geometry and dimensions [26]. Several nanofabrication approaches have been applied in the literature to experimentally realize optical nanoantennas. In particular, there are two different kinds of methods for manufacturing nanomaterials either top-down or bottom-up. Top-down approach typically transforms larger objects into nanoscale material components. It requires a large amount of material, therefore it is not suitable for mass production. The two main top-down nanofabrication approaches are Electron Beam Lithography (EBL) and Focused Ion Beam Milling (FIB). They usually start from a thin multi-crystalline metal film on top of an optically transparent but electrically conductive substrate. Furthermore, they are able to fabricate large array of identical nanostructures with well-defined orientations and distances. Both of these top-down methods are serial techniques and require expensive equipment. The bottom-up approach is the fabrication of nanoscale objects by building them up from

atomic and molecular components. It takes advantage of chemical synthesis and self-assembly of metal nanoparticles in solution that can be put on any substrate. However, this approach often requires precise size selection and assembly strategies to create nontrivial structures [26]. Recently, a combination of both approaches has been employed. This technique allows to fabricate high-definition nanostructures with fine details over large areas [73].

1.4.1 – Electron Beam Lithography (EBL)

Electron Beam Lithography is one of the most famous techniques to fabricate nanoantennas on a

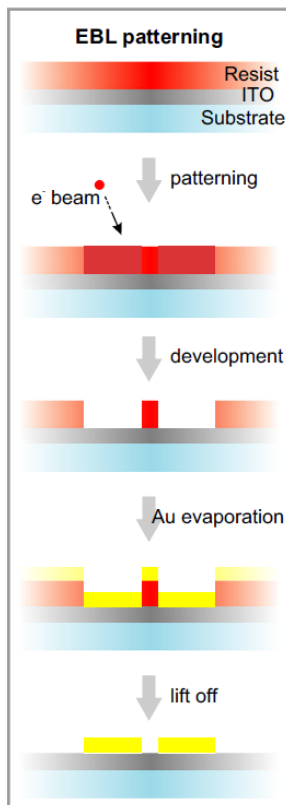


Figure 22: EBL [26]

substrate. A typical implementation of EBL is shown in Figure 22. A high-resolution electron-sensitive resist, such as Poly methyl methacrylate (PMM), is patterned by means of a focused electron beam. Electron beams can focus up to nanoscale size and can be deflected either electromagnetically or electrostatically. When an electron beam enters the polymer layer, it loses its energy via elastic and inelastic collisions. Elastic collisions cause deflection in the direction of the electron beam, while inelastic collisions cause a decrease in the energy of beam. While the electrons penetrate the solid, they spread out producing a transverse electron flow normal to the incident beam direction. Due to this spread, it can be noted an exposure of the resist at points remote from the point of initial electron incidence. The patterns are then developed and selectively removed. A thin layer of metal with the desired thickness is then evaporated covering both the voids and the remaining resist. The voids are covered by means of lift-off technique. Finally, the sample is subjected to a solvent which removes the remaining resist and leaves the metal structures in the voids unchanged. An appropriate software then controls the pattern. This software controls different aspects of pattern and transfer pattern data to the beam deflection systems. The spatial

resolution of the pattern typically obtained by EBL is usually below 5 nm. Moreover, the electron beam cannot cover large area, so typically for EBL a mechanical stage has to move during the process. It means that the stage stays steady until the beam can write a part of pattern, then the stage moves to the other part needed to be exposed. In order to increase the stability of the fabricated structures during the lift-off, a thin adhesion layer of titanium or chromium, typically below 5 nm, is often used. Such layers, however, can significantly increase the damping of the surface plasmon [26, 74].

1.4.2 – Focused Ion Beam Milling (FIB)

Focused Ion Beam milling is another top-down technique for the realization of optical nanoantennas. This method has been applied since the development of the liquid metal ion (LMI) source in 1975. It is able to build high-resolution patterns and to produce microscale electronic devices. Moreover, several advantages can be attributed to FIB method, such as high resist exposure sensitivity and its negligible ion scattering within the resist along with low back scattering from the substrate. However, this technique shows some drawbacks which limits its application, such as lower throughput and extensive substrate damage. Therefore, FIB is usually employed in industrial manufacturing of components.

Figure 23 shows a typical implementation of FIB. Two different kinds of FIB etching can be applied, physical sputtering etching and chemical assisted etching. The localized sputtering of material uses accelerated Ga ions extracted from a liquid metal ion source. The emitted ions are accelerated with a higher energy, focused into a beam with a few nanometer spot and scanned over a conductive substrate in order to bombard the area to be etched, to erode material from the sample and to produce a desired pattern. Ion collisions generate a cascade inside the solid removing atoms from their equilibrium position and giving rise to a local surface erosion. Chemical etching is based on chemical reactions between the substrate and gas molecules absorbed on the substrate. This method exhibits some advantages such as an increased etching rate and a little residual damage. FIB nanofabrication couples nanoscale resolution with the high versatility of the patterns. The broad applicability to almost different materials and the very good resolution are the two main advantages of FIB method. For these reasons, this technique allows to fabricate the prototype surface nanostructures and gaps in the range of 10 nm - 20 nm. On the other hand, since FIB is a sputtering process, part of the sputtered material can be redeposited back to the surface and contaminate the already fabricated structure. Therefore, it is crucial to design an accurate pattern and to have a correctly writing sequence. Although FIB sputters away the material, the accelerated ion beam can cause a Ga implantation into the target metal film and substrate [26, 75].

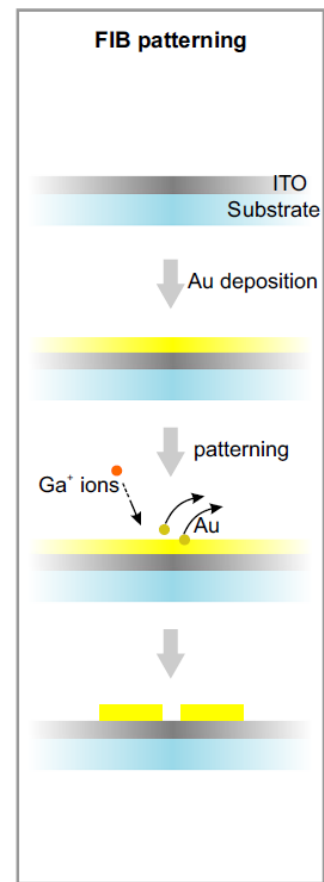


Figure 23: FIB [26]

1.4.3 – Nano-imprint Lithography (NIL)

Nano-imprint Lithography (NIL) is a possible low-cost and high-throughput alternative of both EBL and FIB techniques. The NIL process uses a hard mould that contains all the surface topographic features to be transferred onto the sample and is pressed under controlled temperature and pressure into a thin

polymer film, thus creating a thickness contrast [26, 76]. The resolution of patterns is usually on the order of 10 nm. In order to reduce the cost of mould fabrication and to achieve patterning over large areas at lower pressures, soft-nanoimprinting techniques have also been developed. These techniques are based on polymeric flexible stamps replicated from a single master mould [77]. In future, NIL might become the ideal technique for low-cost and highly reproducible realization of optical antennas array covering large areas.

Conclusion

Several types of optical nanoantennas have been introduced and discussed in this chapter. In particular, the difference between metallic and dielectric nanoantennas have been examined.

Metallic nanoantennas works in a range of frequency close to the plasmonic resonance of metals used. The main structures of metallic nanoantennas have been investigated. Dipole nanoantenna consists of two nanoparticles with a gap in between. It is able to generate strongly localized field when an electromagnetic wave irradiates its surface. Furthermore, it offers several advantages in terms of easy production, fine-tuning of the operation mode and high confinement of electric field in the gap. Bowtie nanoantennas consist of two triangles facing each other from their apices and with a gap in between. They are characterized by a broad bandwidth and by a higher field enhancement in the gap compared with dipole nanoantenna because of larger lightning-rod effect at apex. However, they exhibit a lower confinement factor compared to a dipole nanoantenna due to a larger amount of metal used for their fabrication. Spiral antenna reveals planar structure, circular polarization and broadband characteristics. The structure requires a more complicated manufacturing process and a bigger quantity of metal for both the antenna and the ground plane. Therefore, the power losses in this structure are much higher. Yagi-Uda nanoantennas are narrowband devices that work at frequencies close to those of the plasmon resonances, determined by the dimensions of the antenna elements. They are directive antennas and have a high efficiency in terms of directivity and losses that occur throughout the antenna while it is operating at a given frequency. However, they suffer from the absorption losses in metals in the visible and infrared range.

Dielectric nanoantennas are made of optically transparent materials, such as semiconducting materials. They exhibit smaller dissipative losses in the material with enhanced magnetic response in the visible. Typically, dielectric nanoantennas consist of spherical particles and sometimes of rods and disks. The main structures of dielectric nanoantennas have been investigated. Whispering gallery antennas consist of dielectric microspheres and possess good directional capabilities by virtue of their large surface area. However, they have a weak influence on the spontaneous relaxation rate of the emitter. Huygens optical element, consisting of a single dielectric nanoparticle, can be considered for the creation of totally dielectric nanoantennas with good directional properties. Dielectric Yagi-Uda

nanoantenna consists of more dielectric nanoparticles of equal size and exhibits the radiation efficiency that slowly decreases with the distance between the elements.

Finally, the main techniques used for the fabrication of optical nanoantennas have been described. They include Electron Beam Lithography and Focused Ion Beam milling that are top-down approaches requiring expensive equipment and, therefore, are not suitable for mass production. However, the top-down approaches are able to fabricate large array of identical nanostructures with well-defined orientations and distances. The bottom-up approaches take advantage of chemical synthesis and self-assembly of metal nanoparticles in solution that can be put on any substrate. However, these approaches often require precise size selection and assembly strategies to create nontrivial structures.

The analysis of the two main types of nanoantennas and of their main structures have allowed to choose the particular structure studied in this work. Especially, to the purpose of this work the structure chosen has been the dipole nanoantenna that offers easy production, fine tuning, high confinement of electric field in the gap and less dissipative metal loss. The material chosen has been aluminium because it shows a reasonable efficiency values over the whole frequency band of interest. Moreover, it has a transparent oxide.

CHAPTER II – ANALYSIS OF THE MAIN OPTICAL NANOANTENNA PARAMETERS

A numerical analysis of the dipole nanoantenna in order to acquire the main parameters is fulfilled in this section. First, the main theoretical methods of simulation and several commercially simulation tools will be overviewed. A description of the software used in this work and of the simulated structure will then be made. Finally, the main results of simulations of the dipole nanoantenna will be summarised. In particular, the evaluation of the internal nanoantenna impedance will be detailed; the method used in order to evaluate the effective nanoantenna area will be described; the analysis of the main electrical parameters, i.e. the Poynting vector and the available power on the load matching conditions, will be made.

2.1 – Simulations

This subsection considers the numerical analysis of dipole nanoantenna. At the beginnings, the fundamental theoretical techniques widely used for the computational electromagnetics will be discussed. Several simulation tools implementing these techniques will then be overviewed. Finally, a description of the software used in this work and of the simulated structure will be made.

2.1.1 –Modelling techniques

In order to design a nanoantenna or to study the interaction between nanometric structures and electromagnetic waves, a determination of the electromagnetic field distribution close to the structure and the relative radiation properties are needed. The variation of the antenna geometric parameters and the choice of appropriate materials make possible to obtain a plasmonic resonance frequency in the range of interest. To this purpose, a simulation of the nanostructures assumes a greater interest. Two main types of methods of simulation can be identified: Integral Equation (IE) and Differential Equation techniques [78]. Integral Equation methods make use Maxwell's equations in integral equation form in order to formulate the electromagnetic problem in terms of unknown currents flowing on the object to be described. These currents are related to the fields by means of a Green's function tensor, which includes the electromagnetic influence of the complete background environment. Therefore, the problem formulation covers the entire surrounding space without making any approximations and allows to evaluate the electromagnetic fields in every point. One of the most important integral equation technique is the Method of Moment (MoM). This method allows a functional equation to be transformed in a dense matrix equation, which can be solved using standard matrix algebra technology. The boundary equations can be solved applying Volume Integral Equations (VIE). IE-MoM is usually applied in the frequency

domain; therefore, the solution has to be determined at each frequency of interest. IE formulations are very power free because they minimize the number of unknowns for a certain problem. However, the resulting dense MoM matrix needs to a large memory demand. IE-MoM satisfies the radiation conditions by the Green's function. The latter allows multi-layered structures to be analysed, which are of interest in the analysis of planar antennas. The only elements, which cannot be described by means of the Green's function, are local scattering objects with medium or small dimensions. The IE-MoM technique becomes inferior to the differential equation techniques only in the case of complex environment. Differential equation methods are derived directly from Maxwell's curl equations or the Helmholtz wave equations with little analytical preprocessing. The main differential equation-based methods are the Finite Element Method (FEM) and the Finite-Difference Time Domain method (FDTD). Differential equation methods are usually applied for modelling small full three-dimensional volumes that have complex geometrical details. The reason is that the number of unknowns is proportional to the volume and the resolution considered. Furthermore, these methods require a discretization of the entire space under consideration. Therefore, they are less suitable for open problems, which require infinite space. This problem can be solved employing truncating techniques such as Absorbing Boundary Conditions and Perfectly Matched Layers (PML). The Finite Element Method (FEM) is a differential equation method based on solving partial differential equations. It subdivides the space in elements, for example tetrahedral. The fields inside these elements are expressed in terms of a number of basic functions. These expressions are inserted into the functional of the equations and the variation of the functional is null. This yields a matrix eigenvalue equation whose solution yields the fields at the nodes. The Finite-Difference Time Domain (FDTD) technique is one of the oldest differential equation methods. The main property of this method is that, at any point in space, an updated value of the E/H-field in time is dependent on the stored value of E/H-field and the numerical curl of the local distribution of H/E-field in space. The interaction of an electromagnetic wave with the matter can be mapped into the space lattice by assigning appropriate values of permittivity to each electric field component and permeability to each magnetic field component. For this reason, FDTD is extremely versatile [78-79]. The Finite Integration Technique (FIT) consists of a discrete reformulation of Maxwell's equations in their integral form. It allows to simulate real-world electromagnetic field problems with complex geometries. In the time-domain, the resulting discrete grid equations of FIT are often identical to the discrete equations derived with the classical Finite-Difference Time-Domain (FDTD) method [78].

2.1.2 –Software tools

In order to design a nanoantenna, the choice of the software tool, which implements one or more solution methods of Maxwell's equations in the range of interest, is crucial. This choice depends on

many factors, such as costs, computational times and spaces, solution techniques, integration with other software or databases. In particular, most important is the geometry of the analysed structure because it can change the resolution efficiency of a certain method [80]. The main commercial and academic software tools are CST Microwave Studio (CST MWS), Ansoft's HFSS, FEKO, COMSOL Multiphysics, Lumerical and MAGMAS 3D. CST MWS is based on the finite integration technique (FIT). It allows to choose the time domain as well as the frequency domain approach. The Time Domain Solver calculates the broadband behaviour of electromagnetic devices in one simulation run with an arbitrarily fine frequency resolution. A problem sometimes observed with CST is a ripple in the frequency response in case the tool settings are not appropriate [78, 80]. HFSS is based on a 3D FEM solution of the electromagnetic topology under consideration. The purpose of this tool is to extract parasitic parameters, to visualize 3D electromagnetic fields and to generate SPICE models. Furthermore, automatic adaptive mesh generation and refinement characterize it [78, 80]. FEKO is based on the IE-MoM method. The matrix elements are computed using a mixed-potential formulation and a spatial domain approach. The solver can model arbitrary 3D structures. The surface of the structure is discretized using triangular mesh, while tetrahedral mesh is used for volumetric discretization [77, 79]. COMSOL Multiphysics is a finite element code which allows to solve partial differential equations in 2D and 3D domains. The geometry, material parameters and boundary conditions of the problem can be set up in a graphical user interface (GUI). After defining boundaries and domains, the mesh has to be generated. This includes the selection of the basis functions' order and the choice of the order of the curved mesh elements [80]. Lumerical FDTD Solutions is based on the FDTD technique. It uses a rectangular mesh. The fundamental simulation quantities (material properties and geometrical information, electric and magnetic fields) are calculated at each mesh point. By default, the simulation mesh is automatically generated. To maintain accuracy, the meshing algorithm creates a smaller mesh in high index. In some cases, it is also necessary to manually add additional meshing constraints [80]. MAGMAS 3D is the IE-MoM code developed at the Katholieke Universiteit Leuven, Belgium. The matrix elements are computed using a hybrid dyadic-mixed potential formulation and a combined spectral-space domain approach. This allows to perform a large part of the computation procedure for these matrix elements analytically in the spectral domain. Surface and volume currents are decomposed in horizontal and vertical currents, which are both expanded using generalized rooftop functions. A full mesh control of combined rectangular and triangular mesh cells is available in manual meshing mode. The exact coordinates and dimensions can be set for every single mesh cell. A Graphical User Interface is available [78, 81].

2.1.3 – Software CST Studio Suite

The software chosen for the design of optical nanoantennas has been CST Studio Suite. It provides a good compromise between costs and performances. CST Studio Suite is an electromagnetic simulation software that offers most accurate and efficient computational solutions for electromagnetic designs. It includes several tools for the design and optimization of devices operating in a wide range of frequencies. The tool used for the purpose of this work is the CST MicroWave Studio (MWS). It is an innovative tool for the fast and accurate 3D simulation of high frequency devices, such as antennas, and market leader in the Time Domain simulation. Furthermore, it allows to choose the time domain and frequency domain solver. The Time Domain Solver calculates the broadband behaviour of electromagnetic devices in one simulation run with an arbitrarily fine frequency resolution. The transient analysis of an antenna can be done utilizing the hexahedral mesh type. The automatic mesh generator detects the important point inside the structure and locates mesh nodes there. The user can be manually add fixpoints on a structure, as well as, control the number of mesh lines in each coordinate relatively to the specified wavelength. Energy based adaptation of the mesh allows to refine it in a predefined number of passes. As a consequence, a mesh refinement of sophisticated design features can be provided and a longer overall simulation time can be required. Real time domain simulation is useful for studying the field propagating through a component. Field results for many frequencies (for example 100 farfield samples) can be derived from one single simulation run [82].

2.1.4 – Simulated structure

Several issues have been taken into account for the study and design of optical nanoantennas. These devices have to be able to efficiently capture the polarized incident radiation. This can be achieved using an appropriate structure. The nanoantenna structure, in particular the metals used as conductor and the dimensions of nanoantenna, also influences one of the most important nanoantenna parameter, the radiation efficiency. This is the ratio between the radiated power and the power injected at the terminals. Therefore, an accurate choice of materials and design of nanoantenna is most important for its efficiency. The structure chosen for the purpose of this work is the dipole nanoantenna that offers easy production, fine tuning, high confinement of electric field in the gap and less dissipative metal loss. The metal chosen is aluminium because it shows a reasonable efficiency values over the whole frequency band of interest. Moreover, it has a transparent oxide. The numerical analysis has been performed with CST MWS, in particular the Time Domain solver. The mesh used for the simulation has been the hexahedral mesh type, which allows most accurate computational solutions but longer simulation time. The number of cells for wavelength is about 20. In particular, the simulation time has been about 8-12 hours using a workstation with the following features: Intel ® Core™ 15-4590 CPU @ 3.30 GHz and RAM 8 Gb. The wavelength range of interest is between 300 nm and 1200 nm, which corresponds to a frequency

range of 250 THz – 1000 THz. This is the range commonly used in literature since it covers the visible and infrared interval. The simulated dipole nanoantenna consists of a width W (in z direction) and of a height H (in y direction), both equal to 40 nm. The arm length L varies in a range from 100 nm to 350 nm in steps of 50 nm. The gap G is fixed to 10 nm [56, 83-84]. Figure 24 shows a sketch of the dipole structure for arm length equal to 150 nm.

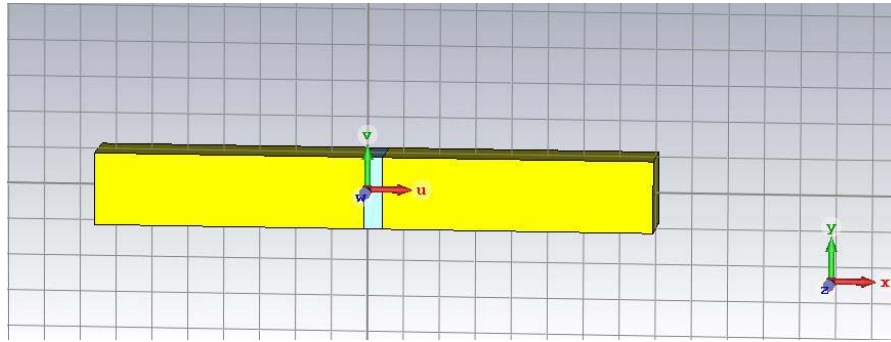


Figure 24: Sketch of simulated dipole nanoantenna for L equal to 150 nm

The reference frequency is equal to 350 THz, which is close to the plasmonic resonance frequency of the aluminium. All the simulation has been made at a frequency of 250 THz, 350 THz and 1000 THz. In particular, the frequency range used in CST has been equal to 150 THz – 1500 THz in order to best analyse the end of the band of interest 250 THz – 1000 THz, whereas the frequency monitors have been applied at a frequency of 250 THz, 350 THz and 1000 THz respectively. During the simulation, the excitation signal has been a default Gaussian pulse in a range of frequency from 250 THz to 1000 THz, as shown in Figure 25.

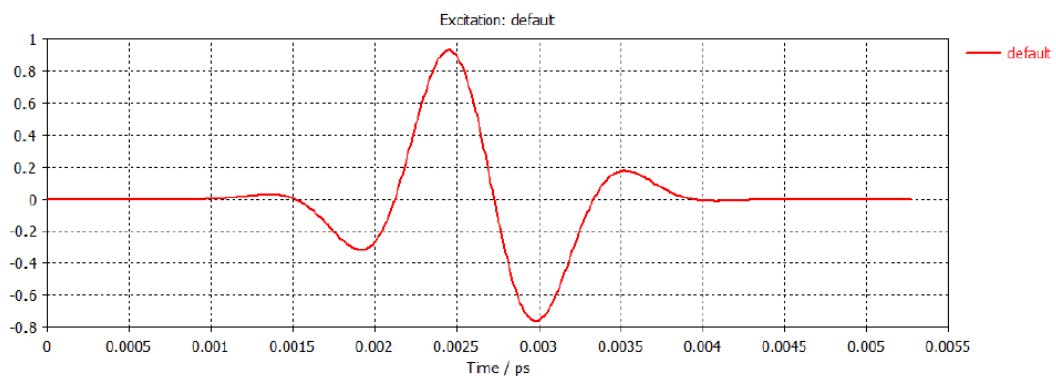


Figure 25: Excitation signal

The nanodipole has been irradiated by circularly polarized plane wave at a frequency of 250 THz, 350 THz and 1000 THz, respectively. The electric field along x direction have an arbitrary amplitude of 1000 V/m.

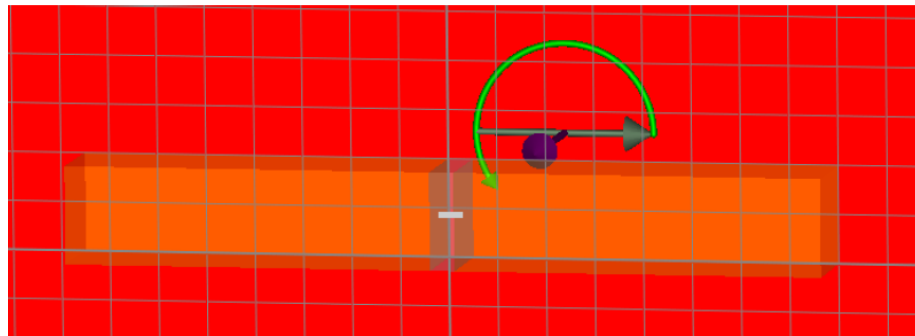


Figure 26: Sketch of circularly polarized plan wave

In order to obtain the electric field enhancement and the voltage in the gap, a discrete port of 25 Ω , 50 Ω , 75 Ω and 1000 Ω respectively has been introduced within the gap, as sketched in Figure 27.

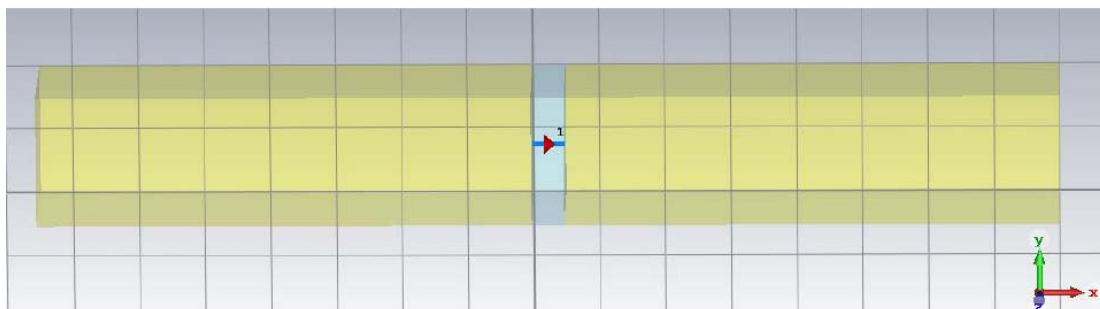


Figure 27: Discrete port in the gap

Figures 28 and 29 show the electric field enhancement of dipole in the gap.

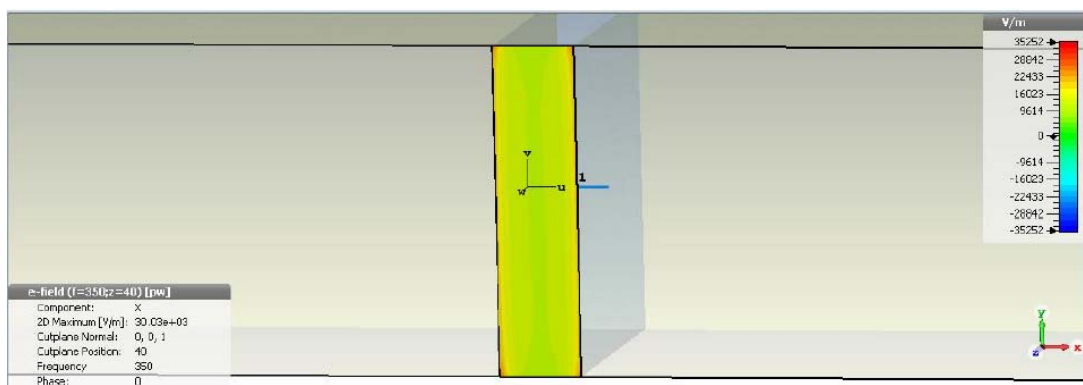


Figure 28: Electric field enhancement at interface dipole-gap

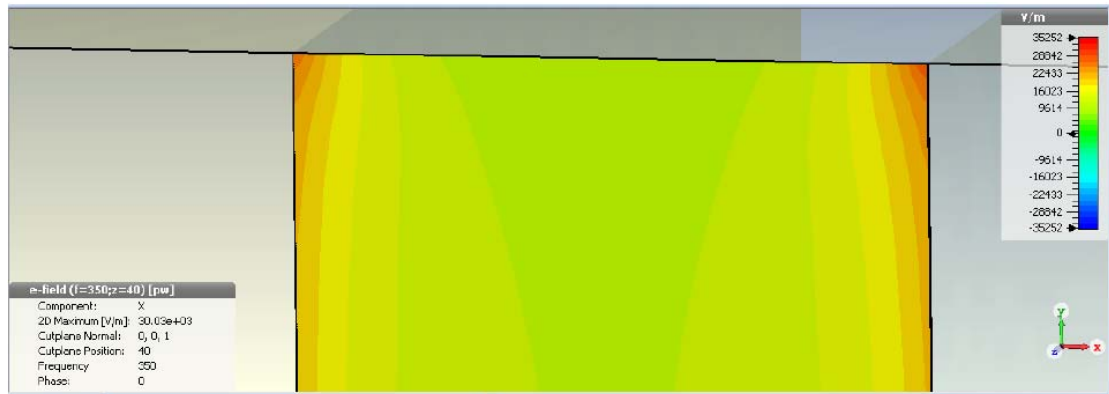


Figure 29: Zoom of electric field enhancement at the interface between dipole and gap

As it can be noted in Figure 29, the enhancement of electric field in the gap is mainly evident in correspondence of the interface between the gap and the surface. This is due to the greater plasmonic resonance effect at the interface between the metal and the dielectric.

All the simulations of the nanodipole have been considered in vacuum. The presence of the substrate, typically glass, only influences the efficiency of the antenna. In particular, in this case the efficiency is lower than in the case of the vacuum [56].

2.2 – Simulation results

This subsection summarizes the main results of simulations of the dipole nanoantenna. First, the evaluation of the internal nanoantenna impedance are detailed. The method used in order to evaluate the effective nanoantenna area will then be described. Finally, the analysis of the main electrical parameters, i.e. the Poynting vector and the available power on the load matching conditions, will be made.

2.2.1 – Nanoantenna impedance evaluation

The antenna operating in receiving mode can be represented by a voltage source, V_{open} , and an impedance in series $Z_A = R_A + jX_A$. V_{open} is the open circuit voltage at the end of the antenna when the load is not connected. Z_A is the antenna impedance characterized by an antenna reactance X_A , which is equal to zero at resonant frequency, and an antenna resistance R_A defined as the sum of the radiation resistance R_{rad} and the loss resistance R_{loss} . R_{rad} models the radiated power and depends on the antenna geometry and on the surface current distribution; R_{loss} models the conductive and dielectric losses and depends on the resistive losses of antenna material. In order to reduce ohmic dissipation in the antenna and then to have a greater radiation efficiency, the radiation resistance has to be larger than ohmic resistance [24, 85-87]. The proposed analysis has general validity and can be performed, following the proposed approach, on different antennas topologies. The internal nanodipole impedance has been evaluated by simulation at a frequency of 250 THz, 350 THz and 1000 THz. This is the range commonly

used in literature since it covers the visible and infrared interval. On the other hand, the nanodipole is expected to have a higher bandwidth; for this reason, the choice of this interval will give an under estimation of the energy. As mentioned above, the numerical analysis has been performed with a commercial full-wave 3D electromagnetic simulator CST Studio Suite 2016. During the simulations, the excitation signal was a default Gaussian pulse in the range of frequency from 250 THz to 1000 THz. The nanodipole has been irradiated by a circularly polarized plane wave at a frequency of 250 THz, 350 THz and 1000 THz, respectively. The electric field along x direction had an arbitrary amplitude of 1000 V/m. First, the open circuit voltage V_{open} at the end of the antenna when the load Z_{LA} is not connected has been calculated. Since the value of the internal nanodipole impedance is in a range from 50 Ω to 100 Ω , the value of V_{open} has been evaluated in correspondence of Z_{LA} equal to 1000 Ω . Then, the voltage V_u occurring when the load Z_{LA} is connected to the antenna has been evaluated. In order to evaluate V_u , Z_{LA} has been fixed equal to 25 Ω , 50 Ω and 75 Ω , respectively. Figure 30 shows the antenna equivalent circuit considered in order to calculate the internal nanoantenna impedance Z_A .

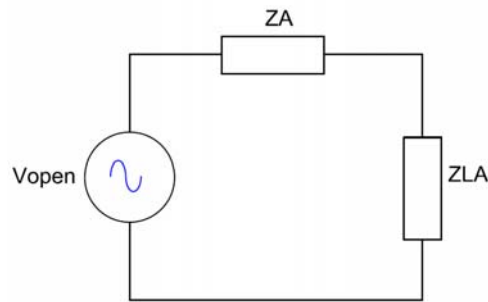


Figure 30: Circuit for calculation of internal nanoantenna impedance

The internal nanoantenna impedance Z_A can be expressed as

$$Z_A = \left(\frac{V_{open}}{V_u} - 1 \right) \cdot Z_{LA} \quad (1)$$

Figures 31 and 32 show the curves of V_{open} and V_u when Z_{LA} is equal to 50 Ω and their FFT, respectively.

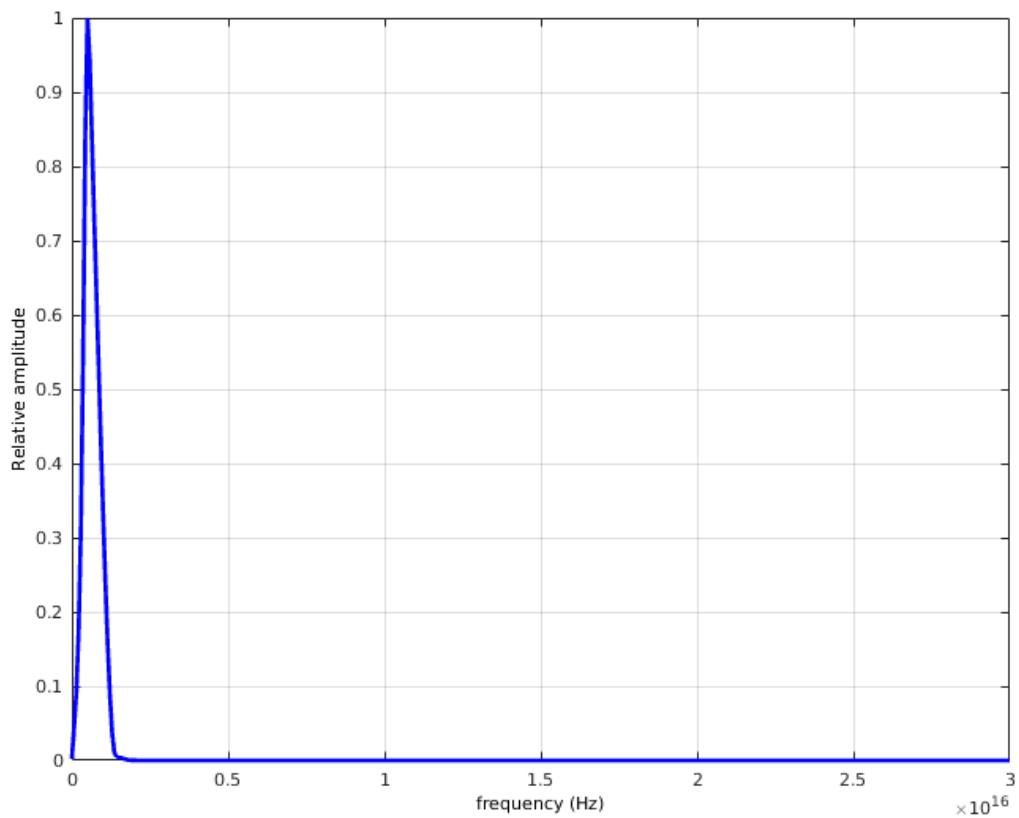
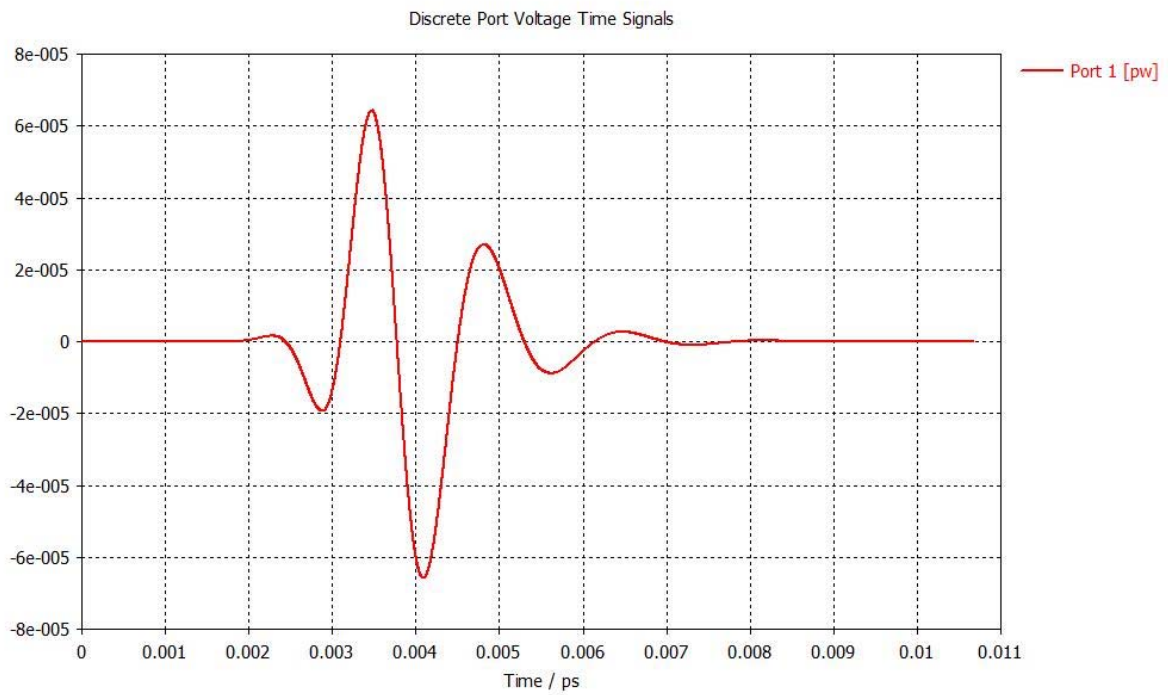


Figure 31: a) Open circuit voltage at the end of dipole when load is not connected; b) FFT

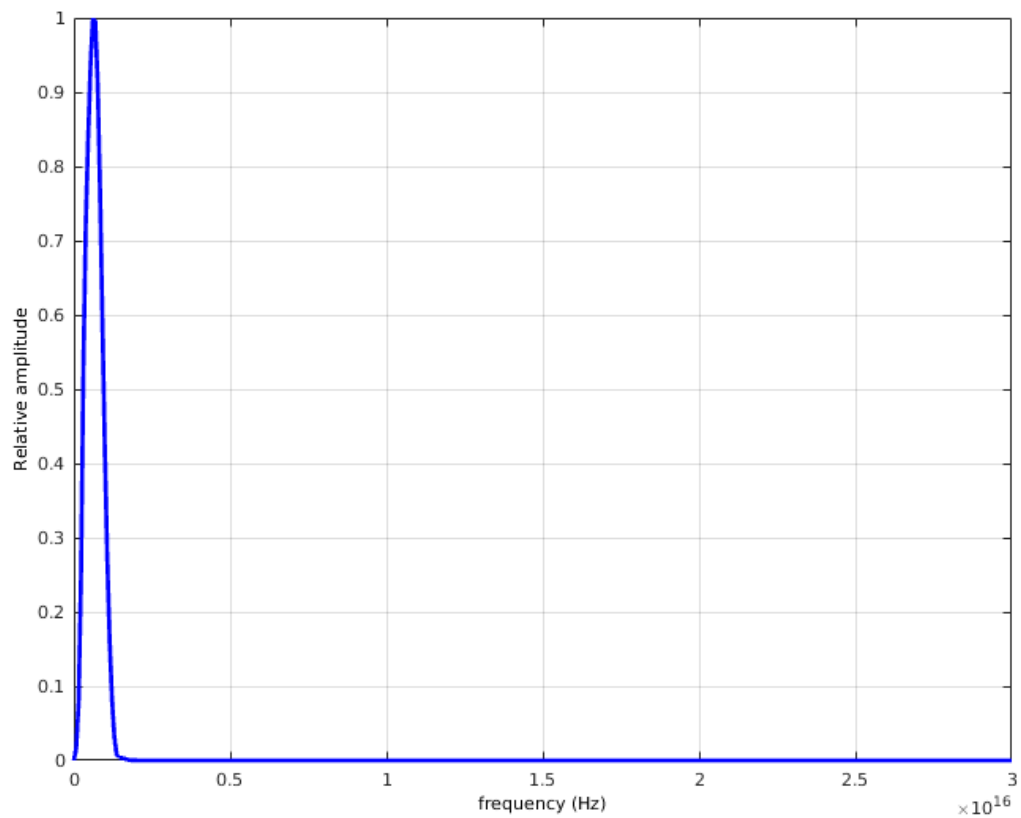
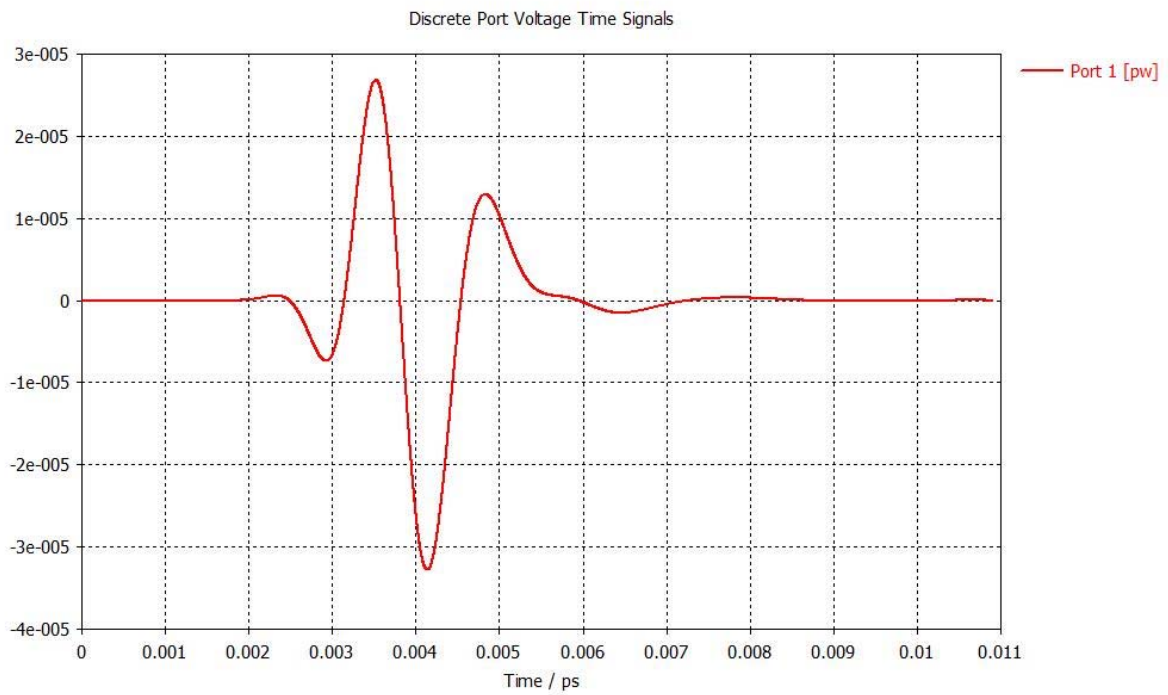


Figure 32: a) The voltage occurring when the load Z_L is connected to the dipole; b) FFT

These curves are relative to a dipole whose arm length is equal to 150 nm. The curves of V_{open} and V_u for each other dipole have the same trend; the difference is only in the peak values. Considering the maximum values of V_{open} and of V_u and Z_{LA} equal to 25 Ω , 50 Ω and 75 Ω , the internal nanoantenna impedance has been obtained [43, 88-89]. Table 1 shows the values of the internal nanodipole impedance evaluated by simulation at a frequency of 250 THz, 350 THz and 1000 THz for dipole arm lengths L varying between 100 nm and 350 nm in steps of 50 nm. It can be noted that the waveforms of the V_{open} and of the V_u differ only for a scale factor. These results confirm that the internal nanoantenna impedance can be considered as resistive. Therefore, the imaginary part of the impedance has been neglected since it results much lower than the resistive part. The values of the nanoantenna impedance shown in Table 1 are in agreement with the main values of the nanoantenna impedance in the literature that are in a range of 50 Ω – 100 Ω [61-62, 84-87].

Table 1: Internal nanodipole impedance values at 250 THz, 350 THz and 1000 THz

<i>L [nm]</i>	<i>Impedance [Ω] at 250 THz</i>	<i>Impedance [Ω] at 350 THz</i>	<i>Impedance [Ω] at 1000 THz</i>
100	69.85	69.64	69.58
150	69.26	69	69.18
200	69.15	69.04	69.27
250	66.47	66.3	66.59
300	62.41	62.47	62.49
350	62.19	62.05	62.17

Moreover, it can be noted that the difference in percentage between the values at 1000 THz, 350 THz and 250 THz is about 0.03% - 0.44%. As a consequence, the internal nanodipole impedance has been approximated to be constant all over the range of frequency from 250 THz to 1000 THz, which corresponds to a range of wavelength from 300 nm to 1200 nm. The values chosen are calculated at the frequency of 350 THz.

2.2.2 – Effective area evaluation

A parameter usually used in the antenna theory is the effective area of antenna A_{eff} . This is the ratio between the received power in the case of matching with the load and the incident power density [24, 83]. The effective area A_{eff} can be calculated in terms of V_{open} , of the incident electric field E_i and of Z_A with the formula (2)

$$A_{eff} = \frac{V_{open}^2 Z_0}{4E_i^2 Z_A} \quad (2)$$

The nanoantenna effective area A_{eff} has been evaluated by simulation at a frequency of 250 THz, 350 THz and 1000 THz. The nanodipole has been irradiated by circularly polarized plane wave with an arbitrary amplitude of 1000 V/m at a frequency of 250 THz, 350 THz and 1000 THz, respectively, and electrical field along x direction. Considering the values of V_{open} and of the internal nanodipole impedance Z_A , the value of the intrinsic impedance of free space Z_0 equal to 377Ω and the value of the incident electric field E_i of 1000 V/m, the values of nanodipole effective area A_{eff} has been obtained [88-89]. Table 2 shows the results.

Table 2: Effective nanodipole area values at 250 THz, 350 THz and 1000 THz

L [nm]	Effective area at 250 THz [10^{-15} m^2]	Effective area at 350 THz [10^{-15} m^2]	Effective area at 1000 THz [10^{-15} m^2]
100	5.5927	5.5926	5.6562
150	6.1675	6.1665	6.2519
200	4.8427	4.8377	4.902
250	3.2488	3.2417	3.2718
300	2.5645	2.5583	2.5701
350	2.5307	2.5264	2.5412

It can be noted that the difference in percentage between the values at 1000 THz, 350 THz and 250 THz is in a range from 0.22% to 1.4%. Therefore, the effective nanodipole area has been considered constant all over the range of frequency from 250 THz to 1000 THz for given dipole arm length. The values chosen are at the frequency of 350 THz.

2.2.3 – Nanoantenna electrical parameters evaluation

In order to obtain the available power on the load matching conditions, the Poynting vector has to be calculated. In the case of solar energy harvesting, the Sun has been characterized by a blackbody source with temperature equal to 5778 K. The energy radiated by the Sun follows the Planck's blackbody radiation formula:

$$W_\lambda = \frac{2\pi hc^2}{\lambda^5 (e^{\frac{hc}{\lambda kT}} - 1)} \quad (3)$$

where h is the Planck's constant equal to $6.63 \cdot 10^{-34}$ [J s] and k is the Boltzmann's constant equal to $1.38 \cdot 10^{-23}$ [J/K]. It should be noted that formula (3) is expressed in [W/m²/unit wavelength in meters], its shape depends on temperature and wavelength. In order to evaluate the total energy emitted by the

Sun, formula (3) can be multiplied for the Sun surface. Since the energy coming from the Sun travels for about $150 \cdot 10^6$ km before encountering the Earth's atmosphere, and remains practically unchanged, the energy on the Earth is obtained by dividing by the area of the surface whose radius is the distance Sun-Earth. Since the surface of the Sun is given by $\pi \cdot (\text{Sun_radius})^2$ and the surface of the sphere having the Sun as center tangential to the Earth is $\pi \cdot (\text{distance_Sun_Earth})^2$, formula (3) must be scaled of a coefficient equal to $C=2.164 \cdot 10^{-5}$ [41]. Nanoantennas are characterized by the radiation efficiency whose values depend on the wavelength.

$$\eta^{rad} = \frac{P^{rad}}{P^{inject}} = \frac{P^{rad}}{P^{rad} + P^{loss}} \quad (4)$$

Figure 33 shows the efficiency versus wavelength of aluminum dipole antennas characterized by an arm length in a range from 100 nm to 350 nm. These curves are taken from [56]. It has to be noted that the efficiency depends on the frequency, and it influences the calculation of the effective value of the Poynting vector on the antenna.

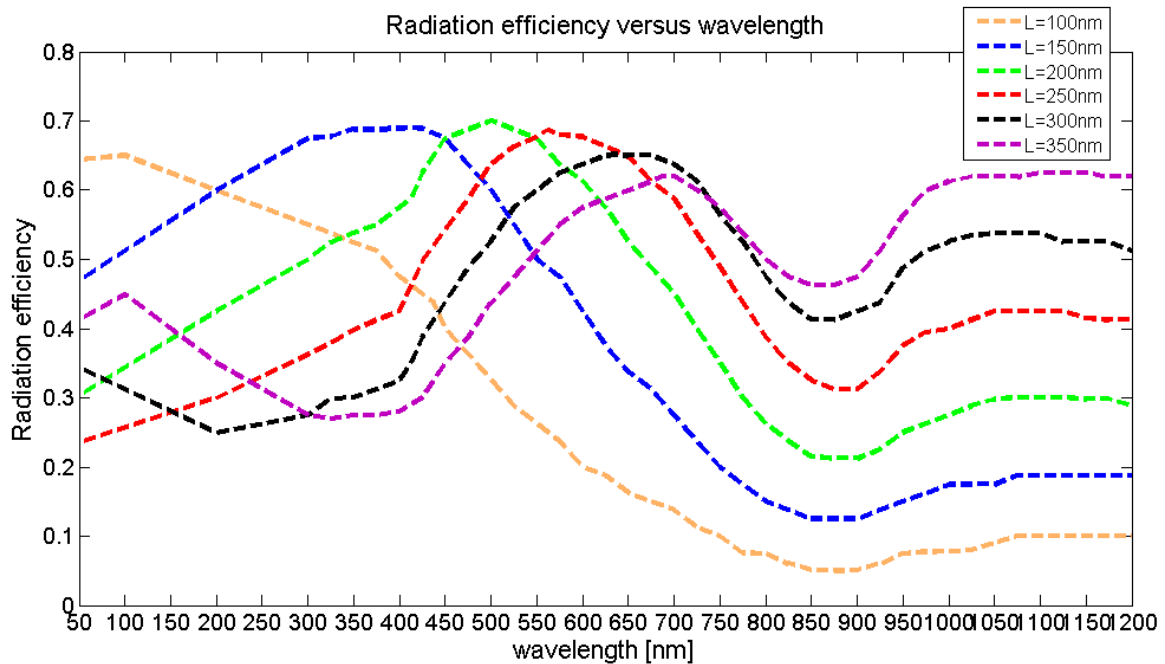


Figure 33: Radiation efficiency versus wavelength, for dipole arm length in a range from 100 nm to 350 nm [56]

The Poynting vector in the ideal case can be calculated integrating (3) in the operating nanoantenna range between 300 nm and 1200 nm, equivalent to a frequency range of 250 THz ÷ 1000 THz, at the temperature of the Sun equal to 5778 K.

$$S = \int_{\lambda_{\min}}^{\lambda_{\max}} W_{\lambda}(\lambda, T) d\lambda \quad (5)$$

This range is commonly used in the literature because it covers the visible and infrared interval. In practice, the efficiency shown in Figure 33 must be taken into account. For this reason, the actual Poynting vector has been obtained as:

$$S' = \int_{\lambda_{\min}}^{\lambda_{\max}} W_{\lambda}(\lambda, T) \eta^{rad}(\lambda) d\lambda \quad (6)$$

The available power on the load matching condition has been evaluated as:

$$P = A_{eff} \cdot S' \quad (7)$$

Table 3 shows the values of the actual Poynting vector and the corresponding power on the load in matching condition of the dipoles with arm length from 100 nm to 350 nm.

Table 3: Poynting vector and optimal power

<i>L [nm]</i>	<i>Actual Poynting vector <S'> [W/m²]</i>	<i>Power P [pW]</i>
100	239.00	1.337
150	412.95	2.546
200	500.44	2.421
250	534.45	1.732
300	535.3	1.369
350	517.08	1.306

From the actual Poynting vector, the maximum value of the electrical field has been calculated as:

$$\bar{E} = \sqrt{2 \cdot \langle S' \rangle} \cdot \sqrt{\frac{\mu_0}{\epsilon_0}} \quad (8)$$

where $\sqrt{\frac{\mu_0}{\epsilon_0}}$ is the intrinsic impedance of free space Z_0 equal to 377 Ω . Figure 34 shows the antenna equivalent circuit that has been considered in order to calculate the nanoantenna power.

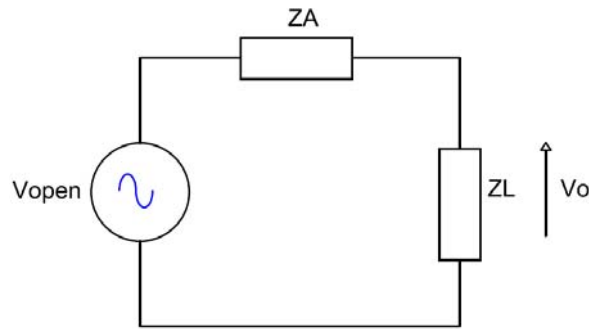


Figure 34: Equivalent circuit for calculation of nanoantenna power

The impedance matching condition between the antenna Z_A and the load Z_L has been assumed. The voltage V_{open} can be expressed as a function of the power

$$V_{open} = \sqrt{4PZ_A} \quad (9)$$

Under matching conditions, the output voltage V_o is equal to $\frac{V_{open}}{2}$. Table 4 shows the values of the incident electric field, of V_{open} and of the output voltage V_o for dipole arm length from 100 nm to 350 nm [88-89].

Table 4: Electrical field, V_{open} and output voltage V_o

L [nm]	E_i [V/m]	V_{open} [μ V]	V_o [μ V]
100	424.51	19.298	9.649
150	558	26.508	13.254
200	614.27	25.857	12.928
250	634.80	21.432	10.716
300	635.31	18.495	9.247
350	624.40	18	9

Conclusion

The analysis of the main nanoantenna parameters has been illustrated, in this chapter. At the beginnings, the fundamental theoretical techniques widely used for the computational electromagnetics has been discussed. Two main types of methods of simulation can be identified, Integral Equation (IE) and Differential Equation techniques. Integral Equation methods make use Maxwell's equations in integral equation form in order to formulate the electromagnetic problem in terms of unknown currents

flowing on the object to be described. These currents are related to the fields by means of a Green's function tensor, which includes the electromagnetic influence of the complete background environment. Therefore, the problem formulation covers the entire surrounding space without making any approximations and allows to evaluate the electromagnetic fields in every point. One of the most important integral equation technique is the Method of Moment (MoM). Differential equation methods are derived directly from Maxwell's curl equations or the Helmholtz wave equations with little analytical preprocessing. The main differential equation-based methods are the Finite Element Method (FEM) and the Finite-Difference Time Domain method (FDTD). Differential equation methods are usually applied for modelling small full three-dimensional volumes that have complex geometrical details. The reason is that the number of unknowns is proportional to the volume and the resolution considered. Furthermore, these methods require a discretization of the entire space under consideration. Therefore, they are less suitable for open problems, which require infinite space. This problem can be solved employing truncating techniques such as Absorbing Boundary Conditions and Perfectly Matched Layers (PML). Several simulation tools implementing these techniques have then been overviewed. The main commercial and academic software tools are CST Microwave Studio (CST MWS), Ansoft's HFSS, FEKO, COMSOL Multiphysics, Lumerical and MAGMAS 3D. A description of the software chosen for the design of optical nanoantennas, CST Studio Suite 2016, has been made. This software provides a good compromise between costs and performances. It is an electromagnetic simulation software, which offers most accurate and efficient computational solutions for electromagnetic designs. It includes several tools for the design and optimization of devices operating in a wide range of frequencies. The tool used for the purpose of this work is the CST MicroWave Studio (MWS), in particular the Time Domain solver. It is an innovative tool for the fast and accurate 3D simulation of high frequency devices, such as antennas, and market leader in the Time Domain simulation. The numerical analysis has been performed. The mesh used for the simulation has been the hexahedral mesh type, which allows most accurate computational solutions but longer simulation time. In particular, the simulation time has been about 8-12 hours using a workstation with the following features: Intel® Core™ i5-4590 CPU @ 3.30 GHz and RAM 8 Gb. The wavelength range of interest is between 300 nm and 1200 nm, which corresponds to a frequency range of 250 THz – 1000 THz. This is the range commonly used in literature since it covers the visible and infrared interval. The simulated dipole nanoantenna consists of a width W (in z direction) and of a height H (in y direction), both equal to 40 nm. The arm length L varies in a range from 100 nm to 350 nm in steps of 50 nm. The gap G is fixed to 10 nm. Finally, the main results of simulations of the dipole nanoantenna have been summarized. In particular, the evaluation of the internal nanoantenna impedance has been detailed. The method used in order to evaluate the nanoantenna effective area has then been described. Finally, the analysis of the main electrical

parameters, i.e. the Poynting vector and the available power on the load matching conditions, has been performed.

CHAPTER III – RECTENNA TOPOLOGY

A description of the rectenna topology, in particular the equivalent circuit configuration, is performed in this section. The main types of rectifiers usually employed for the rectification in the range of terahertz will be described. Finally, the diode equivalent impedance will be evaluated.

3.1 – Equivalent circuit configuration

The nanoantenna output is an AC current that has the same frequency of the incident radiation. Therefore, a proper rectifier is usually employed in order to obtain a DC output. The typical block diagram of a rectenna is shown in Figure 35 [35, 41, 44, 63, 90-92].

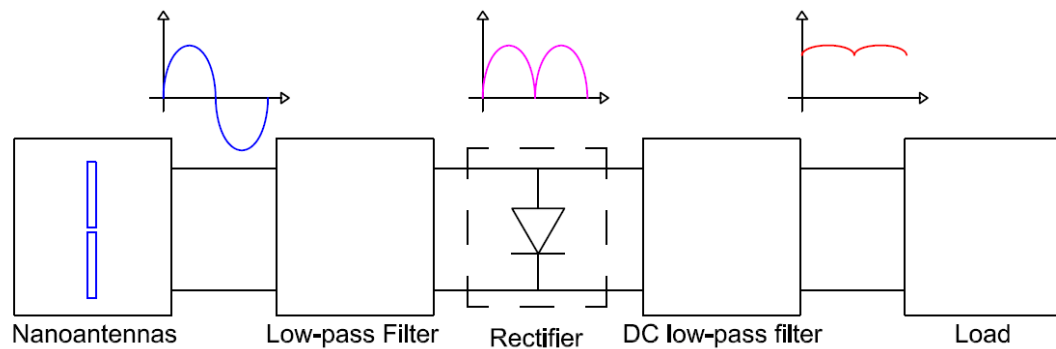


Figure 35: Block diagram of Solar Rectenna

A low-pass filter is placed between the nanoantenna and the rectifier. This device avoids that the radiation of higher harmonics, generated from the rectification of the nonlinear diode, comes back to the nanoantenna resulting in power losses. Furthermore, this filter makes possible the matching between the nanoantenna and the following circuitry [35]. In order to separate the high frequency component from the DC signal, a DC low-pass filter is placed between the rectifier and the load [24]. The equivalent circuit of a solar rectenna consists of the rectifier in parallel with the nanoantenna circuit. The equivalent scheme is shown in Figure 36 [44, 91-92].

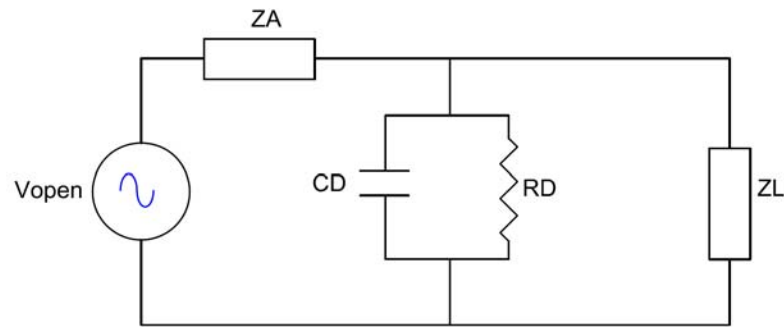


Figure 36: Equivalent circuit of Solar Rectenna

The nanoantenna is shaped as a voltage source V_{open} with an impedance in series Z_A . The rectifier is usually modelled by a junction capacitance C_D , it defines the diode switching time, and a non-linear series resistance R_D . A threshold voltage also characterizes a rectifier. Two main conflicting factors can limit the conversion efficiency of a rectenna, the RC constant and the impedance matching. Every electrical component can be associated with a capacitance and a resistance; the RC product thus determines how quickly a voltage across the device can be change. In order to operate at frequencies in the range of terahertz (approximately 1 PHz), the RC time constant has to very low, of the order of a few femtoseconds. The RC time constant of the rectenna depends on the antenna resistance. Especially, because of the diode resistance and the antenna resistance are in parallel, when the antenna resistance is much less than the diode resistance, the RC time constant is approximate to $Z_A C_D$. This means that Z_A and C_D should be both low. In practice, this is in conflict with the second factor, the impedance matching. As a matter of fact, impedance matching determines how much of the power received by the antenna couples to the diode. The optimal case should be Z_A equal to R_D . The condition for the RC time constant implies that R_D and C_D should be both very low. Therefore, a compromise between the two factors has to be achieved, as it will be explained in details in chapter V.

3.2 – Main rectifiers

In order to ensure a better rectification, an ultra-high speed rectifier has to satisfy several characteristics. The insulator layer should be on the order of a few nanometers, which allows sufficiently large electrical current and ensures the tunneling effect. The $I(V)$ characteristics of the rectifiers should be asymmetric, i.e. different metals should be used on both sides of the insulator layer with great work function difference between them. In order to increase the cut-off frequency and to allow the THz rectification, the area must be very small [93-94]. The junction capacitance defines the diode switching time; as a consequence, a fast diode should have small junction capacitance. The cut-off frequency depends on both the diode capacitance and resistance, as expressed in formula (10)

$$f_c = \frac{1}{2\pi R_D C_D} \quad (10)$$

It can be noted that the resistance R_D mainly depends on the fabrication process. Therefore, the cut-off frequency can be tuned by adjusting the capacitance C_D . However, the presence of the nanoantenna impedance Z_A can modify the overall device response. Consequently, the cut-off frequency can be expressed as

$$f_c = \frac{Z_A + R_D}{2\pi Z_A R_D C_D} \quad (11)$$

In order to achieve a high cut-off frequency, the RC time constant has to be small. Therefore, a small junction area and an appropriate material selection and fabrication are required. The cut-off frequency also changes with the type of rectifier used in the rectenna. This is due to the physical nature of the diode operation. Furthermore, the threshold voltage has to be considered, especially when low power levels have to be harvested. Consequently, in order to obtain a better rectification a low cut-off voltage diode has to be chosen [24, 95].

The main types of ultra-high speed rectifiers used in a rectenna are metal-insulator-metal (MIM) diodes [33, 93, 96], metal-oxide-metal (MOM) diodes [97-99], geometric diodes [33, 100-102], carbon nanotube forests [58, 103]. They will be described in the following subsections.

3.2.1 – MIM diode

The MIM diode is a thin film device consisting of an insulator layer of few nanometers in a thickness placed between two metal electrodes. The metals have a higher work function than the electronic affinity of the insulator. In this way, at the interface between metal and insulator a barrier is produced. The charge transport across the insulator is due to quantum mechanical tunnelling of electrons. A transmission probability is associated with the probability of an electron tunnelling through the classical forbidden region of the insulator bandgap. Figure 37 shows the energy band profile of this diode.

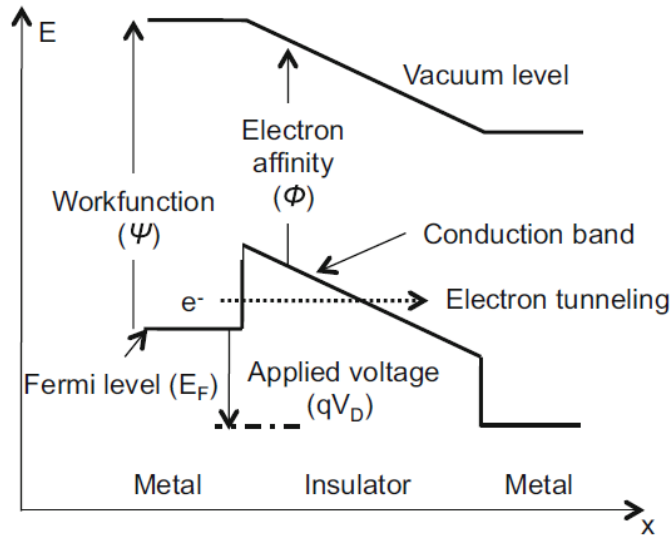


Figure 37: Energy band profile of a single insulator MIM diode [96]

The probability of an electron tunnelling across the insulator depends exponentially on the distance (thickness and height of the barrier) of the bandgap of the insulator. Since this distance changes linearly with the diode voltage, the current is an exponential function of the voltage and depends also on the diode characteristics. To ensure that tunnelling is the dominant conduction mechanism, the thickness of the insulator should not be more than a few nanometers [93, 95-96]. MIM diode has a carrier transit time of the order of femtosecond and can be easily integrated with the nanoantenna. A major drawback of this diode is a relatively large RC time constant; therefore, it can work efficiently at low terahertz frequencies. To make an efficient rectenna, the diode needs to satisfy several characteristics. One is high responsivity, which is the measure of the rectified DC voltage or current as a function of input radiant power. Another characteristic is a low resistance, of the order of the internal nanoantenna impedance, in order to provide good impedance matching between the antenna and the diode. A third property is the asymmetry in the curve $I(V)$. This characteristic is crucial in order to operate the rectenna without applying an external DC bias. A MIM diode can have asymmetric $I(V)$ characteristic if different metals are used on the two sides of the insulator. This gives rise unequal barrier heights. Because of a large asymmetric barrier, a high responsivity can be obtained. However, keeping the diode resistance low requires low barrier heights on both sides and the asymmetry is limited. In order to achieve high responsivity, maintaining high asymmetry and low resistance, a multi-insulator tunnel barrier can be used. The metal multi-insulator metal (MIIM) diodes provides enhanced $I(V)$ non linearity, which allow enhanced responsivity, low resistance and a reduced reverse-bias leakage current. Two mechanisms of operation originate to the enhanced nonlinearity. One is the formation of resonant tunnelling of electrons through a quantum well formed between two insulators. This occurs when the metal Fermi level on the

higher barrier side is biased positive creating a right-triangular well at the interface between the two insulators. The other mechanism occurs for the opposite bias polarity. An abrupt increase in current occurs when the metal Fermi level on the higher barrier side rises above the conduction band of the lower barrier, reducing the tunnel distance. The choice of insulator materials and thicknesses determines the dominant mechanism [33, 93, 95-96]. In order to enhance matching efficiency between nanoantenna and rectifier, a MIM Travelling-Wave diode has been proposed [33, 91, 104-107]. This device consists of MIM plasmonic waveguides. The antenna captures the electromagnetic wave that propagates through a transmission line rectifier and decays totally by the end of the transmission line.

3.2.2 – MOM diode

The MOM diode consists of two metal electrodes that are separated by a thin oxide layer. It operates based on quantum-mechanical tunneling of electrons. As a matter of fact, depending on the work function of the electrodes, electrons tunnel from one electrode to the other with a certain probability. If the metal electrodes are different and have dissimilar work functions, the MOM diode reveals an asymmetric $I(V)$ characteristic. The asymmetry in the structure causes electrons tunnelling effect from the electrode with higher work function to the other creating thus a net tunneling current flow. Due to this asymmetry, the MOM diode exhibits a rectifying behaviour, even without the need of an external bias. Therefore, it is used in the rectenna systems. The tunneling times are of the order of femtoseconds. MOM diode is also characterized by fast response time in mid-infrared measurements and it has a non-linear $I(V)$ characteristic. The greatest shortcoming of using MOM diodes is represented by their low efficiency, which can be even less than 0.1% in the far IR region. Furthermore, the operating frequency is limited due to large RC response time and poor impedance matching to nanoantenna [91, 97-99].

3.2.3 – Geometric diode

The geometric diode is a ballistic ultralow voltage diode with geometrical asymmetry, low capacitance and low resistance to match the antenna impedance [100]. It uses long mean-free path length (MFPL) material with physical asymmetry that determines the preferred direction of the charge movement. This device consists of a patterned conductive thin film whose size is of the order of the MFPL of the charge carriers in the material. Its planar structure allows charge carriers to flow in one direction. The diode is a thin film device designed in order to obtain the asymmetric constriction in the neck region, on the order of the MFPL of the charge carriers or smaller than MFPL. Graphene is chosen because the MFPL of charge carriers is an order of magnitude greater than those in metals at room temperature [108]. The shape of such a geometric graphene diode is an inverse arrowhead so that the charge carriers flow through forward direction, from left to right, as shown in Figure 38.

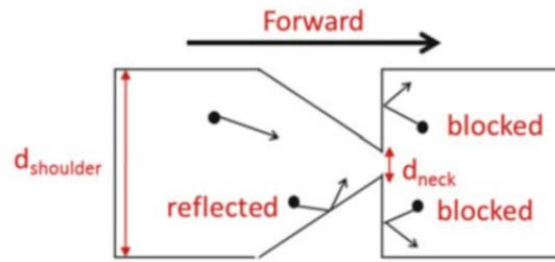


Figure 38: Inverse arrowhead geometric diode structure [101]

The charges moving from right to left are largely blocked by the vertical side wall of the arrowhead. Such a geometric effect causes a $I(V)$ asymmetric characteristic. Increasing charge MFPL and reducing the neck width leads to an increase of the asymmetry of the $I(V)$ characteristic. The choice of the material and the fabrication determine the neck width. Therefore, in order to obtain a large geometric effect, the carrier MFPL in the thin-film material has to be sufficiently large compared to the neck width. Graphene geometric diode provides a low RC time constant, of the order of 10^{-15} s and responds efficiently at petahertz frequencies. The value of the resistance lies in a range from 1 k Ω to 3 k Ω and the capacitance is estimated in a range from 10^{-17} F to 10^{-18} F [33, 100-102, 109-110].

3.2.4 – Carbon nanotube forests

The forest of multiwalled carbon nanotubes consists of nanotubes, which, at high density, are grown on a metal-coated substrate, coated with an insulator and capped with a second metal coating in order to form a diode at the upper contact, as shown in Figure 39.

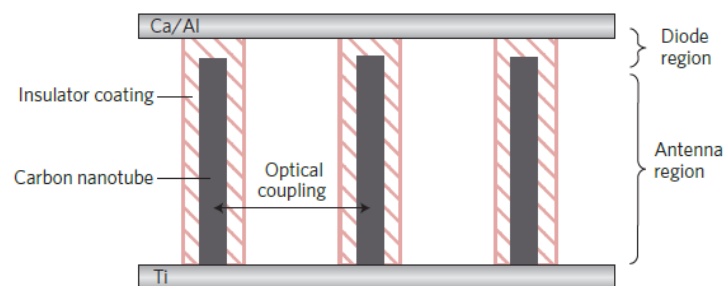


Figure 39: Schematic of carbon nanotube rectenna [58, 103]

The nanotubes act as an antenna, collecting the incident radiation into alternating current that is transferred to the diode. The diode then converts this current into electrical DC power. The area of the tip is very small, with a diameter of about 10 nm. Therefore, the diode capacitance is very low. The diode resistance is instead very high due to the minute diode area. Consequently, there is a relevant

difference between the diode resistance and the antenna resistance and the impedance matching is not satisfied. Nevertheless, the forest of carbon nanotubes works well, because each nanotube is optically coupled to its neighbours and the power rejected from one diode is coupled to neighbours [58, 103].

3.3 – Diode equivalent impedance

The optical radiation incident on rectennas is quantized in the form of photons, the current flowing from the antenna to the diode and the rectification process maintain the quantum nature of energy. As a matter of fact, a quantum description is required for each of these processes in optical rectennas. The photon energy $\hbar\omega$ depends on the diode current-voltage $I(V)$ characteristics [111-112]. Especially, depending on the amplitude of the diode AC voltage V_ω , the rectenna can operate in classical, quantum or transition regime [113-114]. This voltage is a dynamic quantity and changes with the rectenna output voltage V_O . Therefore, in order to determine the operating regime, V_ω is approximated to V_{open} . The rectenna operates in the quantum regime when V_{open} is lower than the photon energy divided by the electronic charge ($\hbar\omega/q$). Electrons can absorb only individual photons. After the photons are absorbed by the antenna, their energy quantization is maintained in form of surface plasmons making up the current flowing to the diode. At the diode, these energy packets can induce transitions of the charge carriers from one side to the other side of the diode. Therefore, to determine the response of the rectenna the photon-assisted tunnelling (PAT) theory can be applied to high-speed diode operation [112]. The voltage across the diode consists of the DC operating voltage V_D and an AC voltage V_ω . Figure 40 shows a typical illuminated $I(V)$ curve. The region of positive current at negative voltage corresponds to power generation.

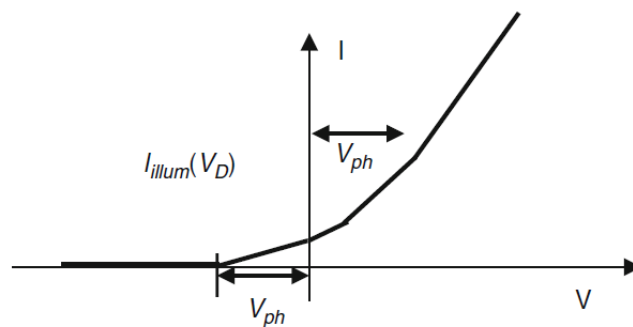


Figure 40: Illuminated $I(V)$ curve. V_{ph} is the photon energy $\hbar\omega/q$ [111]

The AC diode resistance R_D is the reciprocal of the slope of the secant between two points on the $I(V)$ curve R_ω , one photon energy above and below the V_D [111-112, 115-116]

$$R_{\omega} = \frac{2 \left(\frac{h\omega}{q} \right)}{I_{dark} \left(V_D + \frac{h\omega}{q} \right) - I_{dark} \left(V_D - \frac{h\omega}{q} \right)} \quad (12)$$

where I_{dark} is the diode DC dark current. This resistance is twice the DC diode resistance R_{DC} . When V_{open} exceeds $h\omega/q$, electrons absorb multiple photons and the rectenna operates in the transition regime. The electron transitions are described quantum mechanically, but the description of the field can be classical. The rectification process requires a semiclassical description. The $I(V)$ curve is sampled at discrete points corresponding to $\pm h\omega/q$ about the operating voltage, as shown in Figure 41.

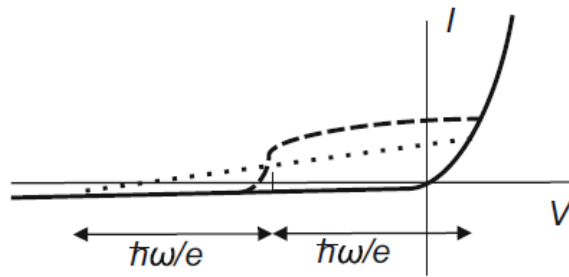


Figure 41: Sketch of a current-voltage $I(V)$ curve for a rectenna diode [33]

As V_{open} is much greater than $h\omega/q$, the rectenna operates in the classical regime and each electron absorbs many photons. The AC diode resistance R_D can be expressed as

$$R_D = \frac{2V_{open}}{\frac{(V_O + V_{open})}{R_f} - \frac{(V_O - V_{open})}{R_r}} \quad (13)$$

where R_f and R_r is the diode forward resistance and the diode reverse resistance respectively and V_o is the operating voltage of rectenna [117]. Electromagnetic radiation from the Sun consists of low intensity but high energy photons. When this type of broadband radiation illuminates the rectenna, it operates in quantum regime. In order to achieve the impedance matching in the rectenna, the diode secant resistance has to be equal to the nanoantenna resistance. An infinite reverse resistance that allows to neglect reverse leakage current, and a forward resistance that matches the antenna and the diode for optimum power transfer usually characterize an ideal diode. The values of forward resistance are in a range of 50-300 Ω for metal-insulator-metal (MIM) diodes and of the order of 3 k Ω for geometric diode. A realistic diode shows a finite reverse resistance of the order of 10^5 - 10^7 Ω [116].

3.4 – Rectenna systems applications

A great variety of rectenna applications have been discussed in the literature. [94] shows an example of a rectenna consisting of an IR dipole nanoantenna coupled to a MIM diode. One end of both dipole's arm has been cut in order to build a MIM diode. The two arms of the dipole are then overlapped over an area of $50 \times 50 \text{ nm}^2$, where an insulator layer of 8.5 nm-thick has been inserted within the gap region. The MIM diode used in this system reveals a diode resistance R_D of about 100Ω and a cut-off frequency of 76.43 THz, so that this configuration is suitable to rectify the $10 \mu\text{m}$ incident infrared wave. An application of the travelling-wave MIM diode is referred in [105]. Two types of travelling wave MIM plasmonic waveguides are considered: vertical coupled strips (VCS) and lateral coupled strips (LCS) transmission lines. These two metallic strips are placed on top of each other or beside each other. Their length is greater than the surface plasmon decay length at the minimum frequency of the band of interest. In this way, the travelling wave is attenuated along the line and there is not reflection at the open-circuit end of the line. Therefore, these transmission lines have the input impedance equal to their characteristic impedances. In order to obtain a dipole nanoantenna that resonates at 30 THz, its length should be optimized. Moreover, the cross-section dimensions of the dipole's arms are fine-tuned to ensure the best matching with the transmission lines. The antenna efficiency for nanodipole terminated by VCS and LCS is respectively 83.61% and 80.15%. The total efficiency, which is the product of antenna harvesting efficiency, matching efficiency and rectifier quantum efficiency, is nine order of magnitude higher for nanodipole terminated by VSC rectifier than that for nanodipole terminated by LSC rectifier [105]. An application of the MOM diode coupled to a bowtie nanoantenna is referred in [98]. It consists of bowtie coplanar slots with MOM diode building between hot and ground metallization of a coplanar waveguide. In this way, the DC power obtained is about 4.6 pW. Another type of rectifier used in the rectenna system is a planar MIM diode formed by two crossed thin film metallic strips made of gold (Au) and copper (Cu) with a very thin copper oxide (CuO) in between them. This diode is integrated with bowtie nanoantennas whose arm is overlapped and the diode is realized in between this overlap. This configuration offers two main advantages: higher field enhancement due to the sharp bowtie tip and a path only available through the rectifier for the highly localized electromagnetic fields [57]. Best performances are obtained employing a sharp tip bowtie nanoantenna with Au/Al₂O₃/Pt MIM diode due to the overlapping antenna arms and the utilization of different electrodes that produces a higher value of tunneling current [118]. It is possible to achieve some improvements increasing the work function difference between the two metal electrodes. So, the I(V) characteristic becomes strongly non-linear and the contact area of the tunnelling junction is reduced; as a consequence, a better impedance matching between antenna and diode is obtained. For this reason, sector bowtie nanoantenna coupled with Au/TiO_x/Ti MIM diode is realized [119]. The choice of sector sharp instead of a traditional triangle is due to the fact that sector configuration can avoid the issue of sharp corners that exist in the traditional

triangle configuration. The Au/TiO_x/Ti MIM diode is chosen because gold and titanium are characterized by a large difference in the work function and so a strong rectifying effect is achieved. By increasing the refractive index of the substrate, the value of power conversion efficiency reached with this type of nano-rectenna is 11.1% [119].

3.5 – Seebeck nanoantennas

Despite nanoantennas coupled to an ultra-high speed rectifier offer high theoretical efficiency, this rectenna system reveals low efficiencies due to the poor performance of the common rectifiers at optical frequencies. So in the last decade new devices based on the use of nanoantennas to confine optical energy and on the exploitation of the thermoelectric properties of their metallic interfaces to recover energy, are under study. This new device consists of a nanoantenna coupled to a metallic thermocouple. The rectification mechanism is based on the Seebeck effect, a thermoelectric voltage generation due to the infrared irradiation induced currents in the antenna [120]. A thermocouple is usually built from two wires of several materials; one end of each wire is connected to a junction (hot junction) while the other ends are unconnected (cold junction). If the temperature of the joined ends increases, an open-circuit voltage occurs across the cold junction of the thermocouple. The value of open-circuit voltage V_{oc} is proportional to the temperature difference between the two junctions and the two Seebeck coefficients of the metals:

$$V_{oc} = (S_a - S_b) \cdot \Delta T \quad (14)$$

This new device reduces the complexity of the fabrication process. Moreover, it is possible to increase the sensitivity of the detectors by varying the material combinations. Figure 42 shows the electric equivalent circuit of the antenna-coupled thermocouples. A high-frequency voltage source, an antenna resistance and a reactance represent the antenna. A current controlled voltage source and an internal resistance represent the thermocouple.

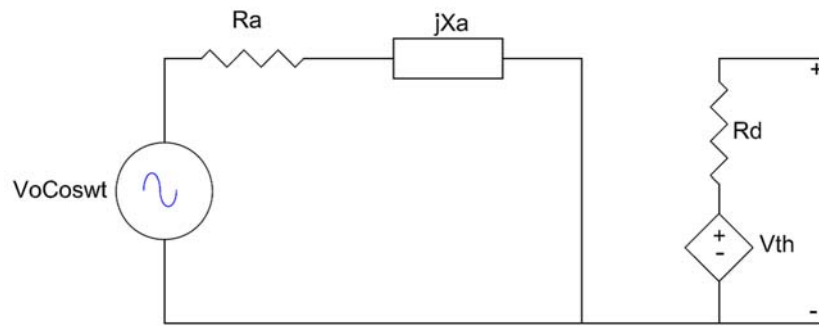


Figure 42: Electric equivalent circuit of the antenna-coupled thermocouples [90]

Similarly to the rectenna, the main types of nanoantennas coupled to thermocouples are the dipole, bowtie antenna and spiral antenna. An antenna-coupled thermocouple in [120] consists of hot junction of a nanowire thermocouple placed at the feed point of a dipole antenna. The hot junction is heated by the dissipation of induced currents due to incident radiation. Different combinations of materials are taken into account for the thermocouple. The best normalized detectivity is obtained with the Palladium-Chromium (Pr-Cr) thermocouple [120-121]. An array of dipole antenna coupled to thermocouples is in [122]. The authors compare this device with the dipole antenna coupled to an MIM rectifier. The conversion efficiency due to thermal effects is better than that due to tunnel effects [122]. Dipole antennas coupled to thermocouples made of the same metal are in [123]. The hot junction of a single metal thermocouple is located close to the center of the dipole. The nanowires of the thermocouples are made of the same metal and with different cross-sections. The time response of this nanostructured thermocouple is a picosecond and so it actually is the fastest THz detector [123]. A bowtie nanoantenna coupled to a thermocouple is in [124]. The thermocouple consists of two wires made respectively of gold and palladium. The hot junction is placed where the wires are joined to each other in the antenna. A transmission line, typically a coplanar strip transmission line, is used to connect the antenna to the thermocouple and to realize an impedance matching between them. The response of this device is obtained varying the length of the transmission line. The best response is recovered using a device with a transmission line of $1.3 \mu\text{m}$ of length. This value is 2.4 fold higher than that of the device without the transmission line. Further improvements can be achieved varying the dimensions of the transmission line, adjusting its characteristic impedance, and as a consequence, by optimizing the impedance match between the antenna and the thermocouple [124]. The Spiral nanoantenna is a convenient system for energy harvesting due to its ideal frequencies-independent electrical impedance. This device can be polarized linearly although better performances are obtained with the right-handed circularly polarized light; the electrical field is concentrated at the center of the nanoantenna [125]. A new device proposed in [125] consists of a metallic thermocouple shaped as a spiral nanoantenna whose size is suitable for the resonance at mid-infrared wavelengths. This device exploits the temperature gradient caused by the

resonant currents in the structure in order to generate a DC voltage V_{OC} thanks to the Seebeck effect at its open ends. Two types of structures have been chosen for the spiral nanoantenna: square spiral and Archimedean spiral. Thin film thermocouples shaped as spiral nanoantenna are built with their arms made of different metals. To optimize the thermal energy harvesting, the chosen power generators have one Ti-Ni interface located at the center of the structures. The percent total efficiencies obtained with these two spiral thermocouples are around 10^{-6} and 10^{-7} [125-126]. An array of metallic thermocouples shaped as spiral nanoantennas are proposed as infrared detectors in [127]. The thermocouple is built employing Archimedean geometry with a left-handed and right-handed spiral connected by the ends and separated from the centers by a distance of $4 \mu\text{m}$. The efficiency values obtained with these types of Seebeck nanoantennas are in a range from $10^{-9}\%$ to $10^{-5}\%$ [127]. Despite several advantages compared to the rectenna systems, Seebeck nanoantennas suffer from heat losses through the substrate, so the efficiencies remain low. It is possible to increase the response of Seebeck nanoantennas reducing the effective thermal conductivity of the substrate. This can be achieved by using freestanding architecture, i. e. by suspending the device on air above its substrate [125].

Conclusion

The rectenna topology has been analysed in this chapter. In particular, the equivalent circuit configuration of a rectenna has been illustrated. It consists of a voltage source V_{open} with an impedance in series Z_A , shaped the nanoantenna, and a parallel between a junction capacitance C_D and a non-linear series resistance R_D , modelled the rectifier. A threshold voltage also characterizes a rectifier. The junction capacitance defines the diode switching time; as a consequence, a fast diode should have small junction capacitance. In order to ensure a better rectification, an ultra-high speed rectifier has to satisfy several characteristics. The insulator layer should be on the order of few nanometers, which allows sufficiently large electrical current and ensures the tunneling effect. The $I(V)$ characteristics of the rectifiers should be asymmetric, i.e. different metals should be used on both sides of the insulator layer each of them should have a work function different each other. In order to increase the cut-off frequency and to allow the THz rectification, the area must be very small. The cut-off frequency also changes with the type of rectifier used in the rectenna. This is due to the physical nature of the diode operation. Furthermore, the threshold voltage has to be considered, especially when low power levels have to be harvested. Consequently, in order to obtain a better rectification a low cut-off voltage diode has to be chosen.

The main types of the rectifiers have been described. The MIM diode is a thin film device consisting of an insulator layer of few nanometers in a thickness placed between two metal electrodes. This diode has a carrier transit time of the order of femtosecond and can be easily integrated with the nanoantenna. It shows a large RC time constant and can work efficiently at low terahertz frequencies. The MOM

diode consists of two metal electrodes that are separated by a thin oxide layer. It is characterized by fast response time in mid-infrared measurements and it has a non-linear $I(V)$ characteristic. The geometric diode consists of a patterned conductive thin film whose size is of the order of the mean-free path length (MFPL) of the charge carriers in the material. It provides a low RC time constant and responds efficiently at petahertz frequencies. The forest of multiwalled carbon nanotubes consists of nanotubes acting as an antenna, coated with an insulator and capped by a metal layer, forming a thin tunnel diode. A low diode capacitance and a high diode resistance characterize this device.

The diode equivalent impedance has been evaluated. Depending on the amplitude of the diode AC voltage V_ω , the rectenna can operate in classical, quantum or transition regime. The rectenna operates in the quantum regime when V_{open} is lower than the photon energy divided by the electronic charge ($\hbar\omega/q$). Electrons can absorb only individual photons. The AC diode resistance R_D is the reciprocal of the slope of the secant between two points on the $I(V)$ curve R_ω , one photon energy above and below the V_D . This resistance is twice the DC diode resistance R_{DC} . When V_{open} exceeds $\hbar\omega/q$, electrons absorb multiple photons and the rectenna operates in the transition regime. As V_{open} is much greater than $\hbar\omega/q$, the rectenna operates in the classical regime and each electron absorbs many photons. The AC diode resistance R_D can be expressed in terms of the diode forward resistance R_f , of the diode reverse resistance R_r and of the operating voltage of rectenna V_0 . Electromagnetic radiation from the Sun consists of low intensity but high energy photons. When this type of broadband radiation illuminates the rectenna, it operates in quantum regime. An infinite reverse resistance that allows to neglect reverse leakage current, and a forward resistance that matches the antenna and the diode for optimum power transfer usually characterize an ideal diode. The values of forward resistance are in a range of 50-300 Ω for metal-insulator-metal (MIM) diodes and of the order of 3 k Ω for geometric diode. A realistic diode shows a finite reverse resistance of the order of 10^5 - 10^7 Ω .

A great variety of rectenna applications, discussed in the literature, has been summarized and compared.

Finally, a new device based on the use of nanoantennas to confine optical energy and on the exploitation of the thermoelectric properties of its metallic interfaces to recover energy, has been described. This new device consists of a nanoantenna coupled to a metallic thermocouple. The rectification mechanism is based on the Seebeck effect, a thermoelectric voltage generation due to the infrared irradiation induced currents in the antenna. A thermocouple is usually built from two wires of several materials; one end of each wire is connected to a junction (hot junction) while the other ends are unconnected (cold junction). If the temperature of the joined ends increases, an open-circuit voltage occurs across the cold junction of the thermocouple. The value of open-circuit voltage V_{OC} is proportional to the temperature difference between the two junctions and the two Seebeck coefficients

of the metals. This new device seems to overcome the limits of low efficiencies due to the poor performance of the common rectifiers at optical frequencies, which characterize the rectennas.

CHAPTER IV – DC-DC BOOST CONVERTERS FOR ENERGY HARVESTING APPLICATIONS

The characteristics of the main commercially DC-DC converters for energy harvesting and ultralow power applications will be discussed in this section. At the beginnings, the constraints of the design of a system based on optical rectennas will be defined. On the basis of these, a commercial DC-DC converter will be chosen. Finally, the characteristics and the mode of operation of the chosen DC-DC converter will be analysed.

4.1 – Main issues of optical rectenna

In order to design a system based on optical rectennas for energy harvesting application, several issues have to be taken into account. The conversion efficiency of a rectenna is limited by two main factors, the RC time constant of the rectifier and the impedance matching between the nanoantenna and the rectifier. The value of the RC time constant has to be of the order of a few femtosecond. This would ensure a good rectification in the range of terahertz. The RC time constant of the rectenna depends on the nanoantenna impedance Z_A , on the diode resistance R_D and on the diode capacitance C_D . When the value of the nanoantenna impedance is much lower than the value of diode resistance, the RC time constant of the rectenna can be expressed only as a function of Z_A and C_D . This means that both Z_A and C_D should to be low. In practice, this is in conflict with the impedance matching condition. As a matter of fact, the impedance matching determines how much of the power received by the antenna couples to the diode. In order to ensure the maximum power transfer between the nanoantenna and the rectifier, Z_A should be equal to R_D . This would imply that R_D and C_D should be both very low, that is in conflict with the condition for the RC time constant. The diode resistance R_D is the characteristic element for each type of diode. The values are typically in a range of 50 Ω -300 Ω for the state of art of MIM diodes and of the order of 1 k Ω - 3 k Ω for the state of art of geometric diode. This means that the impedance matching between the nanoantenna and the rectifier is very difficult to obtain without any expedients. Another issue is tied to the available power on load matching conditions and to the output voltage of the nanoantenna, whose values are respectively on the order of few picowatt and on the order of tens microvolt. Ultralow power applications usually require the values of input voltage that are much higher than that of the nanoantenna output voltage, typically of the order of tens or hundreds of millivolt. For this reason, in order to interface an external load with a rectenna a DC-DC boost conversion system is needed. This system provides the matching with a downstream load, which harvests the output energy from the rectenna. The following subsections will describe the main type of commercially DC-DC boost

power converter for the Ultralow power applications. Furthermore, the characteristics and the operation mode of the DC-DC boost converter chosen for the purpose of this work will be analysed.

4.2 – Harvesting circuits

The DC-DC power converter is typically a system based on the switching elements to obtain an output DC voltage lower or higher than the DC input voltage. This device can be analysed in steady state, which are regulated by means of the turn off and the turn on of the switch, typically a MOSFET. The duty cycle D of the MOSFET defines the value of the output voltage with respect to the input voltage. The basic converter topologies are step-down and step-up. A step-down DC-DC converter, named also Buck converter, produces a lower average output voltage than the DC input voltage. A step-up DC-DC converter, named also boost converter, instead, produces the output voltage greater than the DC input voltage. In energy harvesting applications, a DC-DC power converter has to be able to operate in conditions of extremely low input voltage values, of the order of a few millivolt, and to provide output voltage values on the order of Volt, typical for the supply of the electronic circuits. To this purpose, specific Ultralow Power Devices for energy harvesting application must be considered. These are typically boost converters, charge pump boost converters and resonant converters. Figure 43 shows an equivalent circuit of the step-up DC-DC converter.

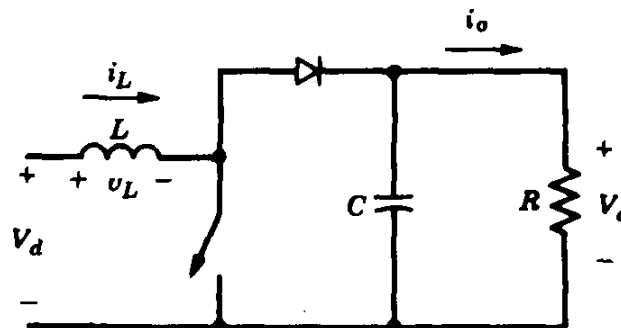


Figure 43: Step-up DC-DC converter [128]

The switch usually is a MOSFET, which turn on and turn off by means of a feedback control maintaining the output voltage constant with respect to the input voltage variations. The switch and the diode operate in complementary mode. In particular, when the switch is on, the diode is reverse biased thus isolating the output stage. The input energy is transferred to the inductor, while the output energy, stored in the capacitor, is transferred to the external load. Instead, when the switch is off, the diode is forward biased and the output stage receives the energy from the inductor and from the input. The interval during the switch is on and the interval during the switch is off depend on the duty cycle of the

switch as well as the ratio between the output voltage and the input voltage, as expressed in formula (15)

$$\frac{V_o}{V_I} = \frac{1}{1-D} \quad (15)$$

In particular, when the duty cycle increases, the output voltage increases too. The control of the average output voltage employs switching at a constant frequency and adjusting of the ON duration of the switch. This method is known as Pulse Width Modulation (PWM) switching. The duty cycle is generated by comparing a signal-level control voltage with a repetitive waveform. The control voltage signal is obtained by amplifying the error, or the difference between the actual output voltage and the desired value. The frequency of the repetitive waveform with a constant peak establishes the switching frequency. The losses in a DC-DC boost converter generally are due to the switching and to the energy dissipation for Joule effect in the parasitic resistances of the inductor and capacitor [128].

Figure 44 shows a charge pump step-up converter.

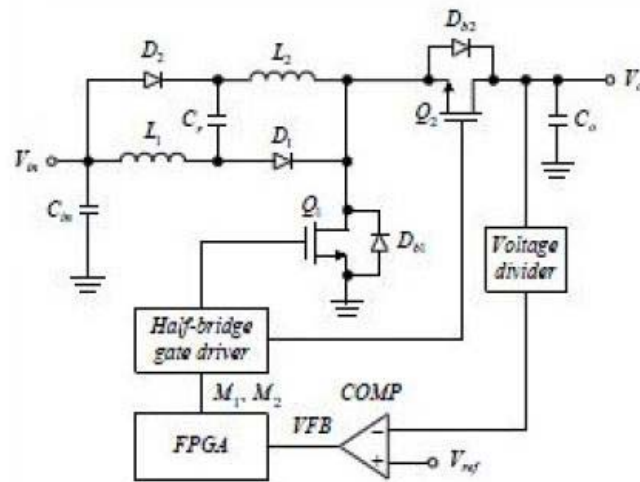


Figure 44: Charge pump step-up converter [129]

This device originates from the classical boost topology and differs from the input stage in which a charge pump, consisting of two diodes, a capacitor and two inductors, is introduced. This type of DC-DC converter operates only in continuous mode and, with the same values of the load current, allows to obtain a better efficiency than the traditional boost converter. Furthermore, it allows to supply higher output voltage values. The charge pump step-up converter is usually employed in commercially boost

converters for ultralow power applications, in particular during the start-up phase. The switch control is performed by means of an output voltage sensing which influences the PWM switching [129].

Figure 45 shows a self-oscillating step-up DC-DC converter.

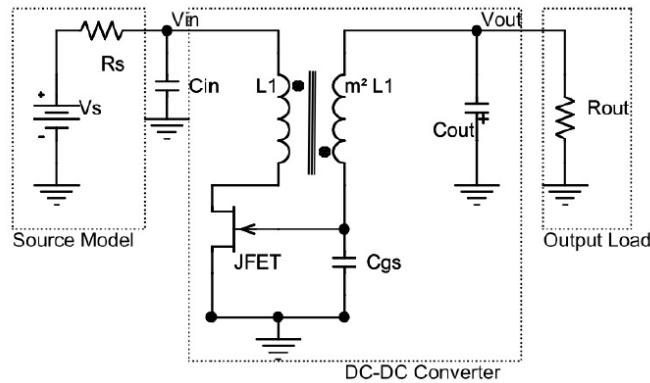


Figure 45: Self-oscillating step-up DC-DC converter [130]

This converter can be coupled with the rectennas since it is able to produce the output voltages on the order of volt with very low input power, on the order of microvolt or millivolt. This converter contains two main blocks: the oscillator, composed by a transformer, a JFET and a capacitor C_{gs} , and the rectifier, whose function is conducted by a p-n junction between gate and source of the JFET and by the capacitor C_{out} . When the current in the primary winding increases, the secondary winding applies a positive voltage on the JFET gate. The gate-source PN junction of the JFET is conducting, and the output capacitor is charged with a negative voltage. The output voltage is therefore negative. When the primary current reaches saturation, the voltage across the primary winding cancels and the negative voltage of the output capacitor is applied on the gate of the JFET pinching it off. The current in the primary winding decreases and a negative voltage is applied by the secondary winding on the gate of the JFET, which leads to its switching off. This peak voltage that switched off the JFET falls back to zero and the oscillation process starts again. The efficiency of this device is between 10 % and 25 %, depending on the value of the input power [130-131].

The boost or buck-boost DC-DC converters for energy harvesting application are usually optimized in order to operate with sources whose values of power are extremely low and provide to an external load output voltage values in the range of 3 V – 5 V. These types of converters are generally employed in stand-alone systems for sensing applications, which require the current for short time pulse intervals. During these time intervals, same dates can be harvested by means of circuits based on microcontroller and can be transmitted by means of transceiver. Several commercial topologies, which can be operated with different sources, i. e. photovoltaic cells or thermoelectric generators, has been found. The

following subsections describe the main features of three type of commercially step-up boost power converters for ultralow power applications that have been taken into account.

4.2.1 – LTC3108

The LTC3108 is an ultralow voltage step-up converter and power manager made by Linear Technology Corporation, CA, USA. This device is a highly integrated DC-DC converter for harvesting and managing surplus energy from extremely low input voltage sources such as thermoelectric generators, thermopiles and small solar cells. The LTC3108 is typically used in low power wireless sensors applications; it is designed to manage the charging and regulation of multiples outputs and to charge a standard capacitor, supercapacitor or rechargeable battery, using energy harvested from a Peltier or photovoltaic cells. Figure 46 shows the equivalent circuit of a typical application of LTC3108.

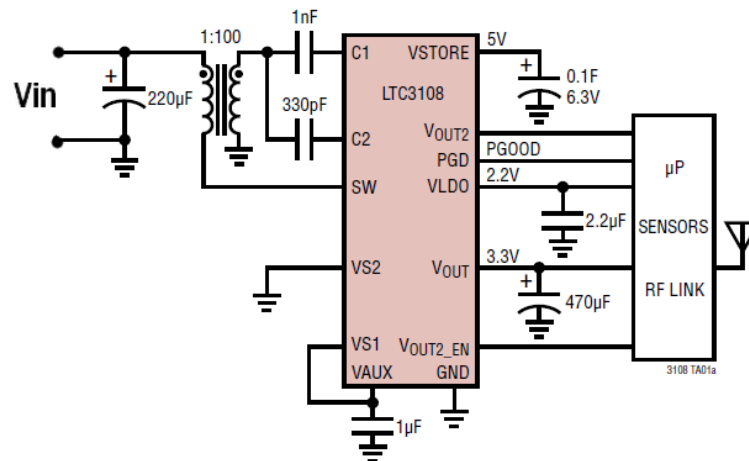


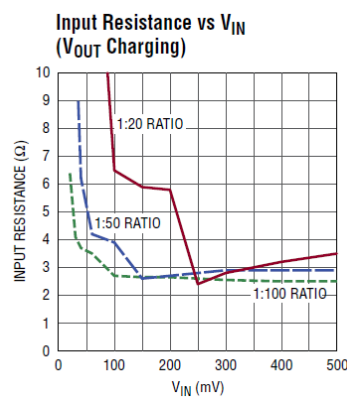
Figure 46: Equivalent Circuit of a typical application LTC3108 [132]

The mode of operation is based on the self-oscillating stage that contains the secondary winding of the transformer, the gate-source junction of the integrated MOSFET and the external capacitor C_2 . The 1 nF-capacitor, that connects the secondary winding of the transformer to the capacitor C_1 , operates as an external charge pump for the rectifying stage. The V_{AUX} pin is the rectifier output and it is the most important voltage reference for the activation of the other outputs. Moreover, it supplies the active circuits within the LTC3108. The V_{S1} and V_{S2} pins allow to select the principal output voltage value V_{OUT} by means of the connection of them to the ground or to V_{AUX} . Table 5 shows the typical regulated values of V_{OUT} using V_{S1} and V_{S2} .

Table 5: Regulated voltage using pins V_{S1} and V_{S2} [132]

V_{S1}	V_{S2}	V_{OUT}
GND	GND	2.35 V
GND	V_{AUX}	3.3 V
V_{AUX}	GND	4.1 V
V_{AUX}	V_{AUX}	5 V

The second voltage output is V_{OUT2} , which can be turned on and off by means of the enabling of the V_{OUT2_EN} . This output can be used to supply external circuits, such as sensors and amplifiers that do not have low power sleep or shutdown capability. The V_{STORE} output can be used to charge a large storage capacitor or rechargeable battery after V_{OUT} has reached regulation. The V_{LDO} pin is a Low Dropout Output of 2.2 V for powering low power microprocessors or other low power integrated circuits. This output is current limited to 4 mA. A power good comparator monitors the output voltage V_{OUT} . The P_{GD} pin have the task of indicate when the converter can be operated in regime mode. The step-up topology operates from input voltages as low as 20mV. The maximum value of input voltage is 500 mV. The step-up transformer turns ratio determines the lower value of the input voltage for the start-up of the converter. Using a 1:100 ratio, the minimum values that can be accepted is 20 mV. A MOSFET switch is utilized to form a resonant step-up oscillator using an external step-up transformer and a small coupling capacitor. This allows the minimum input voltage of 20 mV to be raised. The frequency of oscillation depends by the inductance of the transformer secondary winding and is typically in the range of 10 kHz to 100 kHz. The value of the LTC3108 input impedance depends on the value of the input voltage V_{IN} and on the value of the input current I_{IN} . The average value of this current depends on the frequency of the oscillator and as a consequence on the MOSFET switching frequency. The typical value of Z_{IN} is on the order of few ohm, as it can be noted in the Figure 47.


Figure 47: Input resistance versus V_{IN} [132]

During the charge of V_{OUT} , the P_{GD} signal is low and the values of the input resistance are much higher than those that are measured in regime mode of operation. Figures 48 a) and 48 b) show the start-up voltage sequencing and the P_{GD} response versus V_{OUT} during a step load [132].

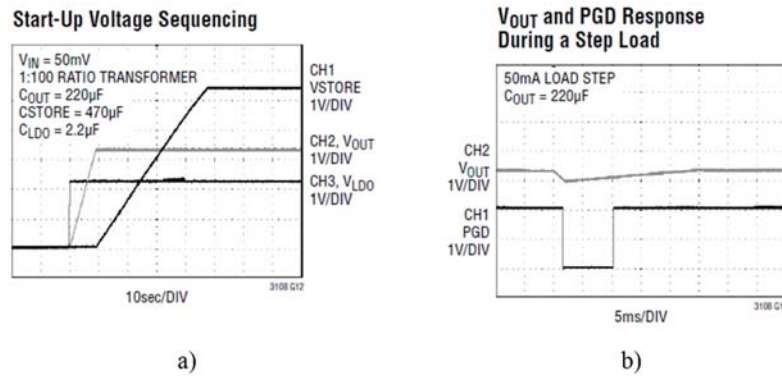


Figure 48: a) Start-up voltage sequencing in LTC3108; b) PGD response versus V_{OUT} during a step load in LTC3108 [132]

4.2.2 – LTC3105

The LTC3105 is a high efficiency step-up DC-DC converter made by Linear Technology Corporation, CA, USA. This device is usually employed for low voltage, high impedance alternative power sources such as photovoltaic cells, thermoelectric generators and fuel cells. An integrated maximum power point controller (MPPC) maximizes the energy that can be extracted from any power source. A Burst Mode operation allows to optimize the converter efficiency and the output voltage ripple over all operating conditions. Figure 49 shows the equivalent circuit of a typical application of LTC3105.

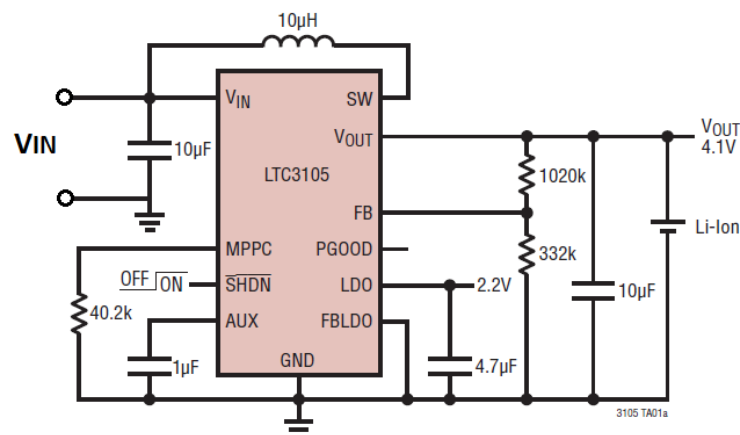


Figure 49: Equivalent Circuit of a typical application LTC3105 [133]

This device is characterized by a main output voltage V_{OUT} and by an output V_{AUX} that supplies external microprocessors and sensors while the main output is charging. The V_{LDO} pin is a Low Dropout Output of 2.2 V for powering low power microprocessors or other low power integrated circuits. The power good output P_{GD} is used to indicate that V_{OUT} is in regulation. The start-up mode operation requires the initial charge of the V_{AUX} . When V_{AUX} has reached the value of 1.4 V, V_{LDO} begins increasing and the converter leaves the start-up mode and enters in normal mode operation. The converter continues charging V_{AUX} until V_{LDO} enters in regulation. When V_{LDO} is in regulation, the converter begins charging V_{OUT} until it is equal to V_{AUX} . V_{AUX} is maintained at a level sufficient to ensure that the LDO remains in regulation. If V_{AUX} becomes higher, charge is transferred to V_{OUT} . The minimum start-up voltage is 250 mV, and the range of input voltages are from 225 mV to 5 V. Figure 50 shows the typical converter start-up sequence.

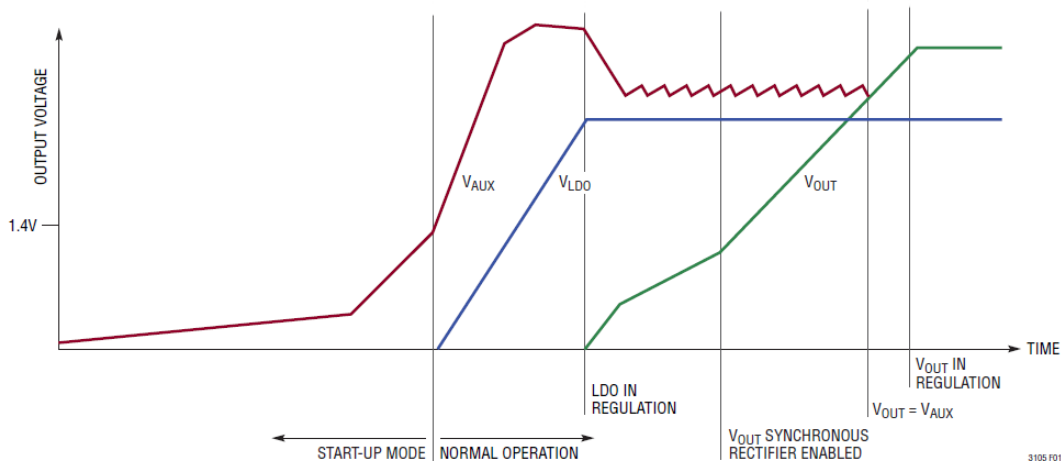


Figure 50: Typical LTC3108 start-up sequence [133]

Both V_{OUT} and V_{LDO} are regulated by an external feedback input. The Maximum Power Point Control (MPPC) circuit allows to set the optimal input voltage operating point for a given power source. The Burst Mode optimizes the output voltage ripple and the peak current, increasing thus the converter efficiency. The Soft Start-up Mode prevents the peak currents during the start-up mode. The Shutdown Mode disables the switching of the device and provides a quiescent current equal to 10 μ A. Moreover, an integrated thermal shutdown offers protection from over temperature faults. The LTC3105 is optimized for low power application employing high internal resistance power sources like photovoltaic cells and thermoelectric generators. This device does not provide the regulation of the minim input voltage during the star-up mode by means of the turns ratio of an external transformer. This is because only a power inductor of about 10 μ H connects the input to the internal switch [133].

4.2.3 – SPV1050

The SPV1050 is an ultralow power and high-efficiency energy harvester and battery charger made by STMicroelectronics™ (USA). This device is suitable for both photovoltaic cells and thermoelectric generators harvesting sources and it allows to charge any type of battery, including the thin film batteries. Moreover, the SPV1050 implements the MPPT function and integrates the switching elements for boost or buck-boost converter. The MPPT is programmable by a resistor input driver and allows to maximize the source power under any temperature and irradiation condition. An unregulated voltage output is available and two independent LDO pins are embedded for powering sensors and RF transceivers. Figure 51 shows a typical block diagram of SPV1050.

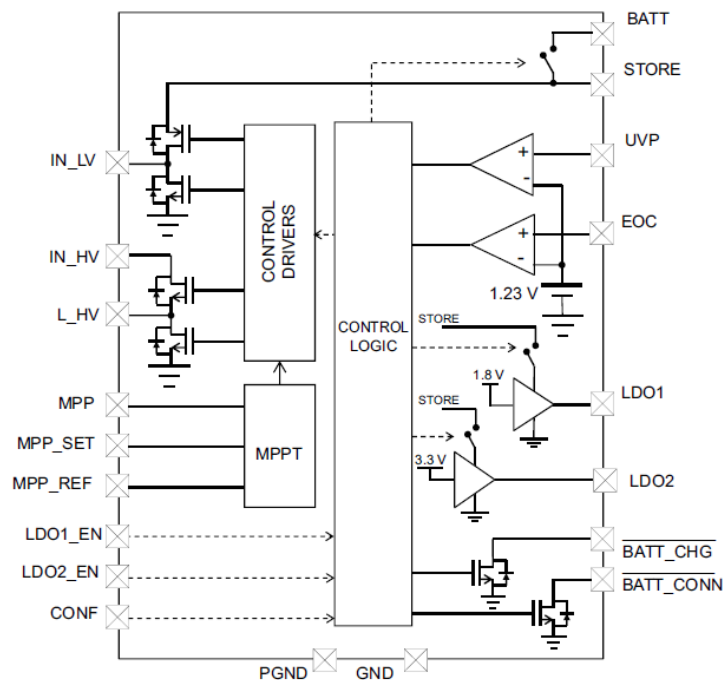


Figure 51: SPV1050 block diagram [134]

The main output is BATT pin, while STORE pin is an output for an auxiliary tank capacitor. An Under Voltage Protection (UVP) and an End-Of-Charge (EOC) functions are implemented. The BATT_CHG and BATT_CONN pins provide some information on the state of charge and the connection of any battery. Several pins are dedicated to the MPPT function. MPP-SET and MPP-RESET allow to enable and to disable respectively MPPC system and choosing an external voltage reference. The IN_HV, IN_LV, L_HV pins are input voltage source that have to be set differently for boost and buck-boost configurations. In the case of boost configuration, shown in Figure 52, the start-up mode requires the use of an integrated high-efficiency charge pump until V_{STORE} remains lower than V_{IN} . The

DC-DC converter stage and the MPPT remain OFF. Once V_{STORE} is equal to V_{IN} , the DC-DC converter stage begins boosting the voltage and the MPPT mode becomes active.

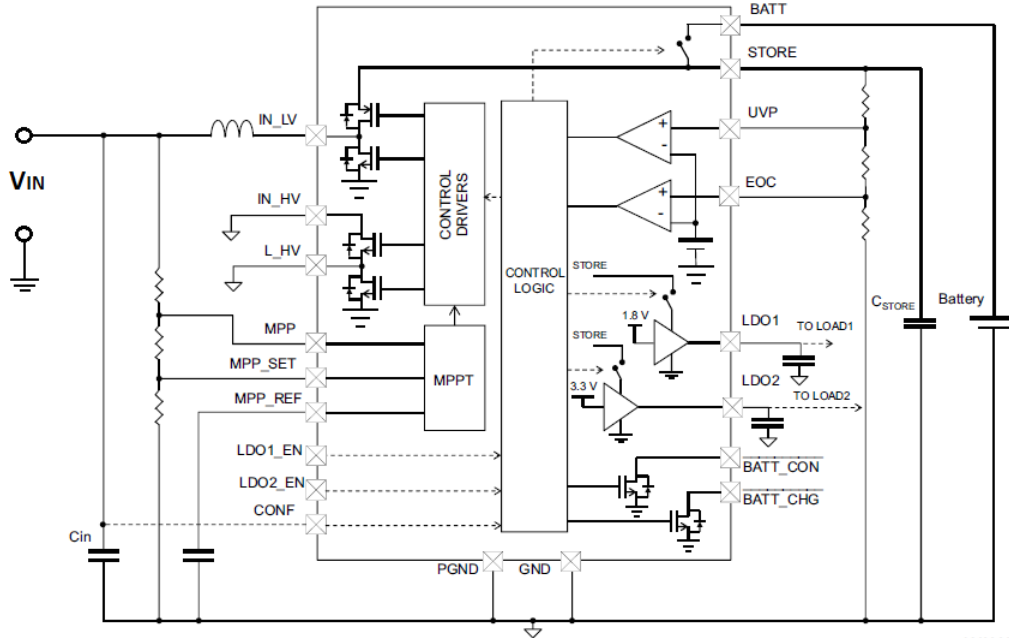


Figure 52: SPV1050 Boost configuration [134]

Figure 53 shows the behaviour of V_{IN} and V_{STORE} at the start-up.

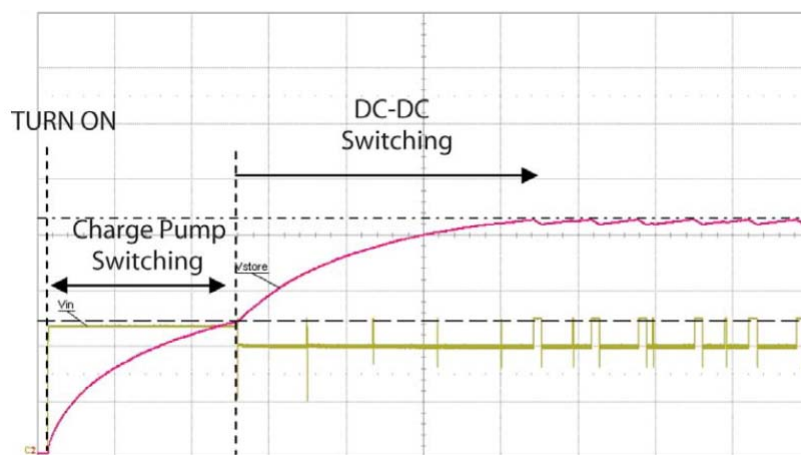


Figure 53: SPV1050 start-up behavior [134]

The integrated MPPT algorithm sets the converter internal impedance in order to maximize the power, as shown in Figure 54. In particular every 16 s, $T_{TRACKING}$ interval, the DC-DC converter stage is disabled for a T_{SAMPLE} equal to 400 ms. During T_{SAMPLE} , the input open circuit voltage V_{OC} is sampled.

Once the T_{SAMPLE} is elapsed, the MPPT algorithm provides a new value of V_{MPP} and the input impedance is regulated so that V_{IN} stay as close as possible to V_{MPP} of the source.

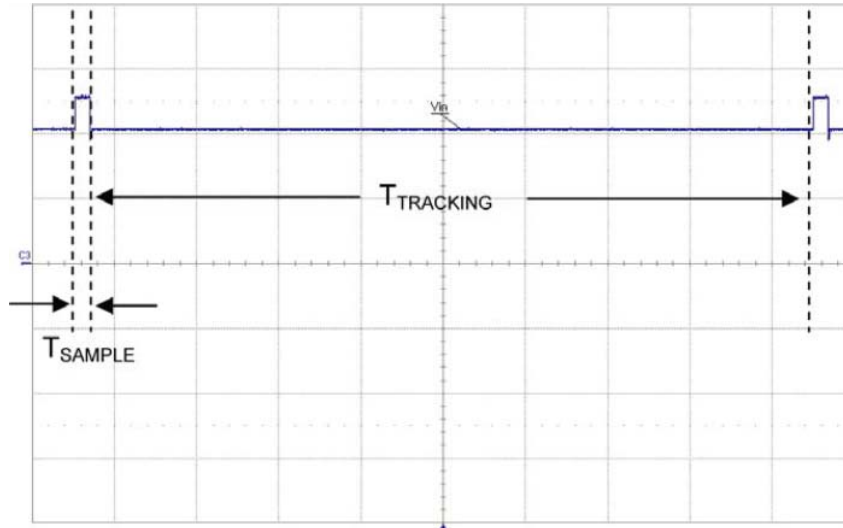


Figure 54: SPV1050 MPPT tracking [134]

The typical minimum input voltage is 150 mV. However, a first start-up in boost configuration requires an input voltage as low as 550 mV [134].

4.3 – Choice of LTC3108

A comparison between the three types of commercial DC-DC converters described in the previous subsections is illustrated in Table 6.

Table 6: Comparison between LTC3108, LTC3105 and SPV1050

<i>DC-DC Converter</i>	<i>Minimum V_{IN}</i>	<i>Maximum V_{IN}</i>	<i>MPPC/MPPT</i>
LTC3108	20 mV	500 mV	No
LTC3105	250mV (start-up mode) 225 mV (regime mode)	5 V	Yes
SPV1050	500 mV (start-up mode) 150 mV (regime mode)	5.3 V	Yes

It can be noted that the LTC3108 DC-DC boost converter reveals the lower value of the minimum input voltage, as low as 20 mV. However, it does not implements the MPPC/MPPT algorithm. Otherwise, the other typologies of DC-DC converter are characterized by a higher start-up voltage and implement the MPPC/MPPT function. Since the most important issues for the design of an energy harvesting system based on optical nano-rectennas are the low output voltage, on the order of tens microvolt, and the low available power on the load matching conditions, on the order of few picowatt,

the LTC3105 and the SPV1050 are not suitable. Therefore, the DC-DC boost converter chosen for the purpose of this work is the LTC3108. The absence of a maximum power point tracking system involves that the input impedance of the converter would not be controlled immediately as the rectenna supplied voltage changes. Therefore, the use of an external control is required in order to regulate the input converter impedance. This circuit will be analysed in details in the chapter VI. The following subsections instead will explain the evaluation board, the mode of operation and the input impedance evaluation of the LTC3108.

4.3.1 – Evaluation board

The Demonstration Circuit 1582B featuring the LTC3108 is a highly integrated DC-DC converter optimized for harvesting and managing energy from extremely low input voltage sources such as thermoelectric generators. Figure 55 shows the connection diagram of the Demonstration circuit 1582B.

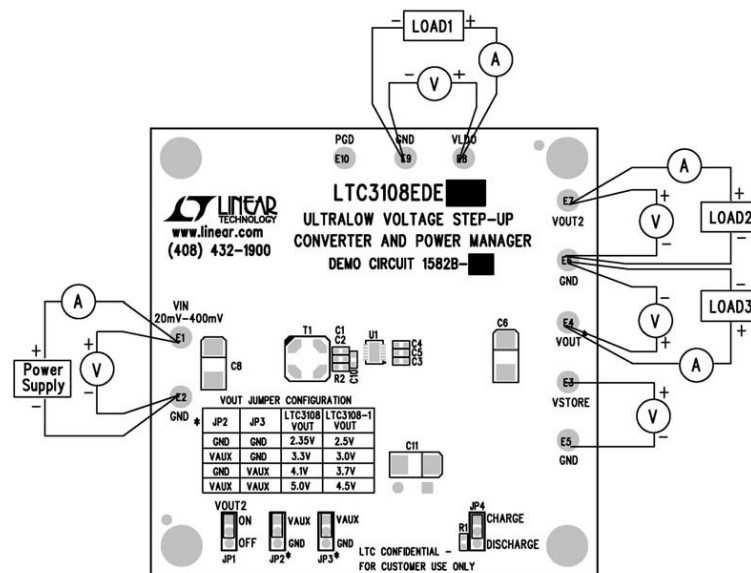


Figure 55: LTC3108 Demonstration Circuit 1582B [135]

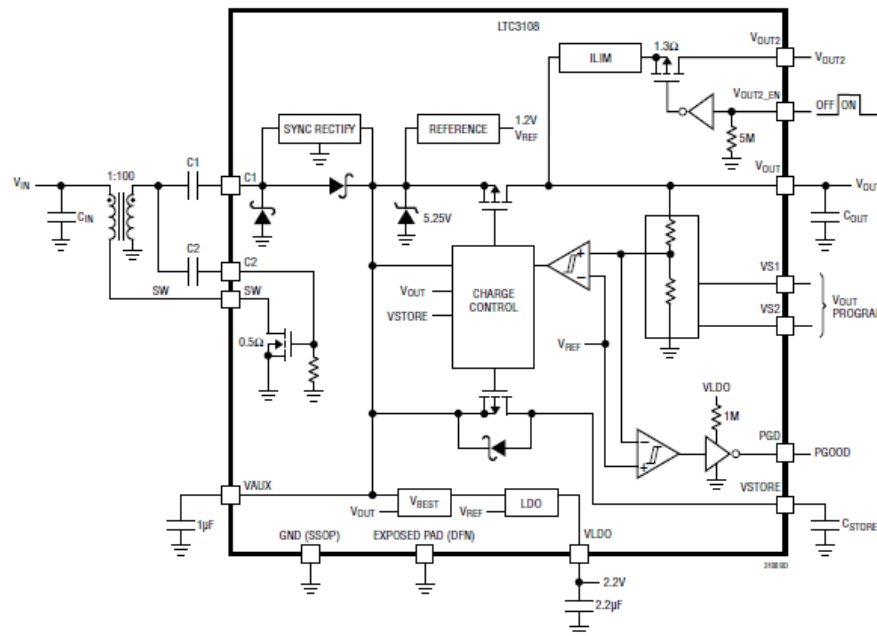
This Demonstration Circuit implements a transformer LPR6235 made by Coilcraft (USA). It has been optimized for low start-up voltage with a 100:1 turns ratio transformer. Therefore, the minimum input voltage for the start-up is 20 mV. The self-oscillating stage, consisting of the secondary winding of the transformer and the capacitor C_2 , works at a frequency range from 10 kHz to 100 kHz. Considering the Demonstration Circuit, the value of this frequency is about 44 kHz. The circuit includes three external jumpers, which allow to connect V_{S1} and V_{S2} pins to the output voltage pins V_{AUX} and G_{ND} . In this way it is possible setting the values of the output voltages V_{OUT1} and V_{OUT2} . Table 7 shows the electrical characteristics of the Demonstration Circuit 1582B [135].

Table 7: Electrical characteristics of the Demonstration Circuit 1582B [135]

Input Voltage Range	50 mV – 400 mV (typical no load start-up = 20 mV)
V_{LDO}	2.2 V
V_{OUT}	Jumper selectable from 2.35 V to 5.0 V
V_{OUT2}	Switching output, $V_{OUT2}=V_{OUT}$
V_{STORE}	5.25 V

4.3.2 – Mode of operation

The block diagram of the LTC3108 boost converter is sketched in Figure 56.


Figure 56: LTC3108 block diagram [132]

A specific output voltages sequencing characterize the start-up mode. The self-oscillating stage supplies an alternating current to the transformer secondary winding that is boosted and rectified using an external charge pump capacitor C_1 and the rectifiers internal to the LTC3108. The rectifier circuit feeds current into V_{AUX} , providing charge to an external V_{AUX} capacitor and the other outputs. When V_{AUX} reaches the value of 2.0 V, synchronous rectifiers provide to the rectification of the input voltage, improving thus the converter efficiency. A voltage reference is then activated. Once V_{AUX} exceeds the value of 2.2 V, the V_{LDO} becomes active. When V_{AUX} reaches the value of 2.3 V, the V_{OUT} is charging and for its value within 7.5 % of its regulated voltage, P_{GD} becomes active. This value indicates the complete regulation of the main output voltage V_{OUT} . Once V_{OUT} has reached regulation, the V_{STORE}

output begins increasing until it reaches its standard value. Figure 57 shows the output voltage sequencing.

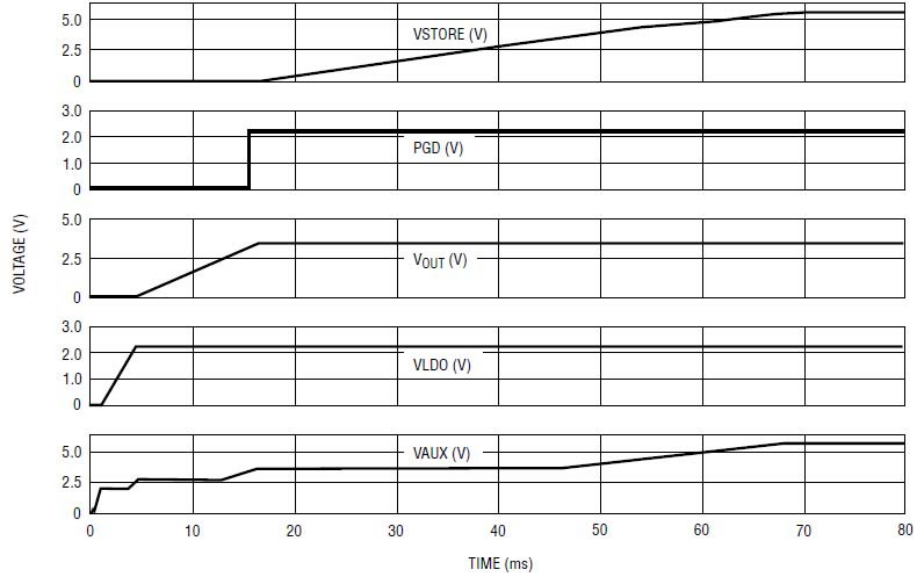


Figure 57: Output voltage sequencing [132]

Therefore, the value of the LTC3108 input impedance depends on the value of V_{IN} and on the value of the input current I_{IN} . The average value of this current depends on the frequency of the oscillator and as a consequence on the MOSFET switching frequency. For this reason, the external control circuit, which will be described in details in chapter VI, has to be able to change the MOSFET switching frequency.

4.3.3 – Input LTC3108 impedance evaluation

In order to obtain a maximum power transfer from the energy harvesting system to an external load, an impedance matching between the rectenna and the DC-DC converter is required. To this purpose, the knowledge of the LTC3108 input impedance R_{IN} is required. To estimate this input impedance the voltage and the current at the input of DC-DC converter have been measured. These were taken employing a DMM4050 Digital Multimeter (Tektronix, OR, USA), a E3615A Power Supply (Hewlett-Packard, CA, USA), a MSO6104A Oscilloscope (Agilent Technologies, CA, USA), a 1582B Demo Circuit (Linear Technology Corporation, CA, USA). The experimental rig is shown in Figure 58.

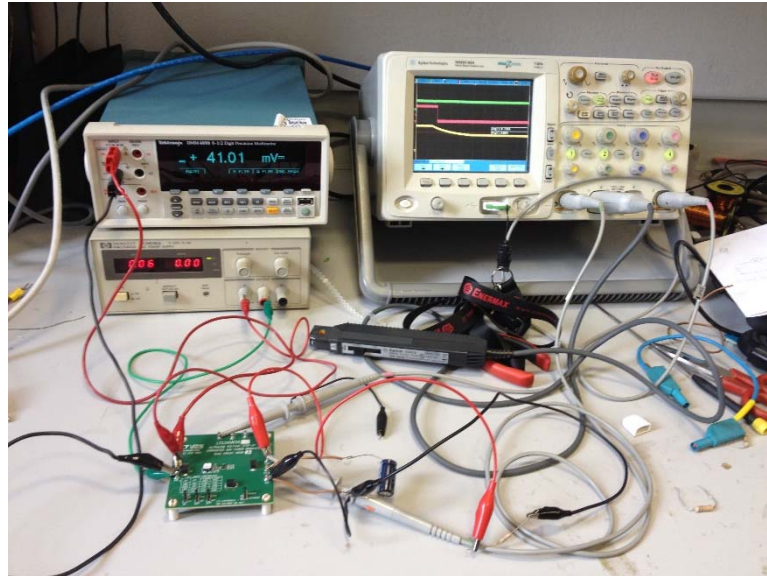


Figure 58: The experimental rig

Figure 59 shows the sketch of the connections in the rig.

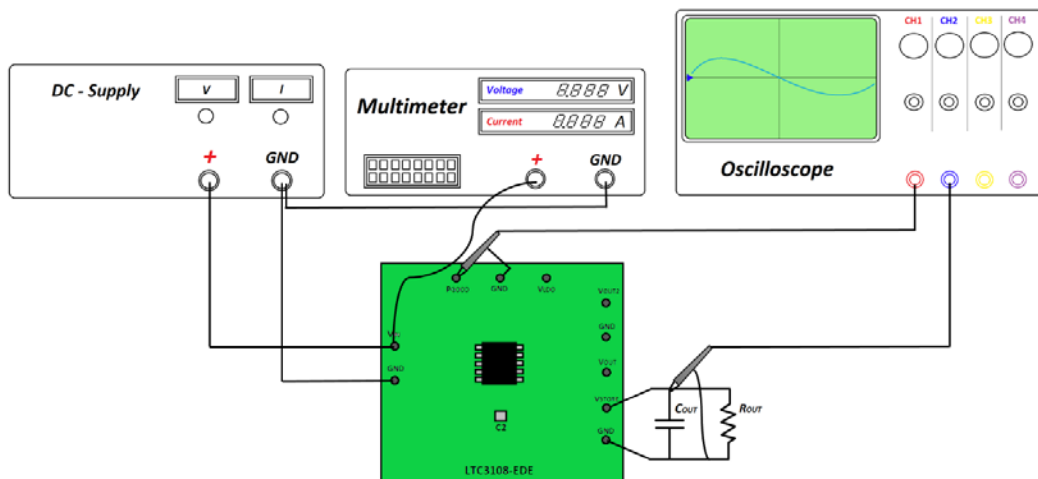


Figure 59: Connections in the rig

The output voltage reference is indicated as V_{STORE} (see Figure 56). At the beginnings, a voltage in a range of 40 mV – 400 mV is supplied at the input of LTC3108 by charging at first a 220 μ F internal capacitor C_{STORE} between V_{STORE} and ground and then a 1000 μ F external capacitor C_{OUT} between V_{STORE} and ground. The input current has been measured. Then, the LTC3108 has been discharged by connecting a 100 k Ω resistor R_{OUT} at its end. The current has been calculated. Figure 60 shows the input current during the charging phase of the output capacitor. This current is required from the circuit until the voltage at P_{GD} terminal remains low. During this interval, it is possible to evaluate the input impedance. The trends of V_{STORE} e P_{GD} during a charge cycle also are shown in Figure 60.



Figure 60: Time domain waveforms of input current I_{IN} (top), P_{GD} voltage (middle) and output voltage V_{STORE} (bottom)

Table 8 shows the input impedance measures at $C_{OUT} = C_{STORE} = 220 \mu F$ and $R_{OUT} = 100 k\Omega$.

Table 8: R_{IN} values at $C_{OUT} = 220 \mu F$ and $R_{OUT} = 100 k\Omega$

$C_{TOT} [\mu F]$	$R_{OUT} [k\Omega]$	$V_{IN} [mV]$	$I_{IN} [mA]$	P_{GD}	$R_{IN} [\Omega]$
220	100	41.17	10.88	Low	3.78
220	100	41.19	12.46	High	3.30
220	100	90.66	33.06	Low	2.74
220	100	90.66	37.67	High	2.41
220	100	200.00	72.24	Low	2.77
220	100	200.00	78.42	High	2.55
220	100	300.00	113.40	Low	2.64
220	100	300.00	120.00	High	2.50
220	100	376.00	145.10	Low	2.59
220	100	376.00	151.00	High	2.49

Table 9 shows the values of the LTC3108 input impedance measured at $C_{TOT} = C_{OUT} + C_{STORE} = 1220 \mu F$ and $R_{OUT} = 100 k\Omega$.

Table 9: R_{IN} values at $C_{TOT} = 1220 \mu F$ and $R_{OUT} = 100 k\Omega$

$C_{TOT} [\mu F]$	$R_{OUT} [k\Omega]$	$V_{IN} [mV]$	$I_{IN} [mA]$	P_{GD}	$R_{IN} [\Omega]$
1220	100	41.10	10.84	Low	3.80
1220	100	41.10	12.40	High	3.31
1220	100	90.33	33.25	Low	2.71
1220	100	90.33	37.70	High	2.39
1220	100	200.00	72.94	Low	2.74
1220	100	200.00	78.87	High	2.53
1220	100	304.00	115.20	Low	2.64
1220	100	304.00	121.60	High	2.50
1220	100	376.00	144.92	Low	2.59
1220	100	376.00	151.36	High	2.49

It can be noted that the input current of the LTC3108 is not influenced by the value of the load resistor R_{OUT} . The values of R_{IN} keep almost constant when the input voltage remains the same in both the two measures. During the start-up phase, P_{GD} is still “Low”, the current is lower than its value in regime mode and the value of R_{IN} is higher, on the order of $3.8 \Omega - 2.5 \Omega$. In correspondence of higher values of input voltages, the values of the input current during the start-up and regime mode are almost similar. As a consequence, the values of R_{IN} are comparable. This because V_{STORE} is the output current driven. This allows also to explain because the values of R_{IN} measuring at C_{TOT} equal to $220 \mu F$ and $1220 \mu F$ are the same. Other measures have been carried out at the value of R_{OUT} equal to $10 k\Omega$ and low values of input voltages. At these conditions, P_{GD} has remained “Low”, highlighting how the value of the load resistor R_{OUT} influences the discharge of the LTC3108. As a matter of fact, during the start-up the output voltage sequencing provides that V_{STORE} begins to increase once the V_{OUT} reaches its rated value. The load resistor R_{OUT} in parallel with the output implicates a charge and discharge of the storage capacitor. As a consequence, the value of the discharge time constant $R_{OUT}C_{TOT}$ could be much higher than the value of the charge time constant; therefore, the LTC3108 converter would not reach the regime mode. As the value of R_{OUT} changes to $100 k\Omega$, P_{GD} is “High” and all the output reach their regulation. The storage capacitor has an influence on the LTC3108 charge time and, as a consequence, on the start-up time. The measures carried out at the two different values of C_{TOT} have confirmed these results. Especially, the start-up time during the measures at C_{TOT} equal to $220 \mu F$ is much lower than its value during the measures at C_{TOT} equal to $1220 \mu F$. In order to design the storage capacitor the knowledge of the load impedance Z_{LOAD} and, in correspondence of pulse mode operation, the maximum operation time interval during which C_{STORE} has to supply a constant current are needed.

Conclusion

The main issues of the design of a system based on optical rectennas for energy harvesting application have been taken into account. The RC time constant of the rectifier and the impedance matching between the nanoantenna and the rectifier are two main factors that can limit the conversion efficiency of a rectenna. The value of the RC time constant has to be on the order of a few femtosecond. This would ensure a good rectification in the range of terahertz. Impedance matching between the antenna and the rectifier determines how much of the power received by the antenna couples to the diode. In order to ensure the maximum power transfer between the nanoantenna and the rectifier, Z_A should be equal to R_D . The diode resistance R_D is a characteristic element for each type of diode. The values are typically in a range of 50 Ω - 300 Ω for the state of art of MIM diodes and of the order of 1 k Ω - 3 k Ω for the state of art of geometric diode. This means that the impedance matching between the nanoantenna and the rectifier is very difficult to obtain without any expedients. Another issue is tied to the available power on the load matching conditions and to the output voltage of the nanoantenna, whose values are respectively on the order of few picowatt and on the order of tens microvolt. Ultralow power applications usually require the values of input voltage that are much higher than that of the nanoantenna output voltage, typically on the order of tens or hundreds of millivolt. For this reason, in order to interface an external load with a rectenna a DC-DC boost conversion system is needed. This system provides the matching with a downstream load, which harvests the output energy from the rectenna.

The main features of three types of commercially step-up boost power converters for ultralow power applications have been taken into account. The LTC3108 is an ultralow voltage step-up converter and power manager made by Linear Technology Corporation, CA, USA. This device is a highly integrated DC-DC converter for harvesting and managing surplus energy from extremely low input voltage sources such as thermoelectric generators, thermopiles and small solar cells. The mode of operation is based on the self-oscillating stage that contains the secondary winding of the transformer, the gate-source junction of integrated MOSFET and the external capacitor C_2 . The step-up topology operates from input voltages as low as 20mV. The maximum value of input voltage is 500 mV. The LTC3105 is a high efficiency step-up DC-DC converter made by Linear Technology Corporation, CA, USA. This device is usually employed for low voltage, high impedance alternative power sources such as photovoltaic cells, thermoelectric generators and fuel cells. An integrated maximum power point controller (MPPT) maximizes the energy that can be extracted from any power source. The minimum start-up voltage is 250 mV, and the range of input voltages are from 225 mV to 5 V. The SPV1050 is an ultralow power and high-efficiency energy harvester and battery charger made by STMicroelectronics™, USA. This device is suitable for both photovoltaic cells and thermoelectric generators harvesting sources and it allows to charge any type of battery, including the thin film batteries. Moreover, the SPV1050 implements the MPPT function and integrates the switching elements for boost or buck-boost converter.

The typical minimum input voltage is 150 mV. However, a first start-up in boost configuration requires an input voltage as low as 550 mV. A comparison between the three types of commercial DC-DC converters have been made. Since the most important issues for the design of an energy harvesting system based on optical nano-rectennas are the low output voltage, on the order of tens microvolt, and the low available power on the load matching conditions, on the order of few picowatt, the LTC3105 and the SPV1050 are not suitable. Therefore, the DC-DC boost converter chosen for the purpose of this work has been the LTC3108. The absence of a maximum power point tracking system involves that the input impedance of the converter would not be controlled immediately as the rectenna supplied voltage changes. Therefore, the use of an external control is required in order to regulate the input converter impedance. The Demonstration Circuit and the operation mode of LTC3108 have been detailed. Finally, the evaluation of the LTC3108 input impedance has been described. The values of this impedance are in a range of $2.5 \Omega - 3.8 \Omega$.

CHAPTER V – DESIGN OF RECTENNA ARRAY

The main guidelines for the design of an array of optical rectennas will be defined in this section. In particular, the optimal impedance matching between the array and the load will be investigated in order to allow the maximum power transfer. The available power and energy during a typical day in Palermo (South of Italy, 38.1157° N, 13.3613° E) at the terminals of the array of optical rectennas under matching conditions will be evaluated. Finally, a comparison between photovoltaic cells and rectenna in order to highlight the main differences will be performed.

5.1 – Impedance matching

In order to supply an external load a rectenna system is necessary. The equivalent circuit of a rectenna consists of the nanoantenna circuit in parallel with the rectifier. The nanoantenna is shaped as a voltage source V_{open} with an impedance in series Z_A . A junction capacitance C_D and a non-linear series resistance R_D usually model the rectifier.

To calculate the impedance matching, the diode junction capacitance C_D can be neglected because it behaves as a low pass filter. The current flowing in the circuit can be expressed as:

$$I = \frac{V_{open}}{R_A + \frac{R_D R_L}{R_D + R_L}} = V_{open} \cdot \frac{R_D + R_L}{R_A(R_D + R_L) + R_D R_L} \quad (16)$$

The total power in the circuit can be expressed as:

$$P_{TOT} = V_{open}^2 \cdot \left[\frac{R_D + R_L}{R_A(R_D + R_L) + R_D R_L} \right]^2 \quad (17)$$

The power in the antenna, in the diode and in the load are shown below:

$$P_A = V_{open}^2 \cdot \left[\frac{R_A + R_L}{R_A(R_D + R_L) + R_D R_L} \right]^2 \cdot R_A \quad (18)$$

$$P_D = V_{open}^2 \cdot \left[\frac{R_L}{R_A(R_D + R_L) + R_D R_L} \right]^2 \cdot R_D \quad (19)$$

$$P_L = V_{open}^2 \cdot \left[\frac{R_D}{R_A(R_D + R_L) + R_D R_L} \right]^2 \cdot R_L \quad (20)$$

Figure 61 shows the curve of P_L versus R_A and R_L .

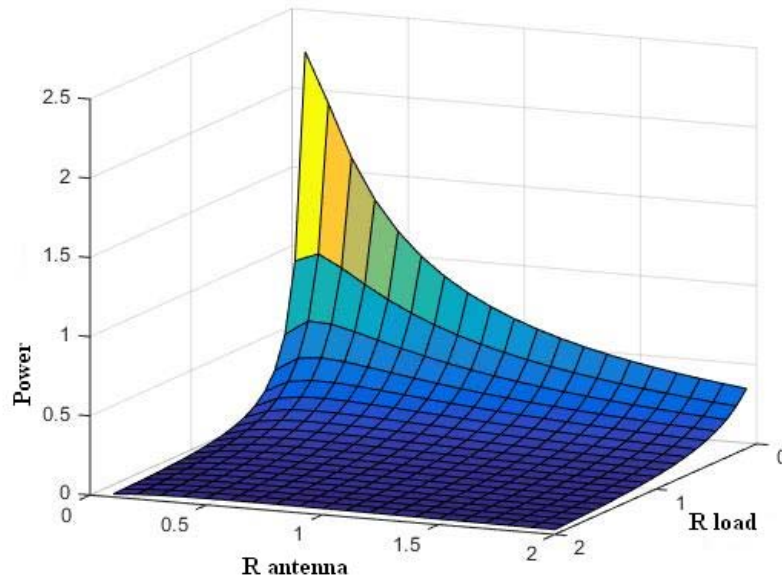


Figure 61: Load power versus R_A and R_L .

It can be noted that if the value of R_D is greater than the values of R_A and R_L , the power in the diode becomes very low and the power in the antenna and in the load are of the same order of magnitude. If the values of R_D , R_A and R_L are similar, the power in the antenna, in the rectifier and in the load are distributed like in (18)-(20). The best impedance matching condition is obtained when the value of R_D is much larger than the values of R_A and R_L , and R_A and R_L are equal. In fact, the maximum of the curve of the power supplied to the load is shown when the value of R_A is equal to the value of R_L ; if the value of R_D is close to the values of R_A and R_L , the power in the load decreases. This makes the matching between a single rectenna and an external load very difficult, considering also the low output voltage. Moreover, a single rectenna is not able to supply efficiently an external load. Therefore, the optimal matching can be achieved by an array of optical rectennas whose equivalent impedance equals the harvesting circuit impedance Z_{boost} [43, 88-89]. The latter is typically a commercial DC-DC boost power converter. To the purpose of this work, the LTC3108 boost converter has been considered, whose input impedance Z_{boost} is equal to 2.5Ω .

The equivalent circuit of an array of optical rectennas is shown in Figure 62. Each cell consists of an antenna with the rectifier placed in the gap, as it can be shown in several examples in the literature [57, 91].

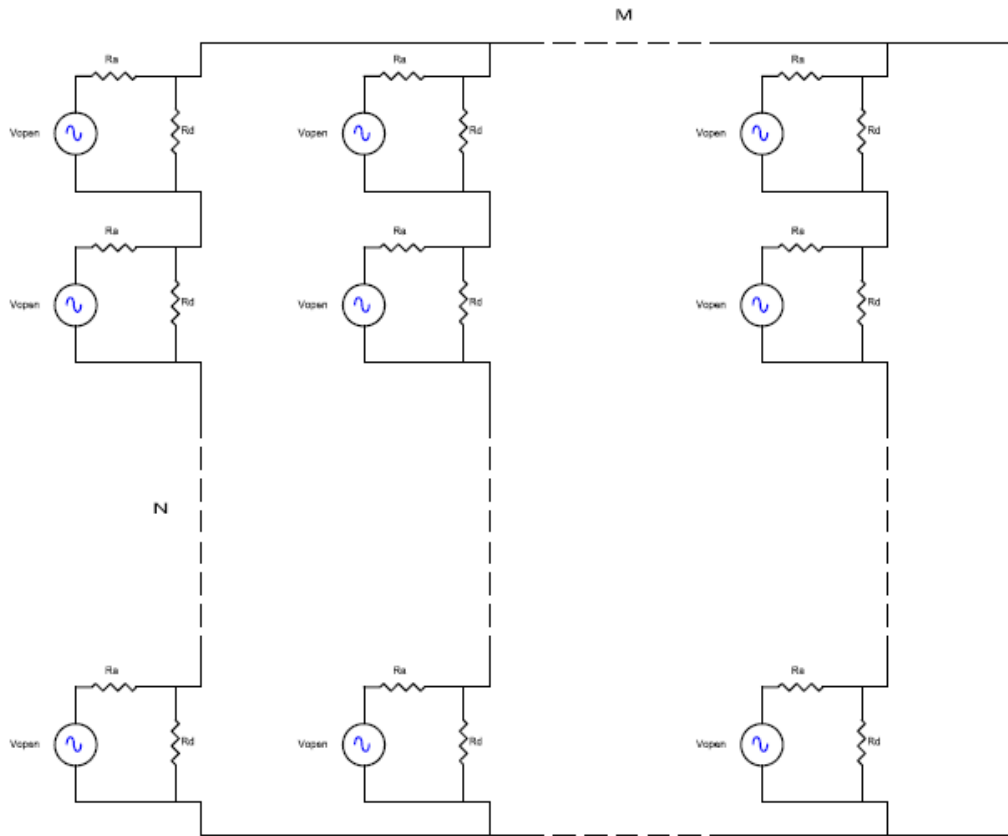


Figure 62: Equivalent circuit of an array of $N \cdot M$ optical rectennas

The equivalent resistance of a single rectenna R_{RECT} can be expressed as:

$$R_{RECT} = \frac{R_A R_D}{R_A + R_D} \quad (22)$$

The value of diode resistance R_D is assumed equal to 300Ω , typical for the state of art of MIM diode, whereas the value of the internal nanoantenna impedance R_A depends on the dipole arm length.

If N rectennas are series connected (matrix column), the value of the column resistance R_{COL} becomes equal to

$$R_{COL} = N \cdot R_{RECT} = N \cdot \frac{R_A R_D}{R_A + R_D} \quad (23)$$

This value is much higher than the value of the input impedance of the DC-DC boost converter. Therefore, the impedance matching between the array and the DC-DC boost converter is not satisfied.

As a consequence, the maximum power transfer between the harvesting system and the load is not obtained [43]. It is needed, thus, to decrease this value of resistance connecting in parallel M column.

Therefore, the equivalent resistance of an array composed of N series connected optical rectennas (string), parallel connected with M strings, is given by:

$$R_{eq,array} = \frac{N}{M} \cdot R_{RECT} = \frac{N}{M} \cdot \frac{R_A R_D}{R_A + R_D} \quad (24)$$

from which the ratio of N/M is obtained as:

$$\frac{N}{M} = R_{eq,array} \cdot \left(\frac{R_A + R_D}{R_A \cdot R_D} \right) \quad (25)$$

The choice of the values of N and of M depends on the DC-DC boost converter downstream to the array. In particular, N depends on the output voltage to be supplied to the DC-DC converter, whereas M depends on the DC-DC converter input resistance.

5.2 – Voltage matching

In order to achieve the voltage matching between optical rectenna and harvester, the rectenna output voltage has to be greater than the lower input voltage of DC-DC converter. This gives the lower limit for N. Considering that the minimum voltage of the harvester is of the order of 20 mV, the minimum voltage of the array has to be fixed to 40 mV. The maximum input voltage of the harvesting circuit is of the order of 400 mV. So, the higher limit for N can be obtained when the maximum output voltage of the array $V_{o,array}$ is fixed to 800 mV (this value is equal to 400 mV when the matching load is connected to the array). This is defined as the ratio between the maximum input voltage value of the harvester V_{Iboost} and the output voltage value at the rectenna V_{DC} . It should be noted that this value corresponds to a DC voltage whereas until now the antenna has been considered as an AC generator. The diode resistance and capacitance imply a rectifying behaviour giving the min value of the waveform obtained by a nanoantenna. The DC value can be obtained by the V_{open} by multiplying for $1/\pi$ (corresponding to an half-wave rectifier). Therefore, N can be obtained as

$$N = \frac{V_{O,array}}{V_{DC}} = \frac{2V_{Iboost}}{\frac{V_{open}}{\pi}} \quad (26)$$

From the formula 25, it is possible to calculate the value of M :

$$M = \frac{N}{R_{eq,array} \cdot \left(\frac{R_A + R_D}{R_A \cdot R_D} \right)} \quad (27)$$

Table 10 shows the values of N and M for nanodipoles whose arm length varies from 100 nm to 350 nm.

Table 10: Parameters of an array of optical rectennas

L [nm]	Z_{boost} [Ω]	V_{DC} [μV]	$V_{o,array}$ [mV]	N	M
100	2.5	6.143	800	130230	2944382
150	2.5	8.438	800	94810	418293
200	2.5	8.230	800	97206	2184405
250	2.5	6.822	800	117268	2549305
300	2.5	5.887	800	135893	2810611
350	2.5	5.729	800	139641	2873272

It can be observed that the order of magnitude of the number of rectennas in an array of optical rectennas coupled to the commercial DC-DC boost converter is about 10^{12} .

The array area can be expressed as

$$A_{array} = N \cdot M \cdot A_{dipole}. \quad (28)$$

Table 11 shows the values of the effective area and the geometric area of a rectenna array for dipole arm length between 100 nm and 350 nm.

Table 11: Effective area and geometric area of an array of optical rectennas

L [nm]	A_{eff} [mm^2]	A_{geom} [mm^2]	A_{eff}/A_{geom}
100	2144	3220.9	0.665
150	1245.6	2504.78	0.497
200	1027.22	3482.33	0.295
250	969.11	6098.22	0.159
300	977.12	9319.4	0.105
350	1013.66	11395	0.09

It can be noted that the effective area and the geometric area of each device are not the same. Therefore, it is possible to define a Figure of Merit (FOM) as the ratio between the effective area and the geometric area. This parameter is relative to the surface efficiency of the array of optical rectennas and is as better as the dipole arm length is lower. Considering the values in Table 11, the dipole of 100 nm exhibits the most favourable ratio [88-89].

5.3 – Load power and energy evaluation

In order to evaluate the available power on the load the equivalent circuit shown in Figure 63 has been considered.

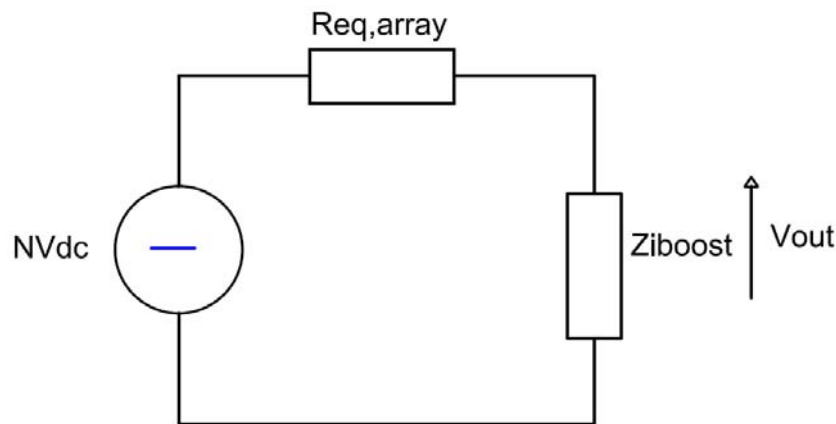


Figure 63: Equivalent circuit for calculation of rectenna array power

The impedance matching condition between the rectenna array $R_{eq,array}$ and the load Z_{Iboost} has been assumed. The load power can be calculated by

$$P_{load} = \frac{V_{out}^2}{Z_{Iboost}} \quad (29)$$

where V_{out} is the output voltage at the load Z_{Iboost} equal to $\frac{NV_{DC}}{2}$. From the values of N and of V_{DC} for each dipole and the value of Z_{Iboost} , the array power is equal to 64 mW. Considering the results shown in Table 10 and 11, it can be deduced that the best performance have been obtained by the 150 nm dipole. The 150 nm arm length dipole allows to obtain the lowest product $N*M$ minimizing the overall area of the array. On the basis of the results summarized in Tables 10 and 11, it can be deduced that the dipole of 150 nm arm length exhibit, maintaining the same power on the load and the same voltage at

the DC-DC boost terminals, the highest value of the single rectenna output voltage and consequently the lowest size in terms of $N \times M$ matrix. In addition, the same dipole has a good ratio effective area over geometric area. For this reason, the evaluation of the delivered energy is performed in the following considering this kind of dipole.

Figure 64 shows the curve of solar radiation versus time during a typical day of July in Palermo (south of Italy, 38.1157° N, 13.3613° E). It can be noted that the maximum of the solar radiation is at the Zenith.

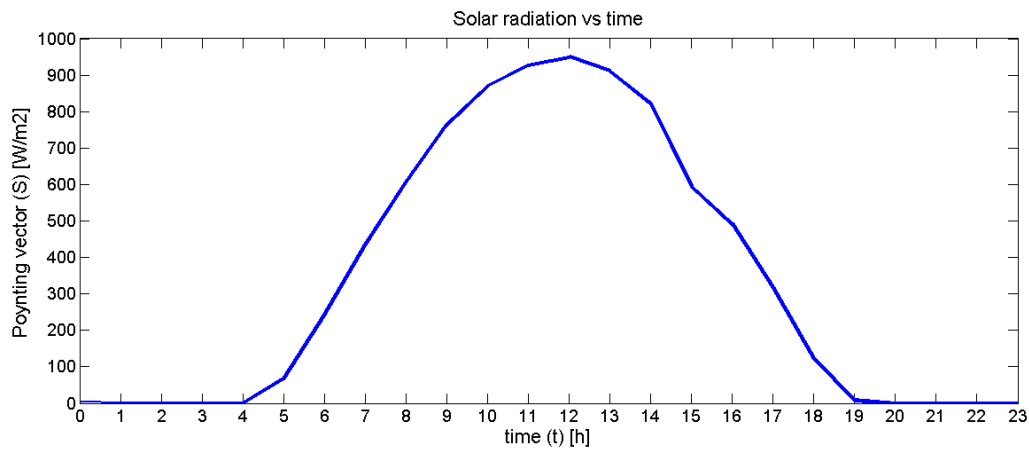


Figure 64: Solar radiation versus time

The energy that can be delivered by an array of optical rectennas in a day can be expressed as:

$$\xi_{day} = \int_t P_{array} \frac{R(t)}{R_{max}} dt \quad (30)$$

where $R(t)$ is the solar radiation versus time, R_{max} is the value of solar radiation at Zenith and P_{array} is the maximum value of the array power. On the basis of the curve shown in Figure 64, the energy delivered to the LTC3108 DC-DC boost power converter, whose maximum input voltage and input impedance are equal to 400 mV and 2.5Ω respectively, has been obtained. Under matching impedance conditions, the array output power and the boost input power are the same and equal to 64 mW. Therefore, the array output energy, calculated on the basis of formula (30), is equal to 1970.52 J. This energy is able, for example, to charge a supercapacitor whose voltage is equal to 5 V and whose capacitance is equal to about 157 F. If the operating voltage range of a common RF transceiver is about 0.5 V and the current is on the order of 30 mA, this value of the capacitance allows the operating mode for about 40 minutes. The other dipoles analyzed need higher dimensions for both N and M and higher surfaces in order to deliver the same energy [88-89].

5.4 – Power evaluation under diode impedance mismatching

The available power on the DC-DC boost converter P_{load} can be calculated as

$$P_{load} = \frac{V_{out}^2}{Z_{Iboost}} = \frac{\left[\frac{N \cdot \frac{V_{open}}{\pi} \cdot Z_{Iboost}}{\frac{N}{M} \cdot \left(\frac{R_A \cdot R_D}{R_A + R_D} \right) + Z_{Iboost}} \right]^2}{Z_{Iboost}} \quad (31)$$

In our case considering R_D equal to 300Ω , the output power is about 64 mW. This value represents a technological limit. A further reduction of R_D would allow the output power to be double; it corresponds to the condition R_D equal to R_A as described in the literature [24, 33, 56, 83, 93]. On the other hand, an increase of R_D does not imply a significant reduction of the power.

Figure 65 shows the trend of P_{load} versus diode resistance R_D .

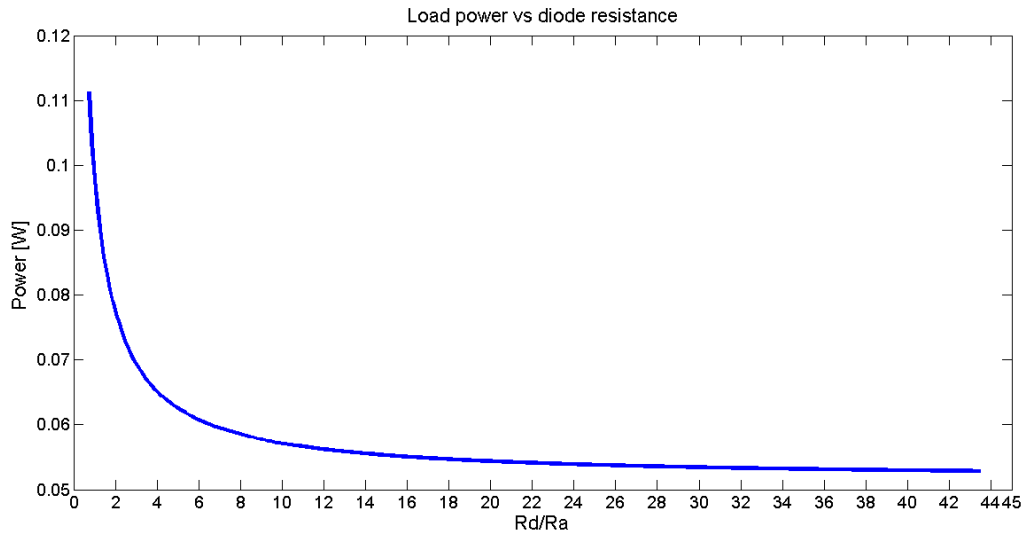


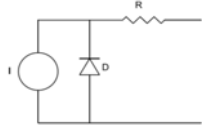
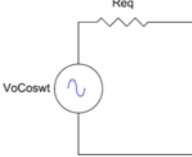
Figure 65: Load power versus diode resistance

The available power on the DC-DC boost converter when it is connected to the array of rectennas whose dipole arm length L is equal to 150 nm has been evaluated. The value of the diode resistance R_D is varied in a range from 50Ω to 3000Ω with steps of 10Ω . It can be noted that when the value of R_D increases, the power on the boost decreases and tends towards a saturation value [88-89].

5.5 – Comparison between Photovoltaic cells and optical rectenna

In Table 12, the main traditional PV cells and the optical rectennas features are compared.

Table 12: Comparison between traditional PV cells and rectennas

	<i>Traditional PV cell</i>	<i>Rectenna</i>
Source Model		
MPPT	Required	Not required
P	High	low
V, I	Single cell	Array
η	10 ÷ 20%	Higher

It can be noted that a voltage source, V_{open} , and an impedance in series Z_{eq} model the optical rectenna, while a current source, a diode and an impedance represent traditional PV cells. Therefore, the value of nanoantenna impedance is crucial for the design and characterization of an optical rectenna. The traditional PV cells, instead, require the maximum power point tracking (MPPT) and provide the values of output power higher than the rectenna values. Moreover, the traditional PV cells depend on solar radiation whereas the rectenna also could work in the absence of solar radiation exploiting the infrared radiation. In particular, with respect to the traditional PV cells, in principle the rectenna is able to exploit energy also at temperature lower than that of the solar radiation. In order to obtain solar energy harvesting, a single traditional PV cell can be used. The output power and voltage of a single optical rectenna are very low, of the order of picowatt and microvolt respectively; consequently, an array of optical rectennas is needed to harvest solar radiation and to supply an external load. The theoretical values of rectenna solar energy harvesting efficiency are much higher than the PV efficiency values. The conversion efficiency of a rectenna depends on the power loss in the diodes, on the impedance matching between the nanoantenna, the rectifier and the load, and on the nanoantenna efficiency [24, 41]. In the literature, a great variety of nanoantenna structures depending on the geometry of nanoparticles can be found [27, 42]. The radiation efficiency of nanoantennas depends on the metal used as conductor and on the dimension of the nanoantenna. The most used metals are gold, silver, aluminum and copper, whose plasmonic properties lie in the optical range. Therefore, an accurate choice of materials and design of nanoantenna is most important for its efficiency [56]. Relatively to the rectifier, the main problems regard diode resistance, capacitance, and reverse-bias leakage. The diode resistance has to be sufficiently low in order to achieve a significant reduction of power loss; the diode capacitance has to be small in order to have a fast diode. The significant current for negative voltages in the diode is

required to be lower, approximately $1\mu\text{A}$ or less [33]. Another issue is the impedance matching between the optical rectenna and the load. The latter is typically a DC-DC boost power converter, modelled by an equivalent input impedance. Considering the values of the internal nanoantenna impedance, the diode impedance and the harvesting circuit input impedance, the optimal matching can be achieved by a nanoantenna array whose equivalent impedance equals the harvesting circuit impedance [43].

Conclusion

The main guidelines for the design of an array of optical dipole rectennas to harvest the energy coming from solar radiation has been defined. In particular, the optimal impedance matching between the array and the load has been investigated in order to allow the maximum power transfer. In the case of a single optical rectenna, the best impedance matching condition is obtained when the value of the diode resistance R_D is much larger than the values of the internal nanoantenna impedance R_A and of the load resistance R_L , and R_A and R_L are equal. Considering the values of the internal nanoantenna impedance, the diode impedance and the harvesting circuit input impedance, the optimal matching cannot be achieved by a single rectenna system. The power delivered to a load can be maximized by matching the impedance of the nanoantenna and the impedance of the load. The optimal impedance matching can be obtained by arranging the rectennas in a matrix of $N*M$ optical rectennas to supply a commercial DC-DC boost converter for harvesting applications. The equivalent impedance of the array has to be equal to the harvesting circuit impedance. The choice of the values of N and of M depends on the DC-DC boost converter downstream to the array. In particular, N depends on the output voltage to be supplied to the DC-DC converter, whereas M depends on the DC-DC converter input resistance. The order of magnitude of the number of rectennas in an array of optical rectennas coupled to the commercial DC-DC boost converter is about 10^{12} . The effective area and the geometric area of each device are not the same. Therefore, a Figure of Merit (FOM) as the ratio between the effective area and the geometric area has been defined. This parameter is relative to the surface efficiency of the array of optical rectennas and is as better as the dipole arm length is lower. The best results have been obtained by the 150 nm dipole since it exhibits the highest value of the single rectenna output voltage and consequently the lowest area in terms of $N*M$ matrix. In addition, the same dipole has a good ratio effective area over geometric area. For this reason, the evaluation of the delivered energy has been performed considering this kind of dipole. The energy produced in a July sunny day has been calculated. This energy is able to charge a supercapacitor of about 150 F with voltage equal to 5 V. The curve of the available power on the DC-DC boost converter P_{load} as a function of the diode resistance R_D for a 150 nm arm length dipole has been calculated. In particular, the value of the diode resistance R_D has been varied in a range from 50 Ω to 3000 Ω in steps of 10 Ω . It can be noted that when the value of R_D increases, the power on the boost decreases and tends towards a saturation value.

Finally, the differences between photovoltaic cells and rectenna has been highlighted. A voltage source, V_{open} , and an impedance in series Z_{eq} model the optical rectenna, while a current source, a diode and an impedance represent traditional PV cells. Therefore, the value of nanoantenna impedance is crucial for the design and characterization of an optical rectenna. The traditional PV cells, instead, require the maximum power point tracking (MPPT) and provide the values of output power higher than the rectenna values. Moreover, the traditional PV cells depend on solar radiation whereas the rectenna also could work in the absence of solar radiation exploiting the infrared radiation. The theoretical values of rectenna solar energy harvesting efficiency are much higher than the PV efficiency values. In order to obtain solar energy harvesting, a single traditional PV cell can be used. On the contrary, since the output power and voltage of a single optical rectenna are very low, of the order of picowatt and microvolt respectively, an array of optical rectennas is needed to harvest solar radiation and to supply an external load. The array output energy is equal to 1970.52 J. This energy is able, for example, to charge a supercapacitor whose voltage is equal to 5 V and whose capacitance is equal to about 157 F.

The analysis performed in this chapter represents a worst case scenario since the range of interest for the collected radiation has been limited to 300 nm and 1200 nm, equivalent to a frequency range of 250 THz ÷ 1000 THz and the rectifying diode impedance has been assumed to be equal to the best value allowed by the actual technology.

The output impedance of the array of optical rectennas usually changes with the solar radiation during a day, which depends on the Sun position. Therefore, in order to achieve an optimal impedance matching between the array and the harvester and, as a consequence, a maximum power transfer, an external control circuit that dynamically allows to obtain the impedance matching conditions is needed. This circuit will be explained in details in the following chapter.

Despite several limitations, the designed matrix of rectennas appears very promising for energy harvesting purposes.

CHAPTER VI – MAXIMUM POWER TRANSFER OPTIMIZATION

This section considers the optimization of the maximum power transfer between the array of optical rectennas and the harvesting circuit. At the beginnings, the external control technique will be discussed. The design of the external control circuit in order to dynamically obtain the impedance matching conditions will be defined. Finally, a description of the implemented external control circuit and several tests will be performed.

6.1 – External converter control

The DC-DC boost converter chosen for the purpose of this work is the LTC3108. This device operates from input voltages as low as 20 mV. The maximum value of input voltage is 500 mV. The absence of a maximum power point tracking system involves that the input impedance of the converter would not be controlled immediately as the rectenna supplied voltage changes. Since the impedance matching between the DC-DC converter and the array of optical rectennas is needed in order to obtain the maximum power transfer between the harvesting system and an external load, the use of an external control is required in order to regulate the input converter impedance. The Demonstration Circuit 1582B of the LTC3108 makes possible to access the SW pin, connected to the gate of the MOSFET, by means of the welding area of the capacitor C_2 , as it can be shown in Figures 66 a) and 66 b).

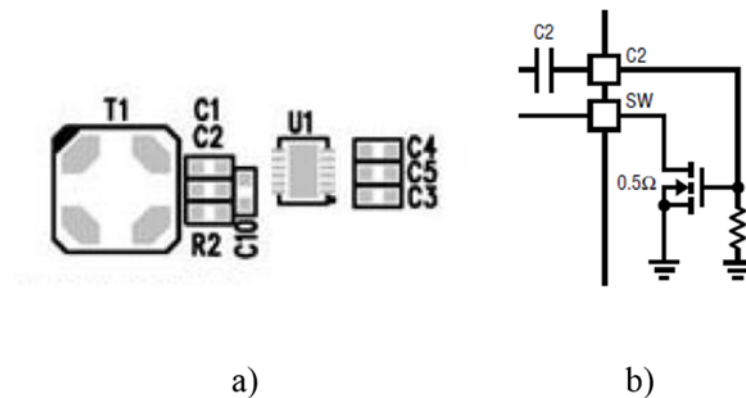


Figure 66: a) Detail of the LTC3108 board; b) Detail of the LTC3108 block diagram [132, 135]

The accessing the gate of the MOSFET allows to control the duty cycle of the LTC3108 by means of an external signal, to interrupt the switching cycle for a certain time interval, reducing thus the pulse train that turns on the switch, and to decrease the average value of the LTC3108 input current I_{IN} . The simulations of the equivalent circuit of the self-oscillating stage of the LTC3108, performed by means of PowerSIM software, have allowed to verify the decrease of the LTC3108 input current stopping the

pulse train through an external signal for a certain time interval. Figure 67 shows the equivalent circuit simulated by the PowerSIM software.

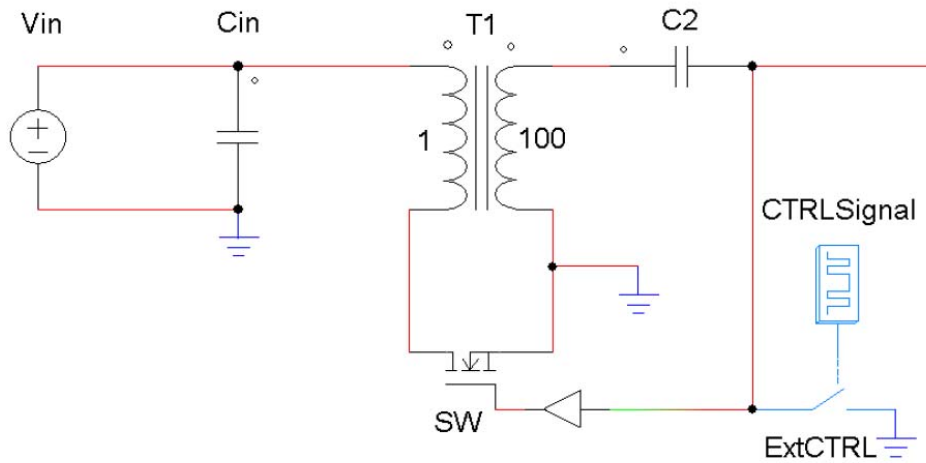


Figure 67: Equivalent circuit of the simulated self-oscillating stage of LTC3108

Figures 68 show the curves of reducing of the self-oscillating stage pulse train versus time.

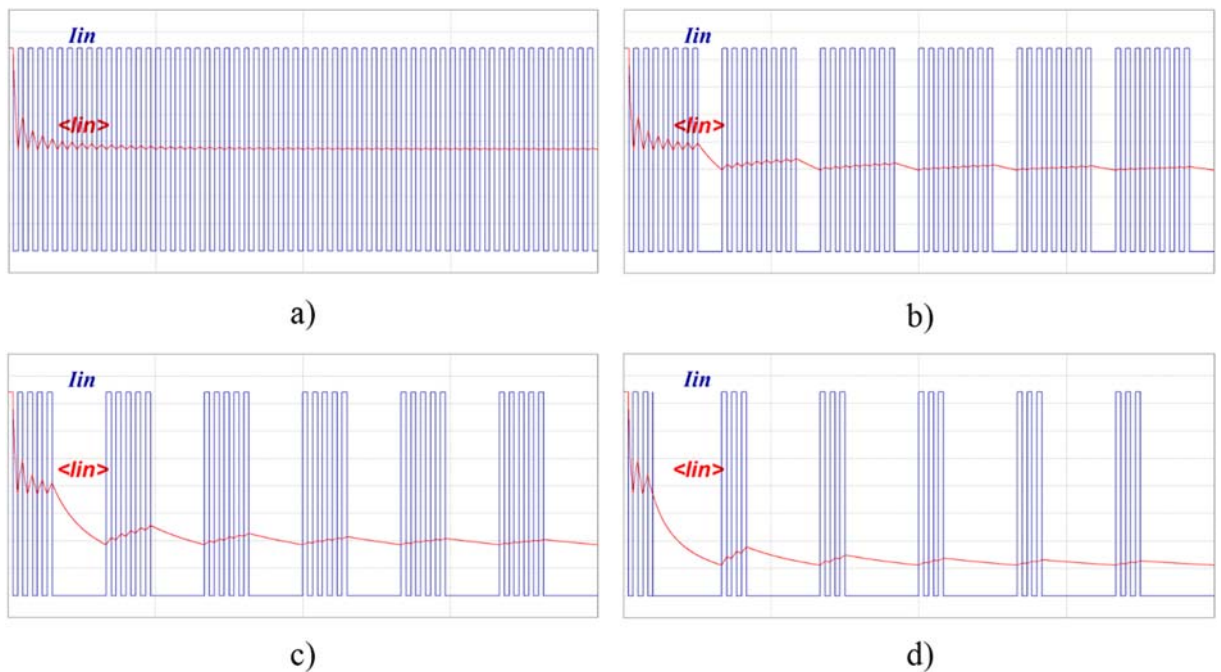


Figure 68: Trend of the reducing of the self-oscillating stage pulse train for different time intervals

It can be noted that in correspondence of the same value of the input voltage V_{IN} , the decreasing of the input current I_{IN} results in the increase of the DC-DC boost converter input impedance R_{IN} . In

addition, these trends of the LTC3108 input current and of its average value confirm that it is possible to obtain dynamically an impedance matching between the harvester and the array of optical rectennas through an external control. The latter has to connect to the ground the input of the switch of the converter, which turns off. Several simulations of the equivalent circuit of the self-oscillating stage with an external signal have been performed for different values of the duty cycle of the square-wave external signal, which short-circuits the gate of the MOSFET, obtaining thus the reduction of the pulse train, as it is shown in Figures 69.

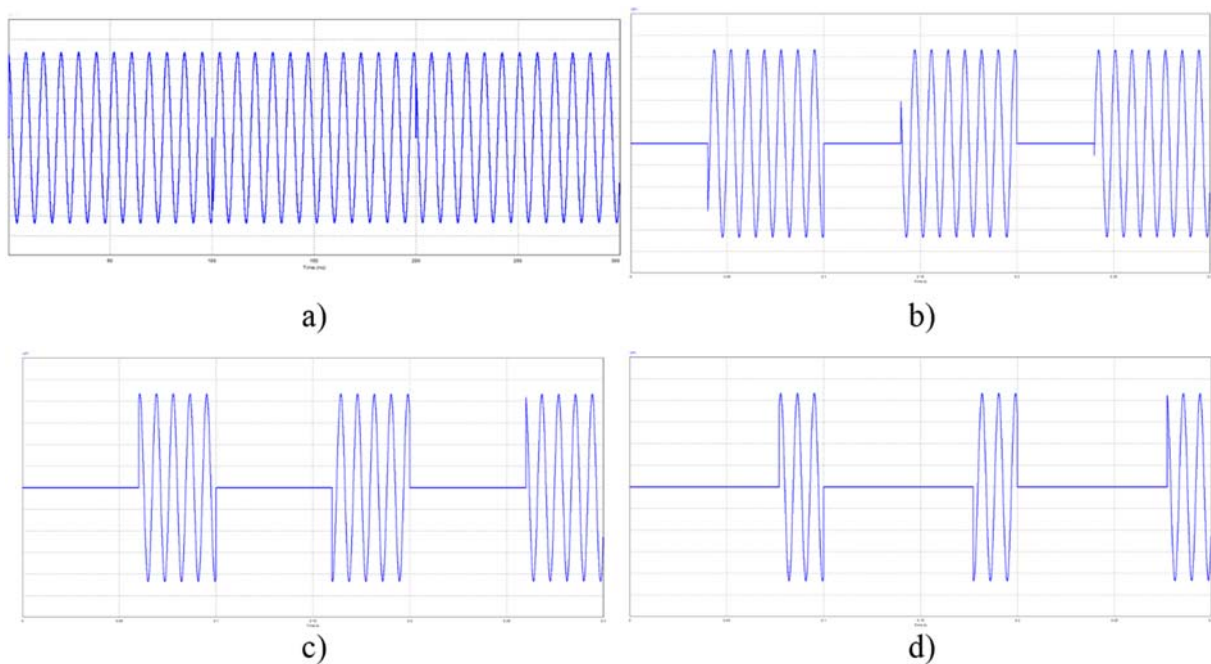


Figure 69: Gate voltage of the MOSFET as a function of the external control

The control of the MOSFET gate has to be implemented when the increase of the value of the DC-DC boost converter input impedance is needed. Otherwise, this control has not to operate and to supply the MOSFET gate, compromising in this case the normal operation mode of the converter. The short-circuit of the gate is realized connecting the external control circuit to the welding area of the capacitor C_2 .

6.1.1 – Open collector

In order to implement the external control of the gate of the MOSFET, a logic port has to be used. In particular, at the beginning a NOT open collector port compatible with most TTL families has been considered. The SN74LS06 is a hex inverter buffers and drivers with open collector high voltage outputs. It is used to interface with high-level circuits and to drive TTL inputs. This device is

characterized by two different output states. When the input is “High”, the output is “Low”, whereas when the input is “Low”, the output is in “High impedance” state. A typical functional block diagram is shown in Figure 70 [136].

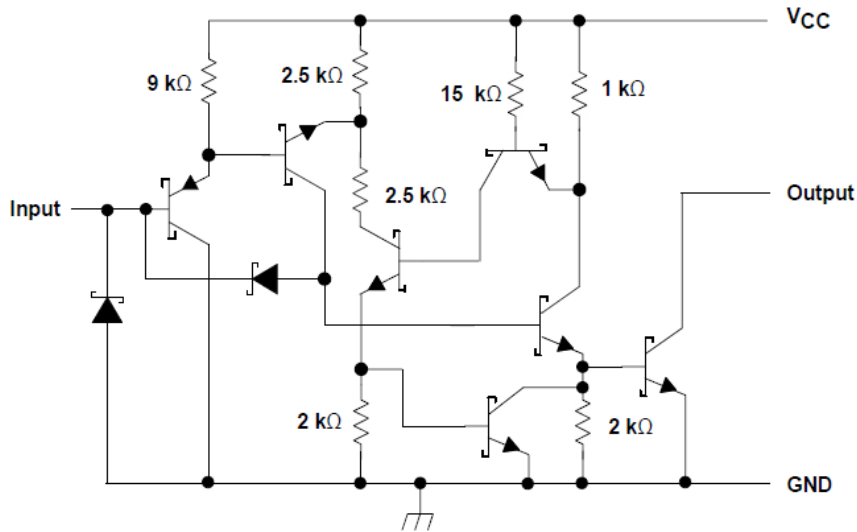


Figure 70: SN74LS06 functional block diagram [136]

The experimental rig, shown in Figure 71, has employed a DMM4050 Digital Multimeter (Tektronix, OR, USA), a E3615A Power Supply (Hewlett-Packard, CA, USA), a MSO6104A Oscilloscope (Agilent Technologies, CA, USA), a 1582B Demo Circuit (Linear Technology Corporation, CA, USA), a PM5138 Function Generator 0.1 MHz – 10 MHz (Philips, USA) which generates the input square wave of the open-collector port.

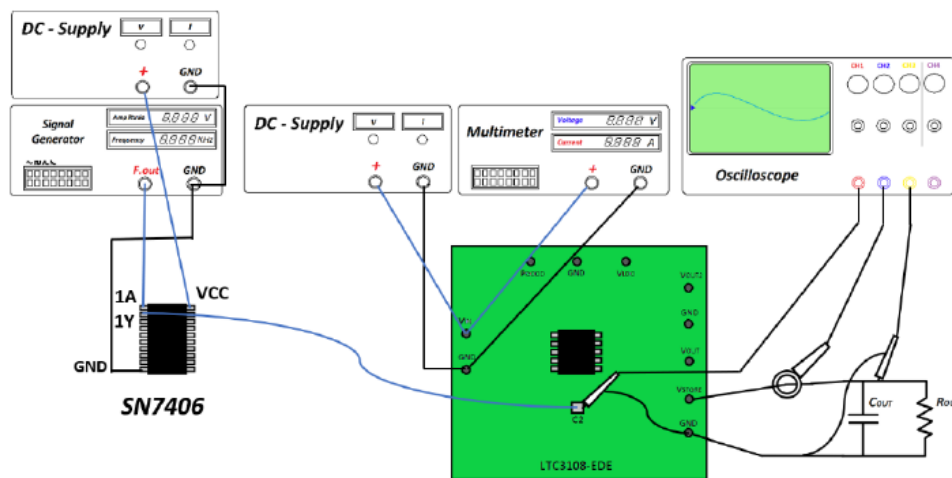


Figure 71: Experimental rig

Regardless of the control signal at the input of the NOT open-collector port, once this port is connected to the capacitor C_2 , the converter output voltage begins decreasing and the pulse train at the gate becomes zero. This is because the open-collector internal resistance charges the converter self-oscillating stage even there is not signal at its input. Therefore, this type of logic port cannot implement the external control. The NOT three-state port has instead employed.

6.1.2 – Not three-state port

The NOT three-state port have three output states, “High”, “Low” and “High impedance”. The latter allows to disconnect the device from the other parts of the circuit. A type of the SNx4LS24x families has been implemented. In particular, the SN74LS244, which is an octal buffers and line drivers specifically for three-state memory address drivers, clock drivers and bus-oriented receivers and transmitters. This port is compatible with most TTL families made in Low Schottky technology having operating frequencies on the order of tens MHz. The SN74LS244, shown in Figure 72 a), is a 20-pin chip which is characterized by two NOT line ports and 3-state outputs which are controlled by two different inputs. The logic diagram is shown in Figure 72 b) [137].

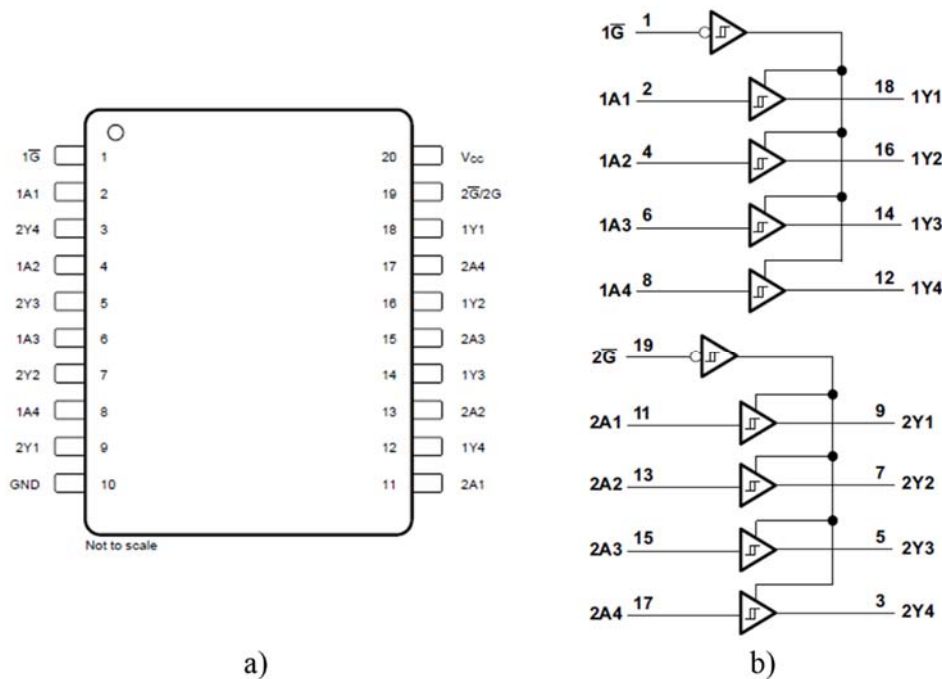


Figure 72: a) SN74LS244 3-state octal buffer; b) SN74LS244 functional logic diagram [137]

The input and the output of each buffer are sketched in Figures 73.

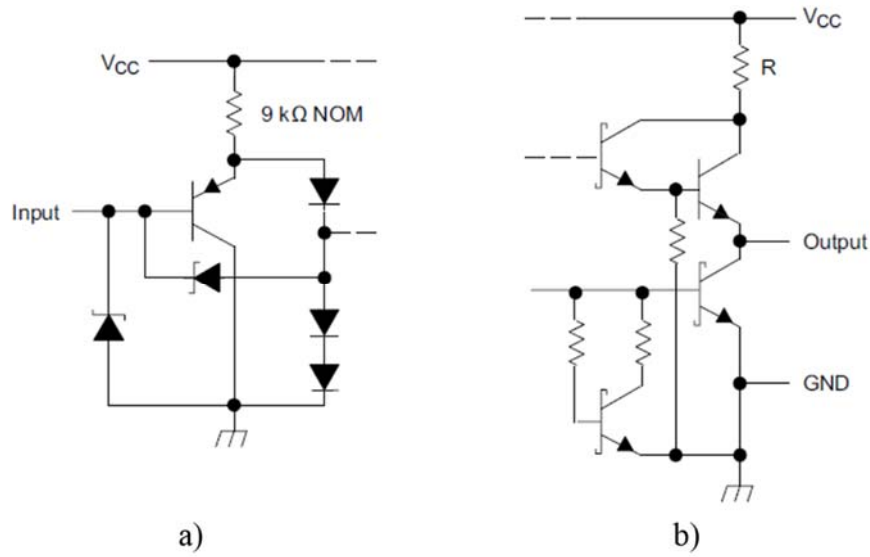


Figure 73: a) SN74LS244 typical input; b) SN74LS244 typical output [137]

Table 13 shows the function table of the SN74LS244 [137].

Table 13: SN74LS244 function table

Inputs		Outputs
\bar{G}	A	Y
L	L	L
L	H	H
H	X	Z

The experimental rig, shown in Figure 74, is equal to that has been used for the tests with the NOT open-collector port.

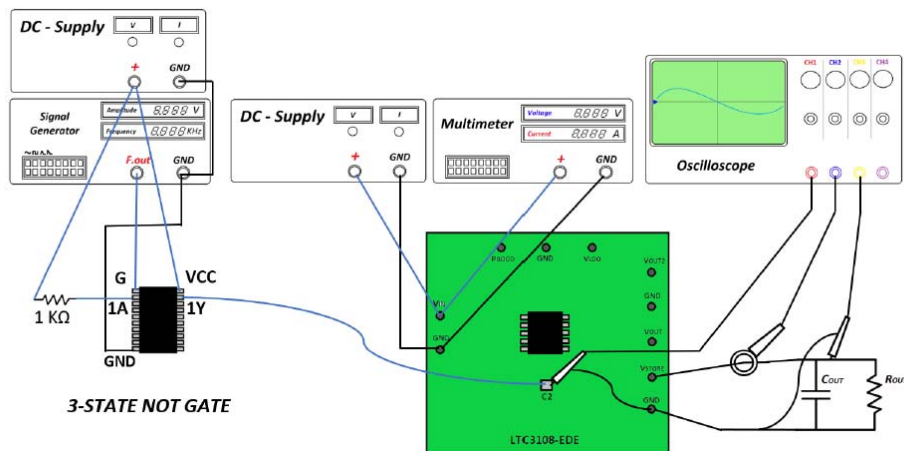


Figure 74: Experimental rig

The first of the eight buffers is connected at the input to V_{CC} through the pull-up resistor, at the output to the pin C_2 of the LTC3108 Demonstration Circuit. The square-wave control signal at a frequency of 1 kHz is connected instead to the control pin \bar{G} . The value of the control signal frequency has been chosen in order to be much lower than the switching frequency of the converter, the latter on the order of 44 kHz. When the square-wave is “High”, the three-state port is in “High impedance” state regardless of the input 1A. Otherwise, when the square-wave is “Low”, the three-state port turns on and the output 1Y becomes “Low”, i.e. equal to the ground. This means that at the C_2 pin there is a turnover of the “High impedance” state Z, which corresponds to a virtual disconnection of the external control, and of the “Low” state L, which corresponds to the short-circuit to the ground. The time interval in correspondence of the output “Low” state is T_{OFF} . This time depends on the duty cycle of the square-wave, which control the three-state port. The higher D, the lower T_{OFF} . This means that in correspondence of high values of D the current decreases are smaller, whereas in correspondence of low values of D, the current decreases are greater because the converter pulse train is reduced. An increase of the values of the input impedance thus is expected. Figures 75, 76 and 77 show the measures performed with the three-state port. In all the Figures the green curve is the input current I_{IN} , the purple curve is the gate pulse V_{C_2} , the yellow curve is the output voltage at C_{OUT} equal to 220 μ F. The duty cycle of the square-wave varies from 95% to 35%.

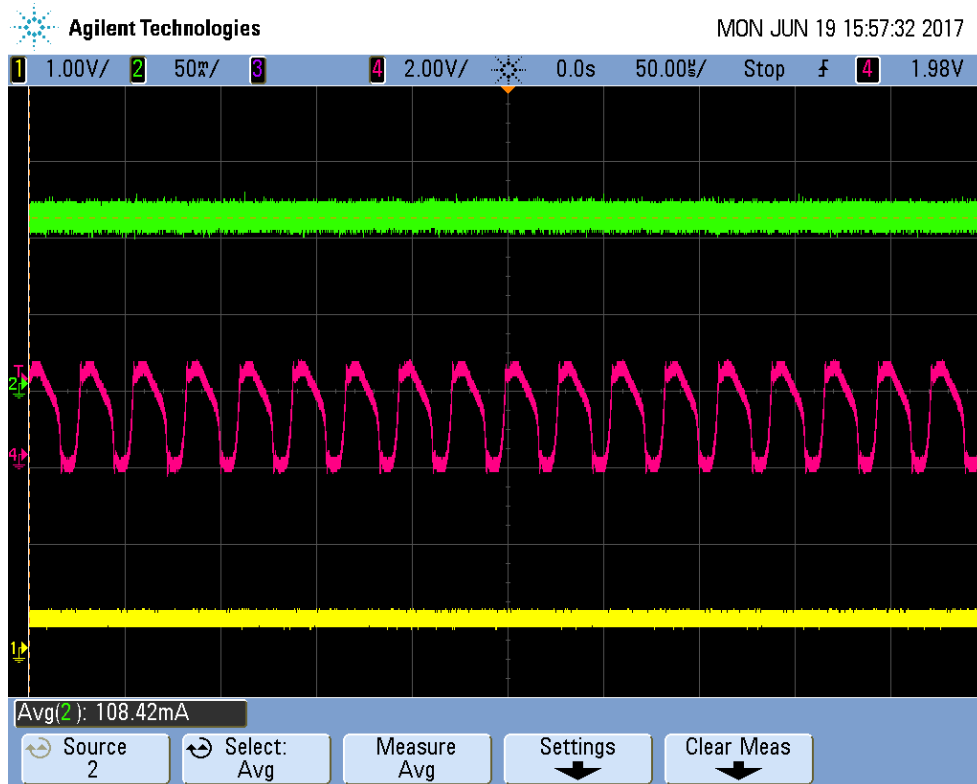


Figure 75: Converter control at $D = 95\%$

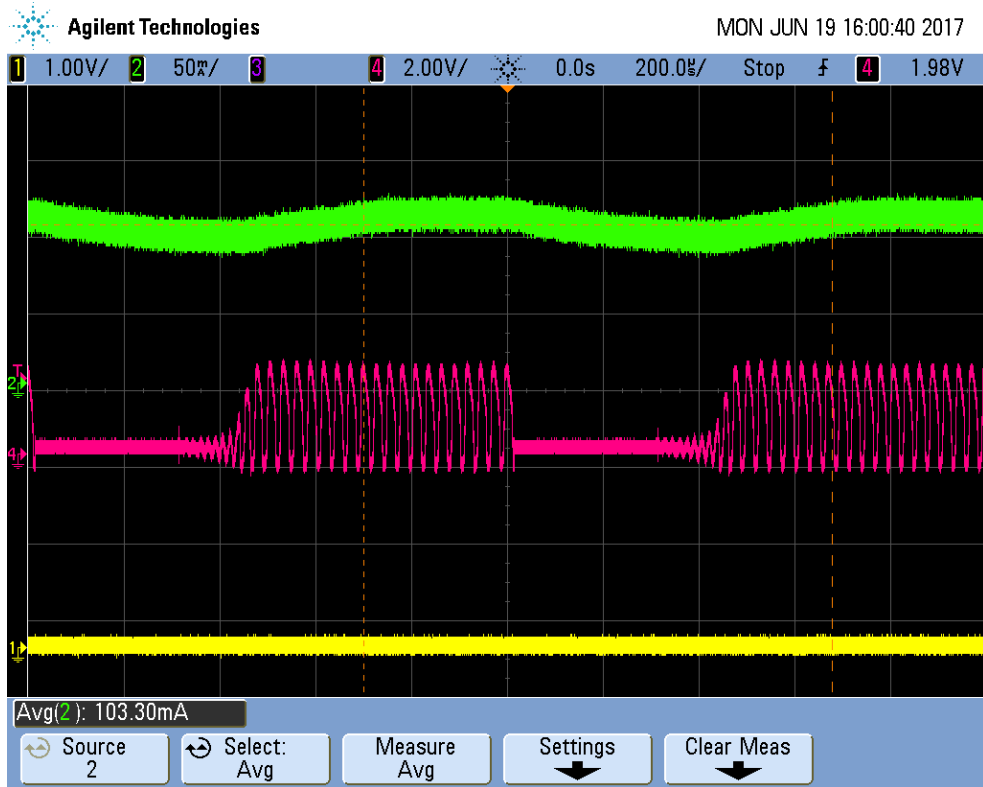


Figure 76: Converter control at D = 50%



Figure 77: Converter control at D = 35%

Table 14 summarizes the values of I_{IN} e R_{IN} in correspondence of a variation of D and for the same value of the input voltage of 40 mV.

Table 14: Input current I_{IN} and input impedance R_{IN} values

V_{IN} [mV]	D	I_{IN} [mA]	R_{IN} [Ω]
40	0.20	45.00	0.89
40	0.35	51.25	0.78
40	0.50	55.00	0.73
40	0.95	65.20	0.64

Figure 78 shows the trend of the input impedance versus the variation of the duty cycle D of the square-wave. It can be noted that it is possible to regulate the converter input impedance by means of the external converter control described in this section.

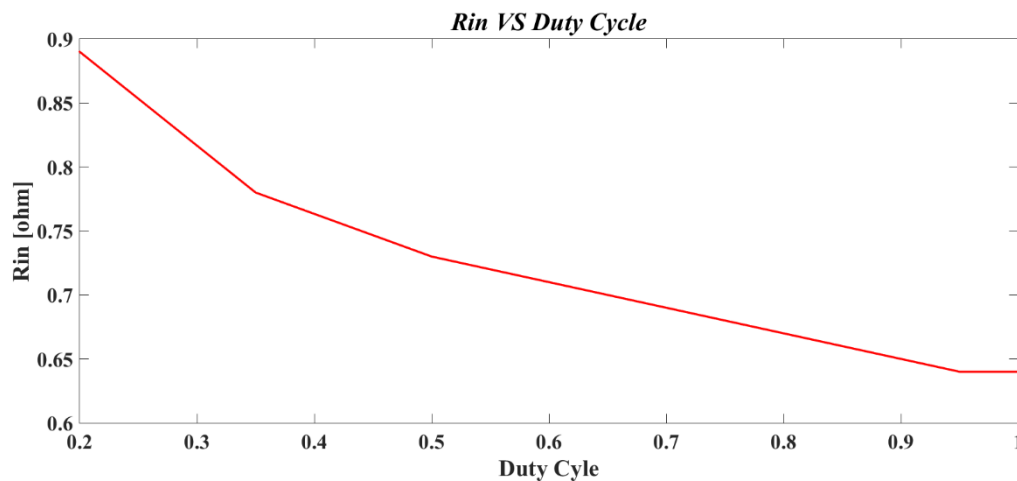


Figure 78: Input impedance R_{IN} versus square-wave duty cycle D

6.2 – Control circuit

The output impedance of the array of optical rectennas varies with the change of the radiation conditions, which depends on the position of the Sun during the day. Therefore, the control of the gate of the MOSFET has to be implemented when the condition of the impedance matching is not satisfied. Otherwise, this control has not to operate and to supply the MOSFET gate, compromising in this case the normal operation mode of the converter. The NOT three-state port can be employed as a switch able to cancel the pulse train at the gate of the MOSFET. In the following subsections, the design of an external control circuit which allows to enable or to disable the control on the DC-DC converter will be explained.

6.2.1 – Design of control circuit

The NOT three-state port can be driven by the square-wave signal at the pin \bar{G} . In this way, the output 1Y can switch from the “High impedance” state to the “High” or “Low” state, depending on the value at the input 1A. In order to disable its operation, the three-state port is driven by an OR port, made in Low Schottky technology. The SN74LS32 is a quadruple 2-input positive OR gate, whose connection diagram and logic diagram are sketched in Figures 79a) and 79b) respectively [138].

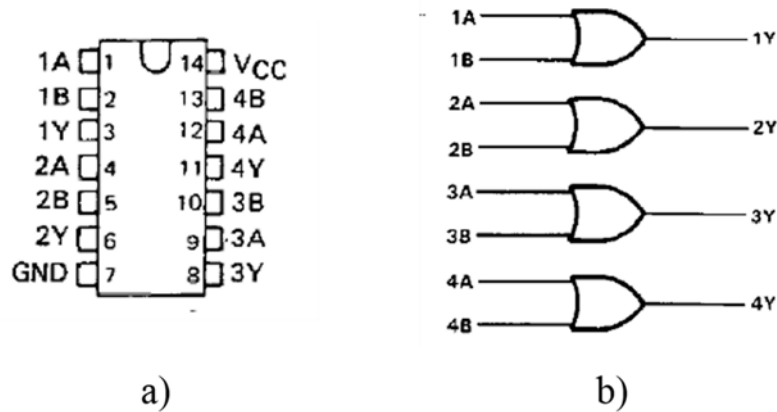


Figure 79: a) SN74LS32; b) Logic diagram [138]

Figure 80 shows the schematic of each OR gate [138].

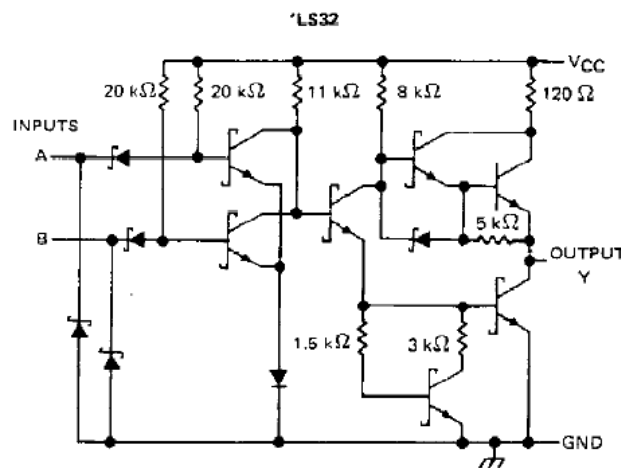


Figure 80: Schematic of the SN74LS32 [138]

As it can be noted in Table 15, the output of the OR port is in “Low” state only if both inputs A and B are in “High” state. If one of the two input is “High”, the output is “High”.

Table 15: SN74LS32 function table [138]

<i>Inputs</i>		<i>Outputs</i>
A	B	Y
H	X	H
X	H	H
L	L	L

This involves that only once the input B is in “Low” state, the output Y follows the square-wave signal at the input A. In the designed external control circuit, the OR port drives the three-state port and it is connected to the pin \bar{G} , as it can be noted in the logic diagram shown in Figure 81.

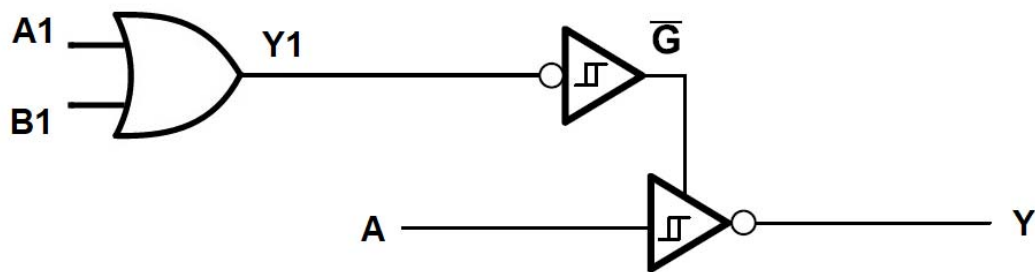


Figure 81: Logic diagram of the three-state port driven by the OR port

Table 16 shows the function table of this circuit.

Table 16: Function table of logic diagram in Figure 81

<i>OR Gate</i>			<i>3-state NOT Gate</i>		
A1	B1	Y1	\bar{G}	A	Y
H	X	H	L	X	Z
X	H	H	L	X	Z
L	L	L	H	L	H
L	L	L	H	H	L

In order to drive the three-state port, the OR input A1 is short-circuit to the ground while the square-wave signal is applied at the OR input B1. In this way, the turn-on and the turn-off of the three-state port is complementary with respect to the square-wave signal. In particular, the three-state output Y is in “High impedance” state Z when the square-wave signal is “High”, whereas the three-state output Y is equal to the three-state input A when the square-wave is “Low”. Therefore, depending on the three-state input A, two case studies may arise.

- 1) The three-state input A “Low”. If the OR input A1 is “Low” and the OR input B1 is “Low”, the three-state output Y is “High”, whereas if the OR input A1 is “Low” and the OR input B1 is “High”, the three-state output Y is in “High impedance” state Z. As a consequence, as the duty cycle increases, the circuit is in “High impedance” state for a longer time. During the control, the gate is thus not short-circuit to the ground. The value of its voltage is instead equal to output three-state port voltage V_Y . The control to the gate of the MOSFET is greater for low values of the duty cycle D. Therefore, the external circuit operates in negative logic.
- 2) The three-state input A is “High”. If the OR input A1 is “Low” and the OR input B1 is “Low”, the three-state output Y is “Low”, whereas if the OR input A1 is “Low” and the OR input B1 is “High”, the three-state output Y is in “High impedance” state Z. As the duty cycle increases, the external circuit operates in negative logic. In this case, during the control, the gate is short-circuit to the ground.

The operation in negative logic is because the three-state control pin is implemented by a NOT port. In order to obtain an external control circuit operating in positive logic, the use of another NOT port between the OR output and the three-state control pin is needed. This allows that as the value of the duty cycle increases, the time during that the gate is controlled is longer. To this purpose, a NAND port operating as a NOT port has been implemented. The SN74LS00 is a quadruple 2-input NAND gate made in Low Schottky technology, whose connection diagram and logic diagram are sketched in Figures 82a) and 82b) respectively [139].

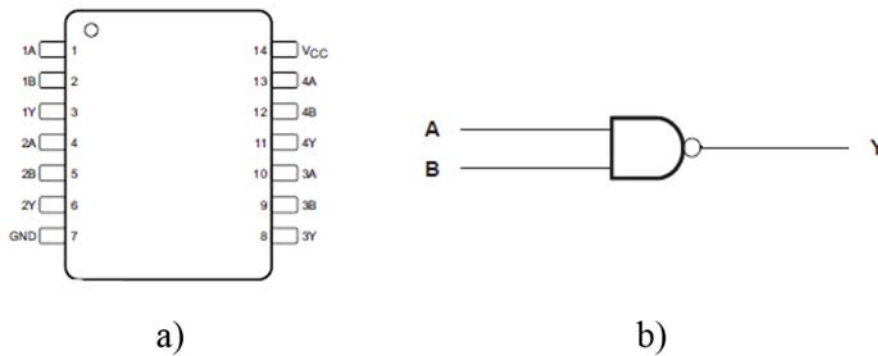


Figure 82: a) SN74LS00; b) Logic Diagram of each gate [139]

As it can be noted in Table 17, the output of the NAND port is in “Low” state only if both inputs A and B are in “High” state. If one of the two input is “Low”, the output is “High”.

Table 17: SN74LS00 function table [139]

<i>Inputs</i>		<i>Outputs</i>
A	B	Y
L	X	H
X	L	H
H	H	L

Connecting one of the two NAND input to the V_{CC} by means of a pull-up resistor, the NAND output Y is equal to the inverter of the other input. The NAND port thus behaves as a NOT port. In this way, the external control circuit operates in positive logic and, as the duty cycle increases, the time during that the gate is controlled is longer. The logic diagram of the circuit consisting of the OR port, the NAND port and the three-state port is shown in Figure 83. Table 18 summarizes its function table.

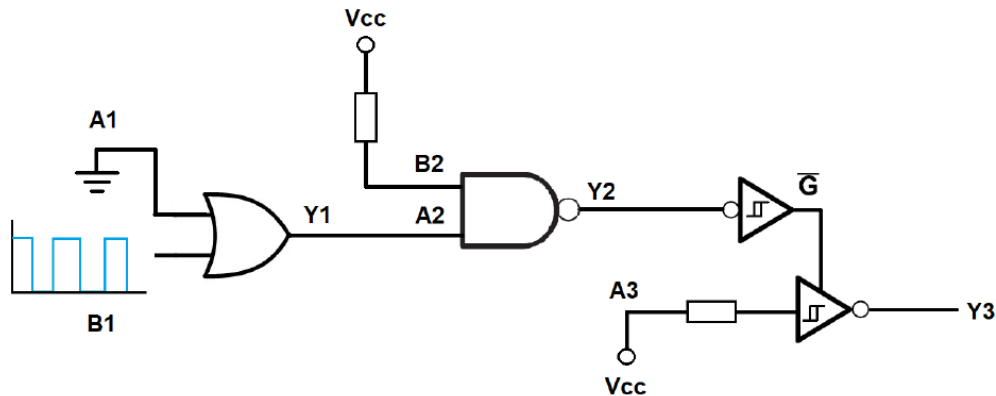


Figure 83: Logic diagram of the circuit with the OR port, the NAND port and the three-state port

Table 18: Function table of logic diagram in Figure 83

<i>OR Gate</i>			<i>NAND Gate</i>			<i>3-state Gate</i>		
A1	B1	Y1	A2	B	Y2	\bar{G}	A3	Y3
L	H	H	H	H	L	H	H	L
L	L	L	L	H	H	L	H	Z

The OR input A1 is short-circuit to the ground in order to allow that the OR output Y1 follows the square-wave signal. The NAND input B2 is connected to V_{CC} by means of the pull-up resistor, operating therefore as a NOT port. The three-state input A3 is connected to V_{CC} by means of a pull-up resistor allowing thus the output Y3 to switch between the “Low” state (the gate is short-circuit to the ground) and the “High impedance” state (regime mode of the self-oscillating stage of the converter).

6.2.2 – Implementation of control circuit

The block diagram of the prototype of the external control circuit is shown in Figure 84.

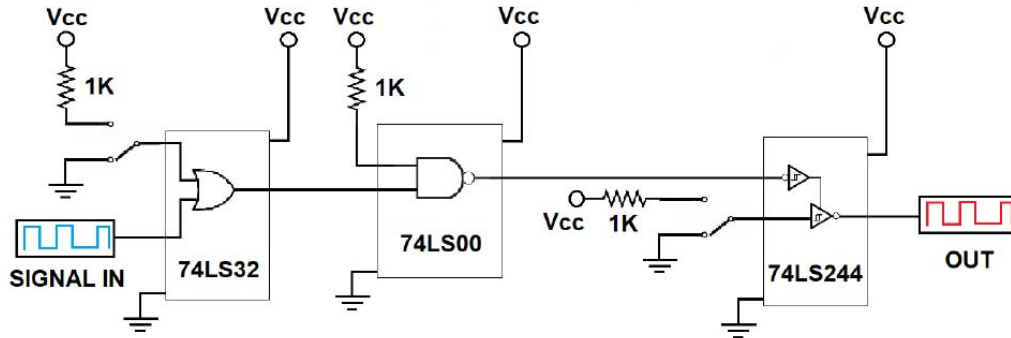


Figure 84: Block diagram of the prototype of the external control circuit [140]

Figure 85 shows its equivalent circuit.

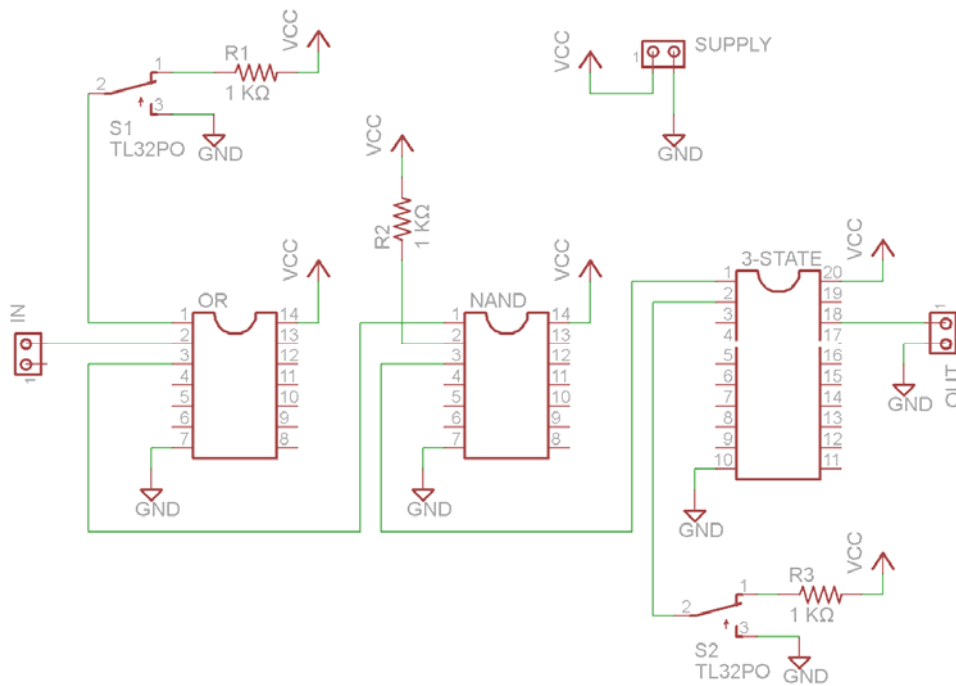


Figure 85: Equivalent circuit of the prototype of the external control circuit [140]

This circuit consists of the OR, NAND and three-state ports, two switches and two pull-up resistors. The switch SW1 is used to carry the three-state port in “High impedance” state, allowing therefore to disconnect the external circuit from the DC-DC converter. The switch SW2 allows to choose if, during the gate control, either the gate is short-circuit to the ground or the gate voltage is equal to the three-

state output voltage (High logic level). Even in the case of the external control output switches between the “High” state and the “High impedance” state, the DC-DC input current can be regulated and the value of the DC-DC input impedance can change [140].

6.2.3 – Measures

In order to validate the mode of operation of the system composed of the external control circuit and the DC-DC boost converter, several measures have been carried out. The experimental rig, shown in Figure 86, has employed a DMM4050 Digital Multimeter (Tektronix, OR, USA), a E3615A Power Supply (Hewlett-Packard, CA, USA), a MSO6104A Oscilloscope (Agilent Technologies, CA, USA), a 1582B Demo Circuit (Linear Technology Corporation, CA, USA), a PM5138 Function Generator 0.1 mHz – 10 MHz (Philips, USA) which generates the square-wave signal.

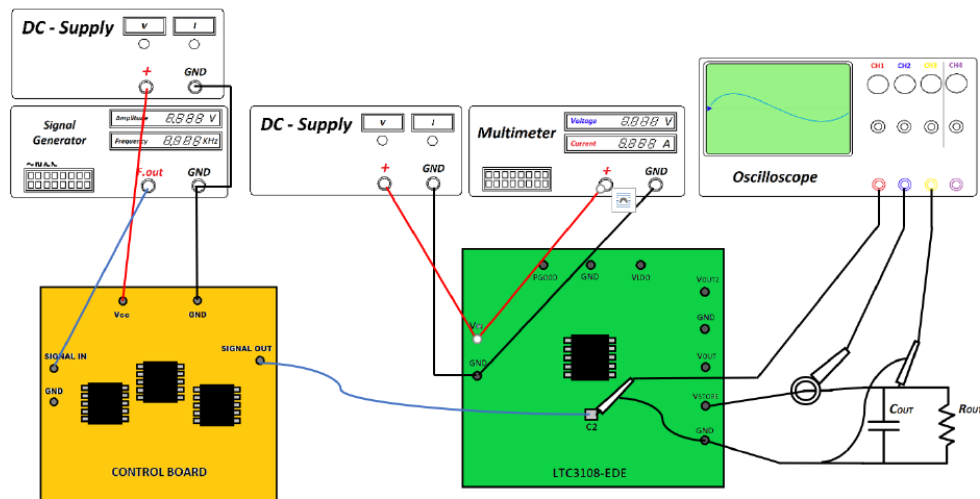
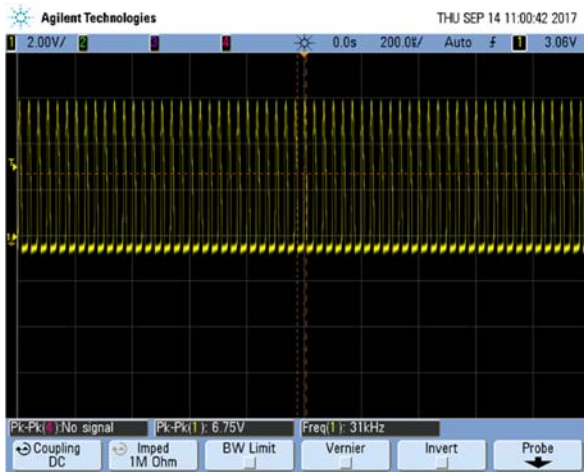
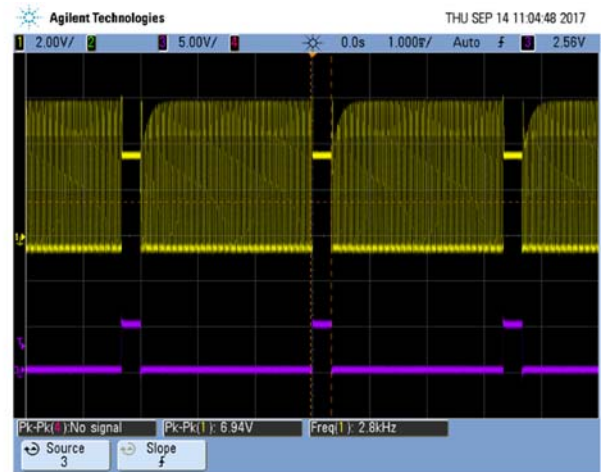


Figure 86: Experimental rig

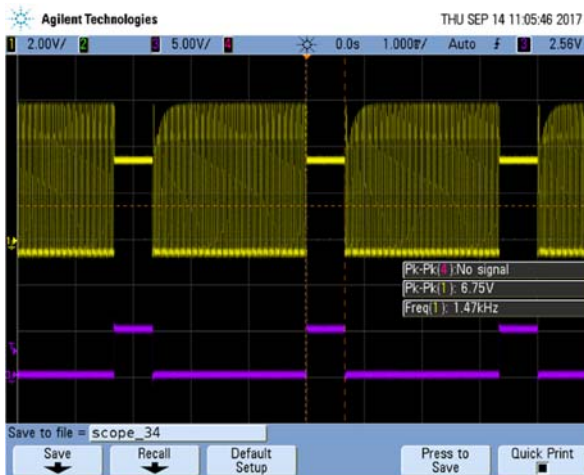
The frequency of the square-wave signal is equal to 1 kHz, much lower than the frequency of the LTC3108 self-oscillating stage equal to 44 kHz. The measures have been performed considering that the external control circuit output switches between the “High” state H and the “High impedance” state Z, following therefore the trend of the square-wave signal. Although the gate of the MOSFET is not short-circuit to the ground, the value of the DC-DC converter input impedance is modulated through the duty cycle of the square-wave signal at the input of the external control circuit. Figures 87 show the trend of the gate voltage (in yellow) and the trend of the square-wave control signal (in purple). It can be noted that during the gate control the pulse train can be cancelled.



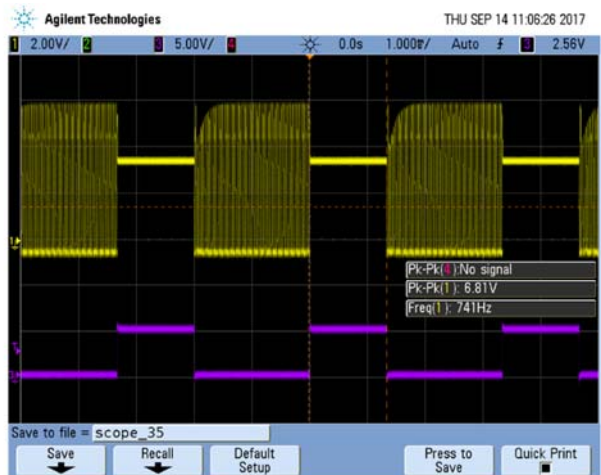
a)



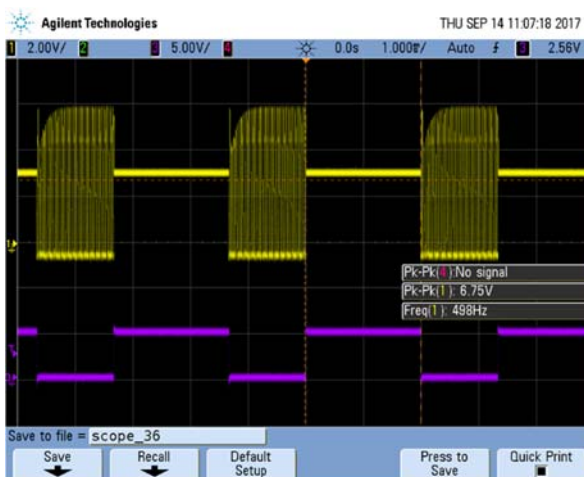
b)



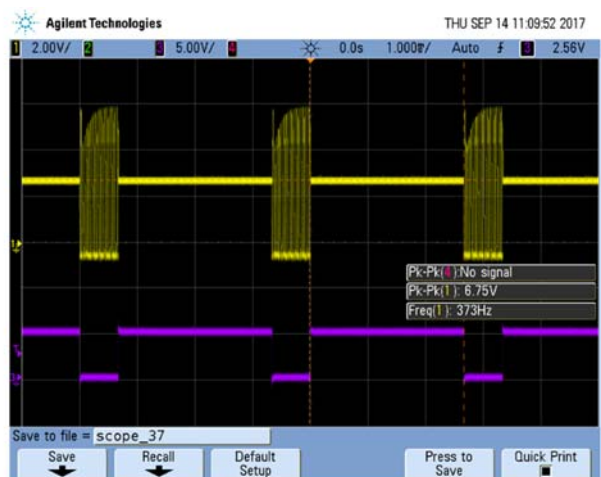
c)



d)



e)



f)

Figure 87: The trends of the gate voltage (yellow) and the square-wave duty cycle (purple) [140]

Table 19 summarizes the values of the DC-DC converter input current I_{IN} , the DC-DC converter input voltage V_{IN} and the input impedance R_{IN} .

Table 19: Input current I_{IN} , input voltage V_{IN} and input impedance R_{IN} values

D [%]	V_{IN} [mV]	I_{IN} [mA]	R_{IN} [Ω]
0	173.0	76.0	2.28
10	168.0	90.5	1.86
20	162.9	103.6	1.57
40	152.3	129.3	1.18
60	142.7	155.0	0.92
80	131.0	180.0	0.73

Figure 88 shows the curve of the DC-DC converter input impedance as a function of the square-wave duty cycle.

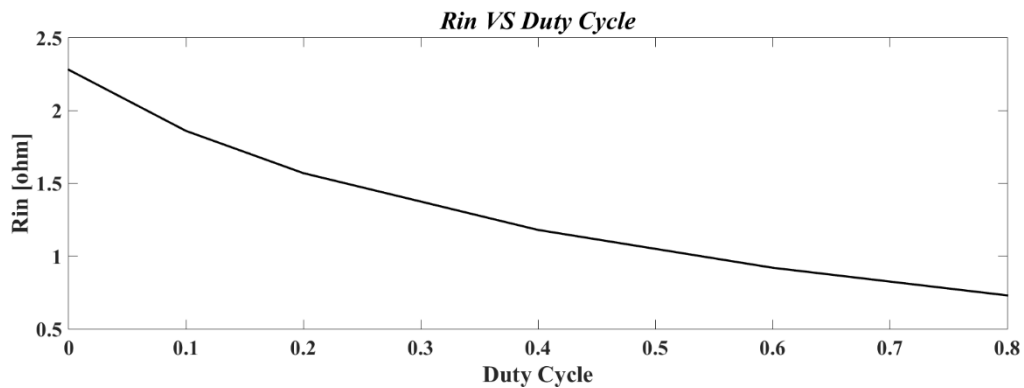


Figure 88: The DC-DC converter input impedance R_{IN} versus the square-wave duty cycle D [140]

It can be noted that in correspondence of the same variations of the duty cycle, the range of R_{IN} is greater than that obtained during the testing with only the three-state port. Choosing the switching of the external control circuit output between the “Low” state and the “High impedance” state, the range of R_{IN} is smaller; in particular, the maximum value is lower. The performed tests have demonstrated that it is possible to vary the input impedance of the commercial DC-DC boost converter such as the LTC3108 by means of the external control [140].

The block diagram of a possible typical energy harvesting system based on nanoantennas is sketched in Figure 89.

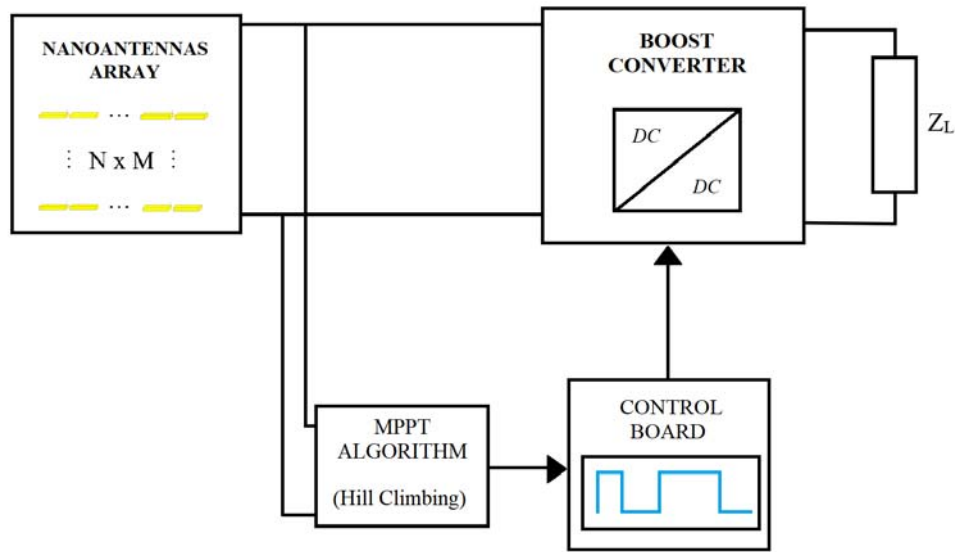


Figure 89: A block diagram of a typical energy harvesting system based on nanoantennas

This system should consist of an array of optical rectennas, a DC-DC boost converter, a load Z_L , an external control circuit and an external circuit implemented MPPT algorithms, which drives the external control circuit. The MPPT algorithm circuit should operate a sensing of the values of the output current and the output voltage of the array of optical rectennas. Furthermore, it should supply a signal proportional to the square-wave duty cycle at the output of the control circuit. A typical MPPT algorithm, usually implemented in photovoltaic cells based system, is the hill climbing. It allows to track the maximum power point in real time and to carry out an impedance matching between the source and the DC-DC converter.

6.3 – Power evaluation under mismatching conditions

The tests of the LTC3108 input impedance have demonstrated that, in correspondence of the variation of the input voltage V_{IN} , the input current I_{IN} absorbed by the LTC3108 changes. This entails that the DC-DC input impedance also changes and the impedance matching could be not satisfy. Table 9, in chapter IV, summarizes the values of V_{IN} and I_{IN} , which allow to evaluate the DC-DC converter input power. Considering the variation of the input impedance R_{IN} with respect to the optimum value R_M of 2.5Ω , it is possible to evaluate the input power as a function of the ratio between R_M and R_{IN} . Table 20 shows the values of the input voltage V_{IN} , the input current I_{IN} , the input impedance R_{IN} and the values of the input power expressed as the formula

$$P_{IN} = V_{IN} \cdot I_{IN} \quad (31)$$

Table 20: Input voltage V_{IN} , input current I_{IN} , input impedance R_{IN} and input power P_{IN}

V_{IN} [mV]	I_{IN} [mA]	R_{IN} [Ω]	P_{IN} [mW]
41.10	10.84	3.80	0.44
90.33	33.25	2.71	3.00
200.00	72.94	2.74	14.59
304.00	115.20	2.64	35.02
376.00	144.92	2.59	54.50

These values are referred to the DC-DC converter start-up phase, in which the P_{GD} signal is in “Low” state, and to the load that is the parallel between the capacitor C_{OUT} equal to 1000 μ F and the resistor R_{OUT} equal to 100 k Ω .

Figure 90 shows the curve of the input impedance R_{IN} as a function of the input voltage V_{IN} during the start-up phase.

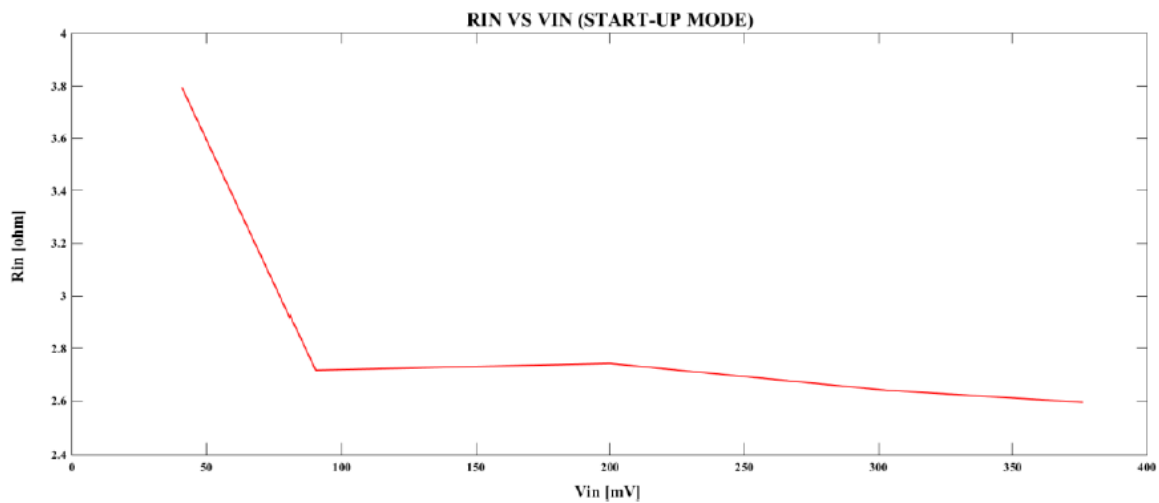


Figure 90: Input impedance R_{IN} versus input voltage V_{IN}

Figure 91, instead, shows the curve of the input power P_{IN} as a function of the values of the input impedance R_{IN} .

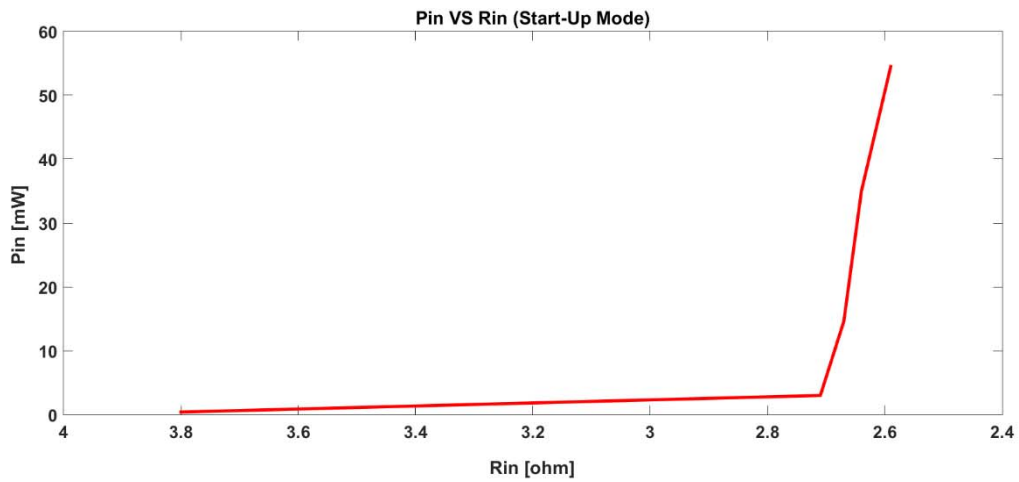


Figure 91: Input power P_{IN} versus input impedance R_{IN}

Normalizing the values of P_{IN} with respect to the maximum value of P_{IN} , $P_{MAX} = 54.50$ mW, and the values of R_{IN} with respect to the optimum value of R_{IN} , $R_M = 2.5 \Omega$, the curve shown in Figure 92 can be obtained.

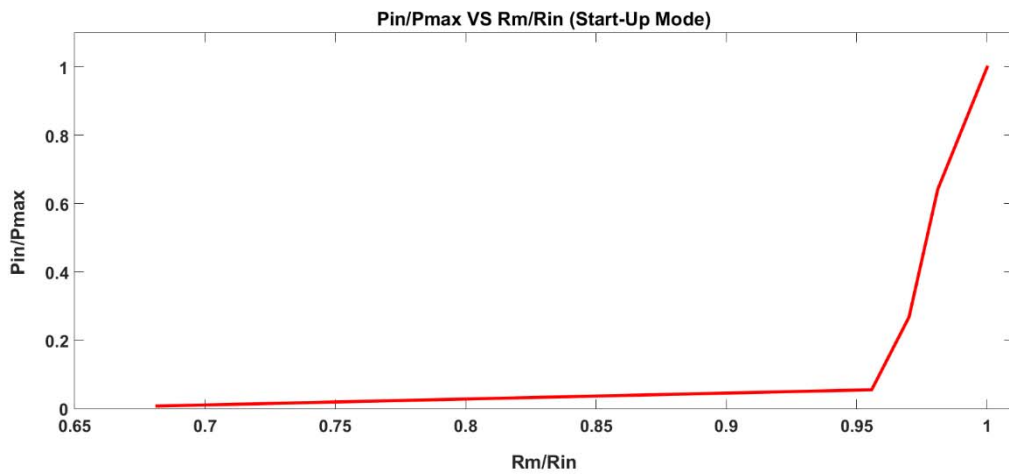


Figure 92: Normalized input power versus the ratio R_M/R_{IN}

It can be noted that the maximum value of the normalized input power decreases rapidly when the ratio R_M/R_{IN} is not equal to 1. This ratio represents a Figure of Merit (FOM) and expresses the mismatch between the DC-DC boost converter input impedance and the rectennas array output impedance. The maximum value equal to 1 represents the best impedance matching condition. Especially, from the Figure 92, it can be noted that the input power decreases of about 90 % with respect to the maximum value when the ratio R_M/R_{IN} is about of 5 %. The results confirm that to the purpose of the maximum

power transfer between the array of optical rectennas and the external load, an external control of the DC-DC converter input impedance is needed.

Conclusion

The optimization of the maximum power transfer between the array of optical rectennas and the harvesting circuit has been considered. In fact, the absence of a maximum power point tracking system in the DC-DC boost converter chosen for the purpose of this work involves that the input impedance of the converter would not be controlled immediately as the rectenna supplied voltage changes. Since the impedance matching between the DC-DC converter and the array of optical rectennas is needed in order to obtain the maximum power transfer between the harvesting system and an external load, the use of an external control is required in order to regulate the input converter impedance. At the beginnings, the external control technique has been discussed. The accessing the gate of the MOSFET allows to control the duty cycle of the LTC3108 by means of an external signal, to interrupt the switching cycle for a certain time interval, reducing thus the pulse train that turns on the switch, and to decrease the average value of the LTC3108 input current I_{IN} . The control of the MOSFET gate has to be implemented when the increase of the value of the DC-DC boost converter input impedance is needed. Otherwise, this control has not to operate and to supply the MOSFET gate, compromising in this case the normal operation mode of the converter. The short-circuit of the gate is realized connecting the external control circuit to the welding area of the capacitor C_2 . The simulations of the equivalent circuit of the self-oscillating stage of the LTC3108, performed by means of PowerSIM software, have allowed to verify the decrease of the LTC3108 input current stopping the pulse train through an external signal for a certain time interval. In order to implement the external control of the gate of the MOSFET, a logic port has to be used. At the beginnings, a NOT open collector port has been chosen. Regardless of the control signal at the input of the NOT open-collector port, once this port is connected to the capacitor C_2 , the converter output voltage begins decreasing and the pulse train at the gate becomes zero. This is because the open-collector internal resistance charges the converter self-oscillating stage even there is not signal at its input. Therefore, this type of logic port cannot implement the external control. The NOT three-state port has been thus employed. A square-wave control signal at a frequency of 1 kHz has been connected to the three-state control pin \bar{G} . The value of the control signal frequency has been chosen in order to be much lower than the switching frequency of the converter, the latter on the order of 44 kHz. When the square-wave is “High”, the three-state port is in “High impedance” state regardless of the input I_A . Otherwise, when the square-wave is “Low”, the three-state port turns on and the output I_Y becomes “Low”, i.e. equal to the ground. This means that at the C_2 pin there is a turnover of the “High impedance” state Z , which corresponds to a virtual disconnection of the external control, and of the “Low” state L , which corresponds to the short-circuit to the ground. Several tests have been performed

with the three-state port. In particular, the input current I_{IN} , the gate pulse V_{C2} , the output voltage at C_{OUT} equal to 220 μ F and the duty cycle of the square-wave have been measured. The design of the external control circuit has been then defined. The NOT three-state port is driven by an OR port. In order to obtain an external control circuit operating in positive logic, the use of another NOT port between the OR output and the three-state control pin has been needed. This allows that as the value of the duty cycle increases, the time during that the gate is controlled is longer. To this purpose, a NAND port operating as a NOT port has been implemented. A description of the implemented external control circuit has been made. This circuit consists of the OR, NAND and three-state ports, two switches and two pull-up resistors. In order to validate the mode of operation of the system composed of the external control circuit and the DC-DC boost converter, several measures has been carried out. The frequency of the square-wave signal has been set equal to 1 kHz, much lower than the frequency of the LTC3108 self-oscillating stage equal to 44 kHz. The measures have been performed considering that the external control circuit output switches between the “High” state H and the “High impedance” state Z, following therefore the trend of the square-wave signal. Although the gate of the MOSFET is not short-circuit to the ground, the value of the DC-DC converter input impedance is modulated through the duty cycle of the square-wave signal at the input of the external control circuit. Choosing the switching of the external control circuit output between the “Low” state and the “High impedance” state, the range of R_{IN} is smaller; in particular, the maximum value is lower. Therefore, the performed tests have demonstrated that it is possible to vary the input impedance of the commercial DC-DC boost converter such as the LTC3108 by means of the external control. Finally, a power evaluation under mismatching conditions has been made. In particular, the maximum value of the normalized input power decreases rapidly when the ratio between the maximum input impedance value R_M and the input impedance R_{IN} is not equal to 1. This ratio represents a Figure of Merit (FOM) and expresses the mismatch between the DC-DC boost converter input impedance and the rectennas array output impedance. The maximum value equal to 1 represents the best impedance matching condition. The input power decreases of about 90 % with respect to the maximum value when the ratio R_M/R_{IN} is about of 5 %. The results confirm that to the purpose of the maximum power transfer between the array of optical rectennas and the external load, an external control of the DC-DC converter input impedance is needed.

CONCLUSIONS AND FUTURE WORK

The novelty of this study has consisted in introducing the concept of integrated design between an array of optical rectennas and a harvesting circuit able to exploit the available energy. Especially, the main guidelines for the design of an array of optical rectennas aiming to harvest energy and the optimization of maximum power transfer to the external load has been studied and discussed. The design of the array represents a crucial point in order to optimize the power transfer between the antenna and the load and can influence the rectenna design. On the other hand, the maximum power transfer to the load has to be obtained under matching conditions between the array and the load and can influence both the design of the array and of the DC-DC boost converter. Several issues have been taken into account to study and to design the optical nanoantennas. These devices have to be able to efficiently capture the polarized incident radiation. This can be achieved using an appropriate structure. The nanoantenna structure, in particular the materials used as conductor and the dimensions of nanoantenna, also influences one of the most important nanoantenna parameter, the radiation efficiency. This is the ratio between the radiated power and the power injected at the terminals. Therefore, an accurate choice of materials and design of nanoantenna is crucial for its efficiency.

For this reason, at the beginnings, a description of the optical nanoantennas has been performed. In particular, the two main typologies of optical nanoantennas, metallic and dielectric, and their typical structures have been examined. The main techniques used for the fabrication of optical nanoantennas have then been described. They include Electron Beam Lithography and Focused Ion Beam milling that are top-down approaches requiring expensive equipment and, therefore, are not suitable for mass production, and the Nano-imprint Lithography, which is a low-cost and high-throughput alternative. On the basis of the analysis of the two main types of nanoantennas and of their main structures, the dipole nanoantenna has been chosen. It offers easy production, fine tuning, high confinement of electric field in the gap and less dissipative metal loss. The material chosen has been aluminium because it shows a reasonable efficiency values over the whole frequency band of interest. Moreover, it has a transparent oxide.

A numerical analysis of the dipole nanoantenna in order to acquire the main parameters has been thus fulfilled. This analysis has involved that the fundamental theoretical techniques widely used for the computational electromagnetics, such as Integral Equation and Differential Equations techniques, have been discussed. Several simulation tools implementing these techniques have then been overviewed. The main commercial and academic software tools are CST Microwave Studio (CST MWS), Ansoft's HFSS, FEKO, COMSOL Multiphysics, Lumerical and MAGMAS 3D. A description of the software chosen for the design of optical nanoantennas, CST Studio Suite 2016, has been made. This

electromagnetic simulation software provides a good compromise between costs and performances. The tool used for the purpose of this work has been the CST MicroWave Studio (MWS), in particular the Time Domain solver. The simulation time has been about 8-12 hours using a workstation with the following features: Intel® Core™ 15-4590 CPU @ 3.30 GHz and RAM 8 Gb. The wavelength range of interest is between 300 nm and 1200 nm, which corresponds to a frequency range of 250 THz – 1000 THz. This is the range commonly used in literature since it covers the visible and infrared interval. The simulated dipole nanoantenna consists of a width W (in z direction) and of a height H (in y direction), both equal to 40 nm. The arm length L varies in a range from 100 nm to 350 nm in steps of 50 nm. The gap G is fixed to 10 nm. The main simulation results of the dipole nanoantenna have then been summarized. In particular, the evaluation of the internal nanoantenna impedance has been detailed. The method used to evaluate the nanoantenna effective area has been described. The analysis of the main electrical parameters, i.e. the Poynting vector and the available power on the load matching conditions, has been performed.

The rectenna topology, in particular the equivalent circuit configuration, has then been analysed. This has implicated a study of the main types of the ultra-high speed rectifiers, such as MIM diode, MOM diode, geometric diode and the forest of multiwalled carbon nanotubes. The diode equivalent impedance has also been evaluated. It depends on the rectenna operation regime. The typical values of the diode resistance are in a range of 50-300 Ω for the state of art of the MIM diodes and of the order of 3 k Ω for the state of art of the geometric diode. To the purpose of this study, the diode resistance R_D has been chosen equal to 300 Ω , which represents a technological limit.

The main issues of the design of a system based on optical rectennas for energy harvesting application have been taken into account. In particular, the RC time constant of the rectifier and the impedance matching between the nanoantenna and the rectifier are two main factor that can limit the conversion efficiency of a rectenna. Another issue is tied to the available power on load matching conditions and to the output voltage of the nanoantenna, whose values are respectively on the order of few picowatt and on the order of tens microvolt. Ultralow power applications usually require the values of input voltage that are much higher than that of the nanoantenna output voltage, typically on the order of tens or hundreds of millivolt. For this reason, in order to interface an external load with a rectenna a DC-DC boost conversion system is needed. This system provides the matching with a downstream load, which harvests the output energy from the rectenna. Therefore, the main features of three type of commercially step-up DC-DC power converters for ultralow power applications, such as LTC3108, LTC3105 and SPV1050, have been taken into account. Since the most important issues for the design of an energy harvesting system based on optical nano-rectennas are the low output voltage and the low available power on the load matching conditions, the DC-DC boost converter chosen for the purpose of this work

has been the LTC3108. Several tests have been carried out in order to evaluate the LTC3108 input impedance. The values of this impedance are in a range of $2.5 \Omega - 3.8 \Omega$.

The main guidelines for the design of an array of optical dipole rectennas to harvest the energy coming from solar radiation has been defined. In particular, the optimal impedance matching between the array and the load has been investigated in order to allow the maximum power transfer. The rectennas have been arranged in a matrix of $N \times M$ optical rectennas to supply a commercial DC-DC boost converter for harvesting applications. The array equivalent impedance has to be equal to the harvesting circuit input impedance. The choice of the values of N and of M depends on the DC-DC boost converter downstream to the array. In particular, N depends on the output voltage to be supplied to the DC-DC converter, whereas M depends on the DC-DC converter input resistance. The order of magnitude of the number of rectennas in an array of optical rectennas coupled to the commercial DC-DC boost converter is about 10^{12} . A Figure of Merit as the ratio between the array effective area and the array geometric area has also been defined, which is as better as the dipole arm length is lower. The best results have been obtained by the 150 nm dipole since it exhibits the highest value of the single rectenna output voltage and consequently the lowest area in terms of $N \times M$ matrix. In addition, the same dipole has a good ratio effective area over geometric area. For this reason, the evaluation of the delivered energy has been performed considering this kind of dipole. The energy produced in a July sunny day has then been calculated. This energy is able to charge a supercapacitor of about 150 F with voltage equal to 5 V. The curve of the available power on the DC-DC boost converter P_{load} as a function of the diode resistance R_D for a 150 nm arm length dipole has been calculated. In particular, the value of the diode resistance R_D has been varied in a range from 50Ω to 3000Ω in steps of 10Ω . It can be noted that when the value of R_D increases, the power on the boost decreases and tends towards a saturation value. The analysis performed represents a worst case scenario since the range of interest for the collected radiation has been limited to 300 nm and 1200 nm, equivalent to a frequency range of $250 \text{ THz} \div 1000 \text{ THz}$ and the rectifying diode impedance has been assumed to be equal to the best value allowed by the actual technology. Despite these limitations, the designed matrix of rectennas appears very promising for energy harvesting purposes.

The output equivalent impedance of the array of optical rectennas usually changes with the solar radiation during a day. The absence of a maximum power point tracking system in the DC-DC boost converter chosen for the purpose of this work involves that the input impedance of the converter would not be controlled immediately as the rectenna supplied voltage changes. Since the impedance matching between the DC-DC converter and the array of optical rectennas is needed in order to obtain the maximum power transfer between the harvesting system and an external load, the use of an external control is required in order to regulate the input converter impedance. The external control allows to control the duty cycle of the LTC3108 by means of an external square-wave signal, to interrupt the

switching cycle for a certain time interval, reducing thus the pulse train that turns on the switch, and to decrease the average value of the LTC3108 input current. Moreover, the external control of the gate of the MOSFET has to be implemented when the change of the value of the DC-DC boost converter input impedance is needed. Otherwise, this control has not to operate and to supply the gate of the MOSFET, compromising thus the normal operation mode of the converter. The control of the gate has been realized connecting the external control circuit to the welding area of the capacitor C_2 . A description of the implemented external control circuit has then been performed. This circuit consists of a NOT three-state port driven by an OR port, a NAND port in order to obtain an external control circuit operating in positive logic and two switches. The value of the control signal frequency has been chosen equal to 1 kHz, much lower than the frequency of the LTC3108, equal to 44 kHz. In order to validate the mode of operation of the system composed of the external control circuit and the DC-DC boost converter, several tests have been carried out. These measures have been performed considering that the external control circuit switches between the “High” state and the “High impedance” state, following therefore the trend of the square-wave control signal. The results have confirmed that it is possible to vary the input impedance of the commercial DC-DC boost converter, such as the LTC3108, by means of an appropriate external control. This allow to optimize the maximum power transfer to an external load. Finally, a power evaluation under mismatching conditions has been performed, confirming that to the purpose of the maximum power transfer to an external load, the impedance matching conditions between the array of optical rectennas and the harvesting circuit are needed.

A typical energy harvesting system based on nanoantennas should consist of an array of optical rectennas, a DC-DC boost converter, an external load, an external impedance control circuit and an external circuit implemented MPPT algorithms, which drives the external impedance control circuit. The MPPT algorithm circuit should operate a sensing of the values of the output current and of the output voltage of the array. Furthermore, it should supply a signal proportional to the square-wave duty cycle at the output of the control circuit. In this way, the impedance matching conditions would be constantly verified. The available energy on the load matching conditions would allow to charge a supercapacitor whose is equal to 5 V and whose capacitor is equal to about 157 F. On the other hand, the numerical analysis of the array of nanodipole would allow to verify if the dipoles interfere each other. This would improve the design of the array and would influence the choice of the DC-DC boost converter and the design of the external impedance control circuit. Last but not least, the values of the diode resistance and the diode capacitance represent a technological limit. Therefore, further studies should be performed in order to improve the rectification in the range of terahertz.

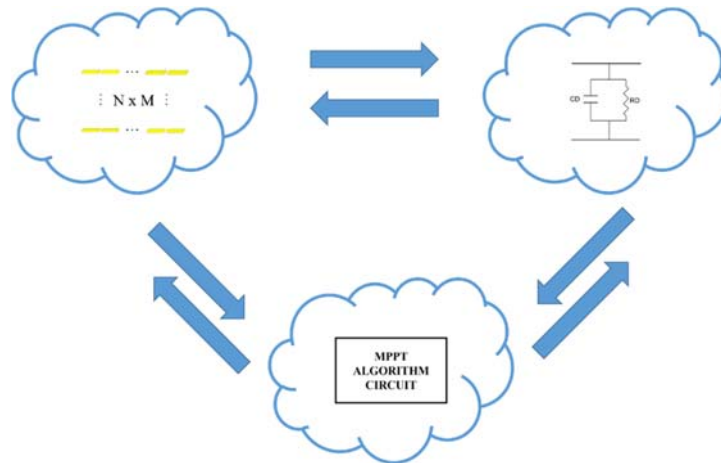


Figure 93: Example of integrated design

Despite the big potentiality of the energy harvesting system based on nanoantennas analysed in this study, several improvements could be performed. To this purpose, the integrated design between an array of optical rectennas and a harvesting circuit able to exploit the available energy seems to be very promising.

REFERENCES

- [1] Steil, M. C., Nobrega, S. D., Georges, S., Gelin, P., Uhlenbruck, S., & Fonseca, F. C. (2017). Durable direct ethanol anode-supported solid oxide fuel cell. *Applied Energy*, 199, 180-186.
- [2] Zhang, Z., Liu, C., Liu, W., Cui, Y., Du, X., Xu, D., ... & Deng, Y. (2017). Innovative design of coal utilization—A green pathway for direct conversion of coal to electricity through flow fuel cell technology. *Applied Energy*, 200, 226-236.
- [3] Bizon, N. (2013). Energy harvesting from the FC stack that operates using the MPP tracking based on modified extremum seeking control. *Applied energy*, 104, 326-336.
- [4] Orrego, S., Shoele, K., Ruas, A., Doran, K., Caggiano, B., Mittal, R., & Kang, S. H. (2017). Harvesting ambient wind energy with an inverted piezoelectric flag. *Applied Energy*, 194, 212-222.
- [5] Wang, X. (2012). Piezoelectric nanogenerators—Harvesting ambient mechanical energy at the nanometer scale. *Nano Energy*, 1(1), 13-24.
- [6] Jung, I., Shin, Y. H., Kim, S., Choi, J. Y., & Kang, C. Y. (2017). Flexible piezoelectric polymer-based energy harvesting system for roadway applications. *Applied Energy*, 197, 222-229.
- [7] Xiong, H., & Wang, L. (2016). Piezoelectric energy harvester for public roadway: On-site installation and evaluation. *Applied Energy*, 174, 101-107.
- [8] Sebal, G., Guyomar, D., & Agbossou, A. (2009). On thermoelectric and pyroelectric energy harvesting. *Smart Materials and Structures*, 18(12), 125006.
- [9] Lu, Z., Zhang, H., Mao, C., & Li, C. M. (2016). Silk fabric-based wearable thermoelectric generator for energy harvesting from the human body. *Applied Energy*, 164, 57-63.
- [10] Kim, M. K., Kim, M. S., Lee, S., Kim, C., & Kim, Y. J. (2014). Wearable thermoelectric generator for harvesting human body heat energy. *Smart Materials and Structures*, 23(10), 105002.
- [11] Konishi, R., & Takahashi, M. (2017). Optimal Allocation of Photovoltaic Systems and Energy Storage Systems based on Vulnerability Analysis. *Energies*, 10(10), 1477.
- [12] Tobón, A., Peláez-Restrepo, J., Villegas-Ceballos, J., Serna-Garcés, S. I., Herrera, J., & Ibeas, A. (2017). Maximum Power Point Tracking of Photovoltaic Panels by Using Improved Pattern Search Methods. *Energies*, 10(9), 1316.
- [13] Morón, C., Ferrández, D., Saiz, P., Vega, G., & Díaz, J. P. (2017). New Prototype of Photovoltaic Solar Tracker Based on Arduino. *Energies*, 10(9), 1298.
- [14] Mughal, M. A., Ma, Q., & Xiao, C. (2017). Photovoltaic Cell Parameter Estimation Using Hybrid Particle Swarm Optimization and Simulated Annealing. *Energies*, 10(8), 1213.

- [15]Gouvêa, E. C., Sobrinho, P. M., & Souza, T. M. (2017). Spectral Response of Polycrystalline Silicon Photovoltaic Cells under Real-Use Conditions. *Energies*, 10(8), 1178.
- [16]Itten, R., & Stucki, M. (2017). Highly Efficient 3rd Generation Multi-Junction Solar Cells Using Silicon Heterojunction and Perovskite Tandem: Prospective Life Cycle Environmental Impacts. *Energies*, 10(7), 841.
- [17]Aiello, G., Alfonzetti, S., Rizzo, S. A., & Salerno, N. (2017). Multi-Objective Optimization of Thin-Film Silicon Solar Cells with Metallic and Dielectric Nanoparticles. *Energies*, 10(1), 53.
- [18]Yun, J. H., Wang, L., Amal, R., & Ng, Y. H. (2016). One-Dimensional TiO₂ Nanostructured Photoanodes: From Dye-Sensitised Solar Cells to Perovskite Solar Cells. *Energies*, 9(12), 1030.
- [19]Elumalai, N. K., Mahmud, M. A., Wang, D., & Uddin, A. (2016). Perovskite Solar Cells: Progress and Advancements. *Energies*, 9(11), 861.
- [20]Peng, Y., Zhang, L., Cheng, N., & Andrew, T. L. (2017). ITO-Free Transparent Organic Solar Cell with Distributed Bragg Reflector for Solar Harvesting Windows. *Energies*, 10(5), 707.
- [21]Di Piazza, M. C., & Vitale, G. (2013). *Photovoltaic sources: modelling and emulation*. Springer Science & Business Media, ISBN: ISSN 1865-3529 ISSN 1865-3537, DOI 10.1007/978-1-4471-4378-9.
- [22]Wentham, S., Green M. A., Watt M. E., Corkish R. (2009). *Applied photovoltaics*. Earthscan.
- [23]Goetzberger, A., & Hoffmann, V. U. (2005). *Photovoltaic solar energy generation (Vol. 112)*. Springer Science & Business Media.
- [24]Mescia, L., & Massaro, A. (2014). New trends in energy harvesting from earth long-wave infrared emission. *Advances in Materials Science and Engineering*, 2014.
- [25]Mescia, L., Bia, P., & Losito, O. (2015). Earth Long-Wave Infrared Emission, New Ways to Harvest Energy. In *Innovative Materials and Systems for Energy Harvesting Applications* (pp. 1-25). IGI Global.
- [26]Biagioni, P., Huang, J. S., & Hecht, B. (2012). Nanoantennas for visible and infrared radiation. *Reports on Progress in Physics*, 75(2), 024402.
- [27]Krasnok, A. E., Maksymov, I. S., Denisyuk, A. I., Belov, P. A., Miroshnichenko, A. E., Simovski, C. R., & Kivshar, Y. S. (2013). Optical nanoantennas. *Physics-Uspekhi*, 56(6), 539.
- [28]Di Piazza, M. C., Pucci, M., Ragusa, A., & Vitale, G. (2008, November). Fuzzified PI voltage control for boost converters in multi-string PV plants. In *Industrial Electronics, 2008. IECON 2008. 34th Annual Conference of IEEE* (pp. 2338-2345). IEEE.
- [29]Marian, V., Allard, B., Vollaïre, C., & Verdier, J. (2012). Strategy for microwave energy harvesting from ambient field or a feeding source. *IEEE Transactions on Power Electronics*, 27(11), 4481-4491.
- [30]Novotny, L., & Van Hulst, N. (2011). Antennas for light. *Nature photonics*, 5(2), 83-90.

- [31]Giannini, V., Fernández-Domínguez, A. I., Heck, S. C., & Maier, S. A. (2011). Plasmonic nanoantennas: fundamentals and their use in controlling the radiative properties of nanoemitters. *Chemical reviews*, 111(6), 3888-3912.
- [32]Zhu, Z., Joshi, S., Pelz, B., & Moddel, G. (2013, September). Overview of optical rectennas for solar energy harvesting. In *Proc. of SPIE Vol (Vol. 8824, pp. 88240O-1)*.
- [33]Moddel, G. (2013). Will rectenna solar cells be practical?. In *Rectenna Solar Cells* (pp. 3-24). Springer New York.
- [34]Sadashivappa, G., & Sharvari, N. P. (2015). Nanoantenna—a review. *International journal of Renewable Energy Tecnology Research*, 4(1), 1-9.
- [35]Sabaawi, A. M., Tsimenidis, C. C., & Sharif, B. S. (2013). Overview of nanoantennas for solar rectennas. In *Rectenna Solar Cells* (pp. 231-256). Springer New York.
- [36]Brown, W. C. (1968). The combination receiving antenna and rectifier. *Microwave Power Engineering*, 2, 273-275.
- [37]Brown, W. C. (1984). The history of power transmission by radio waves. *IEEE Transactions on microwave theory and techniques*, 32(9), 1230-1242.
- [38]Bailey, R. L. (1972). A proposed new concept for a solar-energy converter. *Journal of Engineering for Power*, 94(2), 73-77. DOI: 10.1115/1.3445660.
- [39]Marks, A. M. (1984). Device for conversion of light power to electrical power. U.S. Patent No. 4,445,050. Washington, DC: U.S. Patent and Trademark Office.
- [40]Wijewardane, S., & Goswami, Y. (2014). Extended exergy concept to facilitate designing and optimization of frequency-dependent direct energy conversion systems. *Applied Energy*, 134, 204-214.
- [41]Di Garbo, C., Livreri, P., & Vitale, G. (2016, May). Solar Nanoantennas energy based characterization. In *International Conference on Renewable Energies and Power Quality (ICREPQ)*, Madrid (pp. 4-6).
- [42]Chekini, A., Sheikhaei, S., & Neshat, M. (2016, December). A novel plasmonic nanoantenna structure for solar energy harvesting. In *Millimeter-Wave and Terahertz Technologies (MMWaTT), 2016 Fourth International Conference on* (pp. 20-24). IEEE.
- [43]Di Garbo, C., Livreri, P., & Vitale, G. (2017, June). Optimal matching between optical rectennas and harvester circuits. In *Environment and Electrical Engineering and 2017 IEEE Industrial and Commercial Power Systems Europe (EEEIC/I&CPS Europe), 2017 IEEE International Conference on* (pp. 1-6). IEEE.
- [44]Abadal, G., Alda, J., & Agustí, J. (2014). Electromagnetic radiation energy harvesting—The rectenna based approach. In *ICT-Energy-Concepts Towards Zero-Power Information and Communication Technology*. InTech.

- [45]Javan A. (October 1971). Laser measures light-wave frequency. *IEEE Spectrum* 1971 (pp. 91).
- [46]Heiblum, M., Wang, S., Whinnery, J., & Gustafson, T. (1978). Characteristics of integrated MOM junctions at dc and at optical frequencies. *IEEE Journal of Quantum Electronics*, 14(3), 159-169.
- [47]Lin, G. H., Abdu, R., & Bockris, J. O. M. (1996). Investigation of resonance light absorption and rectification by subnanostructures. *Journal of applied physics*, 80(1), 565-568.
- [48]Kottmann, J. P., Martin, O. J. F., Smith, D. R., & Schultz, S. (2001). Non-regularly shaped plasmon resonant nanoparticle as localized light source for near-field microscopy. *Journal of microscopy*, 202(1), 60-65.
- [49]Berland, B. (2003). *Photovoltaic Technologies Beyond the Horizon: Optical Rectenna Solar Cell*, Final Report, 1 August 2001-30 September 2002 (No. NREL/SR-520-33263). National Renewable Energy Lab., Golden, CO.(US).
- [50]Sundaramurthy, A., Crozier, K. B., Kino, G. S., Fromm, D. P., Schuck, P. J., & Moerner, W. E. (2005). Field enhancement and gap-dependent resonance in a system of two opposing tip-to-tip Au nanotriangles. *Physical Review B*, 72(16), 165409.
- [51]McMahon, J. M., Henry, A. I., Wustholz, K. L., Natan, M. J., Freeman, R. G., Van Duyne, R. P., & Schatz, G. C. (2009). Gold nanoparticle dimer plasmonics: finite element method calculations of the electromagnetic enhancement to surface-enhanced Raman spectroscopy. *Analytical and bioanalytical chemistry*, 394(7), 1819-1825.
- [52]McMahon, J. M., Gray, S. K., & Schatz, G. C. (2010). Optical properties of nanowire dimers with a spatially nonlocal dielectric function. *Nano letters*, 10(9), 3473-3481.
- [53]Kotter, D. K., Novack, S. D., Slafer, W. D., & Pinhero, P. J. (2010). Theory and manufacturing processes of solar nanoantenna electromagnetic collectors. *Journal of Solar Energy Engineering*, 132(1), 011014.
- [54]Midrio, M., Romagnoli, M., Boscolo, S., De Angelis, C., Locatelli, A., Modotto, D., & Capobianco, A. D. (2011). Flared Monopole Antennas for 10 μm Radiation. *IEEE Journal of Quantum Electronics*, 47(1), 84-91.
- [55]Chen, H., Xi, N., Lai, K. W. C., Chen, L., Fung, C. K. M., & Lou, J. (2012). Plasmonic-resonant bowtie antenna for carbon nanotube photodetectors. *International Journal of Optics*, 2012.
- [56]Vandenbosch, G. A., & Ma, Z. (2012). Upper bounds for the solar energy harvesting efficiency of nano-antennas. *Nano Energy*, 1(3), 494-502.
- [57]Gadalla, M. N., Abdel-Rahman, M., & Shamim, A. (2014). Design, optimization and fabrication of a 28.3 THz nano-rectenna for infrared detection and rectification. *Scientific reports*, 4.
- [58]Sharma, A., Singh, V., Bougher, T. L., & Cola, B. A. (2015). A carbon nanotube optical rectenna. *Nature nanotechnology*, 10(12), 1027-1032.

- [59]Obayya, S., Areeed, N. F. F., Hameed, M. F. O., & Hussein, M. (2015). Optical nano-antennas for energy harvesting. In *Innovative Materials and Systems for Energy Harvesting Applications* (p. 26). IGI Global.
- [60]Stokes, J. L., Yu, Y., Yuan, Z. H., Pugh, J. R., Lopez-Garcia, M., Ahmad, N., & Cryan, M. J. (2014). Analysis and design of a cross dipole nanoantenna for fluorescence-sensing applications. *JOSA B*, 31(2), 302-310.
- [61]Huang, J. S., Feichtner, T., Biagioni, P., & Hecht, B. (2009). Impedance matching and emission properties of nanoantennas in an optical nanocircuit. *Nano Letters*, 9(5), 1897-1902.
- [62]Alù, A., & Engheta, N. (2008). Hertzian plasmonic nanodimer as an efficient optical nanoantenna. *Physical Review B*, 78(19), 195111.
- [63]Abbas, A., El-Said, M., & Mahmoud, S. F. (2013, August). Characteristics of an Optical Bowtie Nanoantenna. In *PIERS Proceedings*.
- [64]Liaw, J. W. (2008). Analysis of a bowtie nanoantenna for the enhancement of spontaneous emission. *IEEE Journal of Selected Topics in Quantum Electronics*, 14(6), 1441-1447.
- [65]Wang, Q., Liu, L., Wang, Y., Liu, P., Jiang, H., Xu, Z., ... & Dong, L. (2015). Tunable Optical Nanoantennas Incorporating Bowtie Nanoantenna Arrays with Stimuli-Responsive Polymer. *Scientific reports*, 5.
- [66]Li, Z., Hattori, H. T., & Franco, M. A. (2013, August). Spiral broadband plasmonic nano-antennas. In *Microwave & Optoelectronics Conference (IMOC), 2013 SBMO/IEEE MTT-S International* (pp. 1-5). IEEE.
- [67]Sabaawi, A. M., Tsimenidis, C. C., & Sharif, B. S. (2012, November). Infra-red spiral nano-antennas. In *Antennas and Propagation Conference (LAPC), 2012 Loughborough* (pp. 1-4). IEEE.
- [68]Gallo, M., Mescia, L., Losito, O., Bozzetti, M., & Prudeniano, F. (2012). Design of optical antenna for solar energy collection. *Energy*, 39(1), 27-32.
- [69]Bozzetti, M., De Candia, G., Gallo, M., Losito, O., Mescia, L., & Prudeniano, F. (2010, July). Analysis and design of a solar rectenna. In *Industrial Electronics (ISIE), 2010 IEEE International Symposium on* (pp. 2001-2004). IEEE.
- [70]Thomas, D. R., Kuppusamy, P. G., Gopal, B. G., & Kumar, V. S. Design of Nano Square Spiral Antenna in Terahertz Region for Solar Energy Harvesting.
- [71]Maksymov, I. S., Staude, I., Miroshnichenko, A. E., & Kivshar, Y. S. (2012). Optical yagi-uda nanoantennas. *Nanophotonics*, 1(1), 65-81.
- [72]Krasnok, A. E., Belov, P. A., Miroshnichenko, A. E., Kuznetsov, A. I., Luk'yanchuk, B. S. & Kivshar, Y. S. (2014). All-dielectric optical nanoantennas. *Progress in compact antennas*, pp. 143-175, Intech.

- [73]Huang, J. S., Callegari, V., Geisler, P., Brünig, C., Kern, J., Prangma, J. C., ... & Kamp, M. (2010). Atomically flat single-crystalline gold nanostructures for plasmonic nanocircuitry. *Nature communications*, 1, 150.
- [74]Roxworthy, B. J., Bhuiya, A. M., Yu, X., Chow, E. K., & Toussaint Jr, K. C. (2014). Reconfigurable nanoantennas using electron-beam manipulation. *Nature communications*, 5.
- [75]Lv, J. T., Yan, Y., Zhang, W. K., Liu, Y. H., Jiang, Z. Y., & Si, G. Y. (2015). Plasmonic nanoantennae fabricated by focused Ion beam milling. *International Journal of Precision Engineering and Manufacturing*, 16(4), 851-855.
- [76]Guo, L. J. (2007). Nanoimprint lithography: methods and material requirements. *Advanced materials*, 19(4), 495-513.
- [77]Boltasseva, A. (2009). Plasmonic components fabrication via nanoimprint. *Journal of Optics A: Pure and Applied Optics*, 11(11), 114001.
- [78]Vandenbosch, G. A., & Vasylenko, A. (2011). A practical guide to 3D electromagnetic software tools. In *Microstrip Antennas*. InTech.
- [79]Smajic, J., Hafner, C., Raguin, L., Tavzarashvili, K., & Mishrikey, M. (2009). Comparison of numerical methods for the analysis of plasmonic structures. *Journal of Computational and Theoretical Nanoscience*, 6(3), 763-774.
- [80]Hoffmann, J., Hafner, C., Leidenberger, P., Hesselbarth, J., & Burger, S. (2009). Comparison of electromagnetic field solvers for the 3D analysis of plasmonic nano antennas. *arXiv preprint arXiv:0907.3570*.
- [81]Vandenbosch, G. A., Volski, V., Verellen, N., & Moshchalkov, V. V. (2011). On the use of the method of moments in plasmonic applications. *Radio Science*, 46(5).
- [82]www.cst.com
- [83]Ma, Z., & Vandenbosch, G. A. (2013). Optimal solar energy harvesting efficiency of nano-rectenna systems. *Solar Energy*, 88, 163-174.
- [84]Ma, Z., & Vandenbosch, G. A. (2013, April). Input impedance of optical metallic nano dipole over 300 nm–1200 nm wavelength. In *Antennas and Propagation (EuCAP), 2013 7th European Conference on* (pp. 3810-3813). IEEE.
- [85]Xu, Y., Tucker, E., Boreman, G., Raschke, M. B., & Lail, B. A. (2016). Optical nanoantenna input impedance. *ACS Photonics*, 3(5), 881-885.
- [86]Alu, A., & Engheta, N. (2008). Input impedance, nanocircuit loading, and radiation tuning of optical nanoantennas. *Physical review letters*, 101(4), 043901.
- [87]El-Toukhy, Y. M., Hussein, M., Hameed, M. F. O., Heikal, A. M., Abd-Elrazzak, M. M., & Obayya, S. S. A. (2016). Optimized tapered dipole nanoantenna as efficient energy harvester. *Optics express*, 24(14), A1107-A1122.

- [88]Di Garbo, C., Di Liberto, G., Livreri, P., & Vitale, G. (2017). Optimal design issues of optical dipole rectennas array for energy harvesting application. *Applied Energy*. (In submission)
- [89]Di Garbo, C., Livreri, P., & Vitale, G. (2017). Design and optimization of an array of optical rectennas for solar energy harvesting. *Energies*. (In submission)
- [90]Olmon, R. L., & Raschke, M. B. (2012). Antenna-load interactions at optical frequencies: impedance matching to quantum systems. *Nanotechnology*, 23(44), 444001.
- [91]Di Garbo, C., Livreri, P., & Vitale, G. (2016, July). Review of Infrared Nanoantennas for Energy Harvesting. In *International Conference on Modern Electrical Power Engineering (ICMEPE)*, Accepted for Las Palmas (pp. 6-8).
- [92]Di Garbo, C., Livreri, P., & Vitale, G. (2016). Optical Nanoantennas for Energy Harvesting. 48th Annual Meeting of the Associazione Gruppo Italiano di Elettronica (GE).
- [93]Grover, S., & Moddel, G. (2011). Applicability of metal/insulator/metal (MIM) diodes to solar rectennas. *IEEE Journal of Photovoltaics*, 1(1), 78-83.
- [94]Sabaawi, A. M., Tsimenidis, C. C., & Sharif, B. S. (2013). Analysis and modeling of infrared solar rectennas. *IEEE Journal of Selected Topics in Quantum Electronics*, 19(3), 9000208-9000208.
- [95]Donchev, E., Pang, J. S., Gammon, P. M., Centeno, A., Xie, F., Petrov, P. K., ... & Alford, N. M. (2014). The rectenna device: From theory to practice (a review). *MRS Energy & Sustainability-A Review Journal*, 1.
- [96]Grover, S., & Moddel, G. (2013). Metal single-insulator and multi-insulator diodes for rectenna solar cells. In *Rectenna Solar Cells*(pp. 89-109). Springer New York.
- [97]Sanchez, A., Davis Jr, C. F., Liu, K. C., & Javan, A. (1978). The MOM tunneling diode: Theoretical estimate of its performance at microwave and infrared frequencies. *Journal of Applied Physics*, 49(10), 5270-5277.
- [98]Aldrigo, M., Masotti, D., Costanzo, A., & Rizzoli, V. (2013, May). Numerical analysis of an innovative energy-harvesting system in the infrared region. In *Wireless Power Transfer (WPT)*, 2013 IEEE (pp. 123-126). IEEE.
- [99]Tiwari, B. N., Krenz, P. M., Szakmany, G. P., Bernstein, G. H., Orlov, A. O., & Prood, W. (2013). Investigation of the Infrared Radiation Detection Mechanism for Antenna-Coupled Metal-(Oxide)-Metal Structures. In *Rectenna Solar Cells* (pp. 189-208). Springer New York.
- [100] Zhu, Z., Joshi, S., Grover, S., & Moddel, G. (2013). Graphene geometric diodes for terahertz rectennas. *Journal of Physics D: Applied Physics*, 46(18), 185101.
- [101] Zhu, Z., Joshi, S., Grover, S., & Moddel, G. (2013). Geometric diodes for optical rectennas. In *Rectenna Solar Cells* (pp. 209-227). Springer New York.

- [102] Zhu, Z., Joshi, S., Pelz, B., & Moddel, G. (2016). Graphene Geometric Diodes and Antennas for Terahertz Applications. In *Graphene Science Handbook: Electrical and Optical Properties* (pp. 543-552). CRC Press.
- [103] Moddel, G. (2015). Optical rectennas: nanotubes circumvent trade-offs. *Nature nanotechnology*, 10(12), 1009-1010.
- [104] Grover, S., Dmitriyeva, O., Estes, M. J., & Moddel, G. (2010). Traveling-wave metal/insulator/metal diodes for improved infrared bandwidth and efficiency of antenna-coupled rectifiers. *IEEE Transactions on Nanotechnology*, 9(6), 716-722.
- [105] Hashem, I. E., Rafat, N. H., & Soliman, E. A. (2014). Dipole nantennas terminated by traveling wave rectifiers for ambient thermal energy harvesting. *IEEE Transactions on Nanotechnology*, 13(4), 767-778.
- [106] Sayed, I. E. H., Rafat, N. H., & Soliman, E. A. (2015, May). Harvesting thermal infrared emission using nanodipole terminated by traveling wave rectifier. In *Antennas and Propagation (EuCAP), 2015 9th European Conference on* (pp. 1-5). IEEE.
- [107] Pelz, B., Belkadi, A., & Moddel, G. (2016, June). Traveling-wave metal-insulator-metal diodes for infrared rectennas. In *Photovoltaic Specialists Conference (PVSC), 2016 IEEE 43rd*(pp. 1034-1038). IEEE.
- [108] Joshi, S., Zhu, Z., Grover, S., & Moddel, G. (2012, June). Infrared optical response of geometric diode rectenna solar cells. In *Photovoltaic Specialists Conference (PVSC), 2012 38th IEEE*(pp. 002976-002978). IEEE.
- [109] Masotti, D., Costanzo, A., Aldrigo, M., & Dragoman, M. (2014). Graphene-based nano-rectennain the far infrared frequency band. In *European Microwave Conference Proceedings*.
- [110] Zhu, Z., Joshi, S., & Moddel, G. (2014). High performance room temperature rectenna IR detectors using graphene geometric diodes. *IEEE Journal of Selected Topics in Quantum Electronics*, 20(6), 70-78.
- [111] Grover, S., & Moddel, G. (2013). Optical frequency rectification. In *Rectenna Solar Cells* (pp. 25-46). Springer New York.
- [112] Grover, S., Joshi, S., & Moddel, G. (2013). Quantum theory of operation for rectenna solar cells. *Journal of Physics D: Applied Physics*, 46(13), 135106.
- [113] Joshi, S., & Moddel, G. (2016). Optical rectenna operation: where Maxwell meets Einstein. *Journal of Physics D: Applied Physics*, 49(26), 265602.
- [114] Joshi, S., & Moddel, G. (2015). Rectennas at optical frequencies: How to analyze the response. *Journal of Applied Physics*, 118(8), 084503.
- [115] Joshi, S., & Moddel, G. (2013). Efficiency limits of rectenna solar cells: Theory of broadband photon-assisted tunneling. *Applied Physics Letters*, 102(8), 083901.

- [116] Joshi, S., Grover, S., & Moddel, G. (2013). Efficiency limits for solar spectrum rectification. In *Rectenna Solar Cells* (pp. 47-67). Springer New York.
- [117] Joshi, S., & Moddel, G. (2016). Simple Figure of Merit for Diodes in Optical Rectennas. *IEEE Journal of Photovoltaics*, 6(3), 668-672.
- [118] Gadalla, M. N., & Shamim, A. (2014, October). 28.3 THz bowtie antenna integrated rectifier for infrared energy harvesting. In *Microwave Conference (EuMC), 2014 44th European* (pp. 652-655). IEEE.
- [119] Wang, K., Hu, H., Lu, S., Guo, L., & He, T. (2015). Design of a sector bowtie nano-rectenna for optical power and infrared detection. *Frontiers of Physics*, 10(5), 104101.
- [120] Szakmany, G. P., Krenz, P. M., Orlov, A. O., Bernstein, G. H., & Porod, W. (2013). Antenna-coupled nanowire thermocouples for infrared detection. *IEEE Transactions on Nanotechnology*, 12(2), 163-167.
- [121] Szakmany, G. P., Orlov, A. O., Bernstein, G. H., Porod, W., Bareiss, M., Lugli, P., ... & Nossek, J. A. (2014, March). Nano-antenna arrays for the infrared regime. In *Smart Antennas (WSA), 2014 18th International ITG Workshop on* (pp. 1-8). VDE.
- [122] Bareiß, M., Krenz, P. M., Szakmany, G. P., Tiwari, B. N., Kalblein, D., Orlov, A. O., ... & Klauk, H. (2013). Rectennas revisited. *IEEE Transactions on Nanotechnology*, 12(6), 1144-1150.
- [123] Russer, J. A., Jirauschek, C., Szakmany, G. P., Orlov, A. O., Bernstein, G. H., Porod, W., ... & Russer, P. (2015, May). Antenna-coupled terahertz thermocouples. In *Microwave Symposium (IMS), 2015 IEEE MTT-S International* (pp. 1-4). IEEE.
- [124] Krenz, P. M., Tiwari, B., Szakmany, G. P., Orlov, A. O., González, F. J., Boreman, G. D., & Porod, W. (2012). Response increase of IR antenna-coupled thermocouple using impedance matching. *IEEE Journal of Quantum Electronics*, 48(5), 659-664.
- [125] Briones, E., Briones, J., Cuadrado, A., Martínez-Anton, J. C., McMurtry, S., Hehn, M., ... & Gonzalez, F. J. (2014). Seebeck nanoantennas for solar energy harvesting. *Applied Physics Letters*, 105(9), 093108.
- [126] Briones, E., Briones, J., Martínez-Anton, J. C., Cuadrado, A., McMurtry, S., Hehn, M., ... & González, J. (2015, May). Seebeck nanoantennas for infrared detection and energy harvesting applications. In *Antennas and Propagation (EuCAP), 2015 9th European Conference on* (pp. 1-4). IEEE.
- [127] Briones, E., Cuadrado, A., Briones, J., de León, R. D., Martínez-Antón, J. C., McMurtry, S., ... & González, F. J. (2014). Seebeck nanoantennas for the detection and characterization of infrared radiation. *Optics express*, 22(106), A1538-A1546.

- [128] Mohan, U., Undeland, T. M., & Robbins W., P. (2003). Power Electronics– Converters. Applications, and Design 3rd Edition John Wiley & Sons Ltd.
- [129] Hwu, K. I., & Yau, Y. T. (2012). High step-up converter based on charge pump and boost converter. *IEEE Transactions on Power Electronics*, 27(5), 2484-2494.
- [130] Adami, S. E., Marian, V., Degrenne, N., Vollaïre, C., Allard, B., & Costa, F. (2012, June). Self-powered ultra-low power DC-DC converter for RF energy harvesting. In *Faible Tension Faible Consommation (FTFC)*, 2012 IEEE (pp. 1-4). IEEE.
- [131] Adami, S. E., Degrenne, N., Vollaïre, C., Allard, B., & Costa, F. (2013, May). Ultra-low power, low voltage, autonomous resonant DC-DC converter for low power applications. In *Power Engineering, Energy and Electrical Drives (POWERENG)*, 2013 Fourth International Conference on (pp. 1222-1228). IEEE.
- [132] LTC3108 – Ultralow voltage step-up converter and power manager. www.linear.com/LTC3108.
- [133] LTC3105 – 400 mA step-up DC-DC converter with maximum power point control and 250 mV start-up. www.linear.com/LTC3105.
- [134] SPV1050 – Ultralow power energy harvester and battery charger. www.st.com/en/power-management/spv1050.html.
- [135] Demo Circuit 1582B Quick Start Guide – LTC3108EDE/LTC3108EDE-1 – Ultralow voltage step-up converter and power manager. <http://cds.linear.com/docs/en/demo-board-manual/dc1582B.pdf>.
- [136] SNx4LS06 – Hex inverter buffers and drivers with open-collector high-voltage outputs. <http://www.ti.com/lit/ds/symlink/sn74ls06.pdf>
- [137] SNx4LS24x – Octal buffers and line drivers with 3-state outputs. <http://www.ti.com/lit/ds/symlink/sn54ls240-sp.pdf>
- [138] SN5432, SN564LS32, SN54S32, SN7432, SN74LS32, SN74S32 – Quadruple 2-input positive OR gates. <http://www.ti.com/lit/ds/sdls100/sdls100.pdf>
- [139] SNx400, SNx4LS00, SNx4S00 – Quadruple 2-input positive NAND gates. <http://www.ti.com/lit/ds/symlink/sn74s00.pdf>
- [140] Di Garbo, C., Cinà, M., Livreri, P., & Vitale, G. (2017). Maximum power transfer optimization in energy harvesting systems based on nanoantennas. *IEEE Transaction on Electron Device Letters*. (In submission)

PUBLICATIONS

Publications on Journals:

- **Di Garbo, C.**, Cinà, M., Livreri, P., & Vitale, G. (2017). Maximum power transfer optimization in energy harvesting systems based on nanoantennas. *IEEE Transaction on Electron Device Letters*. (In submission)
- **Di Garbo, C.**, Livreri, P., & Vitale, G. (2017). Design and optimization of an array of optical rectennas for solar energy harvesting. *Energies*. (In submission)
- **Di Garbo, C.**, Di Liberto, G., Livreri, P., & Vitale, G. (2017). Optimal design issues of optical dipole rectennas array for energy harvesting application. *Applied Energy*. (In submission)

Publications on Conferences:

International conferences with referee

- **Di Garbo, C.**, Livreri, P., Vitale, G. “Optimal matching between optical rectennas and harvester circuits”. In 2017 IEEE International Conference on Environment and Electrical Engineering and 2017 IEEE Industrial and Commercial Power Systems Europe (EEEIC/I&CPS Europe). IEEE. 2017, June 6-9, Milano, Italy.
- **C. Di Garbo**, P. Livreri, G. Vitale, “Review of Infrared Nanoantennas for Energy Harvesting”, International Conference on Modern Electrical Power Engineering (ICMEPE-2016), Las Palmas de Gran Canaria, 6 - 8 Luglio 2016.
- **C. Di Garbo**, P. Livreri, G. Vitale, “Solar Nanoantennas energy based characterization”, International Conference on Renewable Energies and Power Quality (ICREPQ'16), Madrid, 4-6 Maggio 2016;
- A. Parisi, **C. Di Garbo**, R. Pernice, G. Adamo, A.C. Cino, P. Livreri, F. Ricco Galluzzo, A.C. Busacca, G. Calogero, G. Di Marco, C. Vasi, “Fabrication and electro-optical characterization of Ruthenium-based Dye-Sensitized Solar Cells”, AEIT 2015 Convegno Annuale Internazionale, Napoli, Italia, 14-16 Ottobre 2015.

National conferences

- **C. Di Garbo**, P. Livreri, G. Vitale, “Optical Nanoantennas for Energy Harvesting”, 48th Annual Meeting of the Associazione Gruppo Italiano di Elettronica (GE2016), Brescia, 22-24 Giugno 2016;
- A. Parisi, **C. Di Garbo**, R. Pernice, G. Adamo, A.C. Cino, P. Livreri, F. Ricco Galluzzo, G. Calogero, G. Di Marco, C. Vasi, A. C. Busacca, “Characterization of Ruthenium-based Dye-Sensitized solar cells”, 6th EOS Topical Meeting on Optical Microsystems (OμS'15), Capri, Italia, 17-19 Settembre 2015.
- A. Parisi, **C. Di Garbo**, R. Pernice, G. Adamo, A.C. Cino, P. Livreri, F. Ricco Galluzzo, G. Calogero, G. Di Marco, C. Vasi, A. C. Busacca, “Electro-optical characterization of highly efficient Dye-Sensitized solar cells”, Proceedings GE 2015 – 47a Riunione Annuale Gruppo Elettronica, Siena, Italia, 24-26 Giugno 2015.
- A. Parisi, **C. Di Garbo**, R. Pernice, G. Adamo, A.C. Cino, P. Livreri, F. Ricco Galluzzo, G. Calogero, G. Di Marco, C. Vasi, A. C. Busacca, “Photoelectric valuation of highly efficient Dye-Sensitized Solar Cells”, Proceedings Fotonica 2015 - 17° Convegno Nazionale delle Tecnologie Fotoniche, Torino, Italia, 6-8 Maggio 2015, ISBN 978-1-78561-068-4.

GLOSSARY

PV	Photovoltaic cells
LWIR	Long-Wave Infrared Radiation
RF	Radio Frequency
AC	Alternating Current
DC	Direct Current
EWEC	Electromagnetic Wave Energy Converter
IR	Infrared Radiation
EM	Electromagnetic
SPP	Surface Plasmon Polariton
LSP	Localized Surface Plasmons
SEM	Scanning Electron Microscopy
SC	Self Complementary
NSC	Non Self Complementary
EBL	Electron Beam Lithography
FIB	Focused Ion Beam Milling
PMM	Poly Methyl Methacrylate
LMI	Liquid Metal Ion
Ga	Gallium
NIL	Nano-Imprint Lithography
IE	Integral Equation
MoM	Method of Moment
VIE	Volume Integral Equations
FEM	Finite Element Method
FDTD	Finite Difference Time Domain
PML	Perfectly Matched Layers
GUI	Graphical User Interface
FIT	Finite Integration Technique
FFT	Fast Fourier Transform
MIM	Metal Insulator Metal
MOM	Metal oxide Metal
MIIM	Metal Multi-Insulator Metal
MFPL	Mean-Free Path Length
PAT	Photon-Assisted Tunneling
VCS	Vertical Coupled Strips
LCS	Lateral Coupled Strips
Au	Gold

Cu	Copper
CuO	Copper Oxide
MOSFET	Metal Oxide Semiconductor Field Effect Transistor
PWM	Pulse Width Modulation
JFET	Junction gate Field Effect Transistor
MPPC	Maximum Power Point Controller
LDO	Low Dropout Output
MPPT	Maximum Power Point Tracking
UVP	Under Voltage Protection
EOC	End Of Charge
FOM	Figure Of Merit
TTL	Transistor Transistor Logic

This work has been funded by the research project **DELIAS “Ricercatori ed Esperti Di Alta Tecnologia e Innovazione Tecnologica Applicata al Settore dei Beni Culturali”** a valere sull’Avviso n. 713/Ric. del 29 ottobre 2010, TITOLO III, “CREAZIONE DI NUOVI DISTRETTI E/O NUOVE AGGREGAZIONI PUBBLICO – PRIVATE”, PON03PE_00214_2/F9, CUP: B79G14000410001.